

## **Distribution Agreement**

In presenting this thesis or dissertation as a partial fulfillment of the requirements for an advanced degree from Emory University, I hereby grant to Emory University and its agents the non-exclusive license to archive, make accessible, and display my thesis or dissertation in whole or in part in all forms of media, now or hereafter known, including display on the world wide web. I understand that I may select some access restrictions as part of the online submission of this thesis or dissertation. I retain all ownership rights to the copyright of the thesis or dissertation. I also retain the right to use in future works (such as articles or books) all or part of this thesis or dissertation.

Signature:

---

Laura Ann Gray

---

Date

# Formation of Polymer Glasses: Impact of Mechanical Deformation and Cooling Conditions on Physical Aging

By

Laura Ann Gray  
Doctor of Philosophy  
Physics

---

Connie B. Roth  
Advisor

---

Stefan Boettcher  
Committee Member

---

Justin Burton  
Committee Member

---

Meisha Shofner  
Committee Member

---

Eric Weeks  
Committee Member

Accepted:

---

Lisa A. Tedesco, Ph.D.  
Dean of the James T. Laney School of Graduate Studies

---

Date

# Formation of Polymer Glasses: Impact of Mechanical Deformation and Cooling Conditions on Physical Aging

By

Laura Ann Gray  
B.S., North Carolina State University, 2009

Advisor: Connie B. Roth, PhD

An abstract of  
A dissertation submitted to the Faculty of the  
James T. Laney School of Graduate Studies of Emory University  
in partial fulfillment of the requirements for the degree of  
Doctor of Philosophy  
in Physics  
2015

## Abstract

### Formation of Polymer Glasses: Impact of Mechanical Deformation and Cooling Conditions on Physical Aging

By Laura Ann Gray

Polymer glasses are ubiquitous materials used in many applications from containers to gas separation membranes to nanolithography templates. Out of equilibrium glasses exhibit a time-dependent decrease in density during structural relaxation towards equilibrium. Other material properties also change over time due to this slow densification; a process generally called physical aging resulting in a decrease in mobility, an increase in modulus, and a decrease in permeability. For many applications, physical aging leads to an undesired reduction in performance.

In this dissertation, I have explored the effect of cooling rate and stress applied during the glass formation process on the physical aging rate of the subsequent glass. First, we conducted systematic experiments to determine the possible causes of accelerated aging of polymer films with decreasing film thickness previously observed. We found that polystyrene (PS) films held in a free-standing state while cooling through the glass transition temperature,  $T_g$ , exhibited film-thickness dependent aging rate whereas films held in a supported state exhibited aging independent of film thickness. We found that PS films cooled slower through  $T_g$  aged slower. However, this did not explain the accelerated, faster physical aging observed for free-standing films, as free-standing films cool faster than supported films, yet aged slower.

Based on the above findings, we hypothesized that differences in stress applied to the films by their supports may account for their aging behavior. A fundamental question surrounding glass formation and jammed materials is how does the glass formation process affect the subsequent state of the glass? Here, we investigated polymer glasses formed at a non-zero, controlled stress for the first time. We constructed a simple apparatus to apply a constant tension to a polymer film while cooling through  $T_g$ . We observed that as stress applied during the quench is increased, the physical aging rate of PS remained constant until quickly transitioning to a much higher aging rate above a minimum threshold in stress. We proposed that stress applied during glass formation can alter the potential energy landscape of the glass former, resulting in the glass ending up in a higher energy state when formed under high stress.

In order to probe the origins of this minimum stress required to increase physical aging, we designed and constructed another experimental apparatus to control and monitor both stress and strain on cooling in polymer films. We measured the tensile yield stress as a function of temperature for PS above  $T_g$ . We estimated the work done by the yield stress to lower potential energy barrier heights as a function of temperature and found that near  $T_g$  this work becomes comparable to the thermal activation energy, a measure of potential energy barrier height. Therefore, on cooling with an applied stress greater than the yield stress near  $T_g$ , the potential energy landscape barrier heights can be significantly altered. This yield stress corresponds to the minimum threshold in stress we observed required to increase the physical aging rate.

The results presented in this dissertation are important to consider when preparing glasses as stress is common, often due to thermal expansion coefficient mismatch between the material and the mold. These results also indicate that stress upon cooling can change the state of the glass, altering the physical aging of the polymer.

# Formation of Polymer Glasses: Impact of Mechanical Deformation and Cooling Conditions on Physical Aging

By

Laura Ann Gray  
B.S., North Carolina State University, 2009

Advisor: Connie B. Roth, PhD

A dissertation submitted to the Faculty of the  
James T. Laney School of Graduate Studies of Emory University  
in partial fulfillment of the requirements for the degree of  
Doctor of Philosophy  
in Physics  
2015

# Acknowledgements

I have received a lot of help and support over the last several years on my way to a PhD and if I forget anyone, it's because my brain may be a little fried from the process. First I would like to thank my husband, Kip, for all his support and never giving up on me. Next, I'd like to thank my dad for all his influence in making me the nerd for science that I am today.

One of the largest thank you's has to go to my adviser, Connie Roth. She taught me due scientific diligence, even when I didn't want to. She has led me through the ups and downs of scientific research for five years with a smile and lots of encouragement. Throughout my future career, she will provide me with an excellent role model as I hopefully continue in research.

I'd like to thank my committee members, Stefan Boettcher, Justin Burton, Meisha Shofner, and Eric Weeks, for their valuable feedback and for reading this manuscript. I'd like to thank the amazing machine shop and electronics staff: Cody Anderson, Horace Dale, Josh Savory, and Lowell Ramsey. Without them, these experiments would not have happened. I'd like to thank all the physics department staff that have helped me out and always know how to fix things: Calvin Jackson, Paulette Evans, Connie Copeland, Art Kleyman, and Jason Boss.

The members of the Roth lab over the years have been great. Justin Pye has been more than a labmate and has been a great friend. His continued, never-ending excitement about literally everything is not quite contagious, but is very admirable. I'd like to thank Roman Baglay, Michael Thees, Phil Rauscher, and Xinru Huang for all their friendships and discussions. Thank you to everyone I've met at Emory along the way.

# Table of Contents

<b>Chapter 1: Introduction and Scope of Dissertation .....</b>	<b>1</b>
1.1 Introduction to Glasses and Open Questions .....	1
1.2 Outline of Dissertation .....	7
<b>Chapter 2: Background .....</b>	<b>10</b>
2.1 Synopsis .....	10
2.2 Potential Energy Landscape Description of Glasses .....	11
2.3 Molecular Mobility Enhanced by Deformation .....	15
2.4 Stress-Induced Landscape Tilting .....	19
2.5 Stresses in Glass Formation .....	23
2.6 Anomalous Physical Aging and Mechanical Properties in Thin Polymer Films .....	26
2.6.1 Accelerated Physical Aging with Decreasing Film Thickness .....	26
2.6.2 Free Volume Diffusion Model .....	30
2.6.3 Rubbery Stiffening in Polymer Thin Films .....	31
2.7 Summary .....	35
<b>Chapter 3: Physical Aging Behavior of Glassy Polymer Films: Effect of Quench Conditions .....</b>	<b>36</b>
3.1 Synopsis .....	36
3.2 Introduction .....	37
3.3 Experimental Methods .....	41
3.4 Results and Discussion .....	44
3.4.1 Effect of Polymer Chemical Structure: Stiff Backbone vs. Flexible C–C Backbone with Bulky Side-Groups .....	44
3.4.2 Free-Standing vs. Supported Quench .....	48
3.4.3 Effect of Annealing Conditions on Physical Aging Rate .....	51
3.4.4 Effect of Quench Rate on Physical Aging Rate .....	53
3.4.5 Applied Stress during Quench due to Thermal Expansion Mismatch .....	59
3.5 Summary and Conclusions .....	66

**Chapter 4: Formation of Polymer Glasses under Stress: Effect on Physical Aging ..... 67**

4.1	Synopsis .....	67
4.2	Introduction .....	68
4.3	Experimental Methods .....	71
4.4	Results and Discussion .....	73
4.5	Summary and Conclusions .....	84

**Chapter 5: Mechanical Tensile Testing Apparatus for Controlled Deformation of Polymer Films during Vitrification ..... 86**

5.1	Synopsis .....	86
5.2	Introduction .....	86
5.3	Experimental Techniques .....	91
5.3.1	Mechanical Tensile Testing Apparatus: Components and Calibration .....	91
5.3.2	Sample Preparation .....	103
5.4	Results and Discussion .....	104
5.4.1	Mechanical Behavior of Polystyrene above $T_g$ under Constant Strain Rate Deformation .....	104
5.4.2	Stress Relaxation of Polystyrene above $T_g$ .....	114
5.4.3	Polystyrene Creep above $T_g$ .....	118
5.5	Summary and Conclusions .....	120

**Chapter 6: Stress Build Up and Yield in Polymer Films near the Glass Transition ..... 123**

6.1	Synopsis .....	123
6.2	Introduction .....	124
6.3	Experimental Techniques .....	128
6.4	Results and Discussion .....	129
6.4.1	Stress Build up on Cooling at Constant Length .....	129
6.4.2	Yield above the Glass Transition Temperature .....	132
6.5	Summary and Conclusions .....	138

**Chapter 7: Summary..... 139**

**Bibliography ..... 145**

# List of Figures

1	Figure 1.1: a) Volume vs. temperature schematic of the thermal glass formation process during vitrification. b) Schematic of logarithmic decrease in volume with aging time .....	2
2	Figure 1.2: Jamming phase diagram proposing an equivalence between temperature, density, and stress controlling glassy and jammed systems .....	4
3	Figure 2.1: Schematic of a potential energy landscape .....	12
4	Figure 2.2: a) Schematic of changes to the potential energy landscape upon mechanical deformation that reduces the barriers for hopping events. b) Schematic depiction of potential energy vs. strain for large deformations .....	20
5	Figure 3.1: Pictures of the free-standing frames with PS films used in the studies in Chapter 3 .....	41
6	Figure 3.2: Normalized film thickness vs. logarithm of aging time for an example bulk PS film spin coated, annealed, quenched, and aged supported on a silicon wafer .....	43
7	Figure 3.3: Normalized film thickness vs. aging time showing physical aging of a) PSF films and b) PS films for two different film thicknesses, spin cast, annealed, quenched, and aged supported on silicon .....	45
8	Figure 3.4: Normalized film thickness vs. aging time for PS films quenched in a free-standing vs. supported states, all films were subsequently aged in a supported state for a) 1260 nm thick PS films. b) 600 nm thick PS films .....	49

9	Figure 3.5: a) Schematic of how supported PS films were cooled after removal from vacuum oven to control quench rate. b) Example temperature profile of the top of a silicon wafer atop the copper base cooled to 30 °C .....	54
10	Figure 3.6: Normalized film thickness vs. aging time for bulk, supported PS films cooled at various cooling rates through $T_g$ .....	56
11	Figure 3.7: Physical aging rate of PS supported films vs. a) cooling rate or b) log of cooling rate .....	56
12	Figure 3.8: Photographs of free-standing films being cooled through $T_g$ , held on a) wire frame, b) rigid nylon frame with rectangular hole, or c) rigid nylon frame with circular hole .....	65
13	Figure 4.1: Jamming phase diagram illustrating that the experiments in Chapter 4 will access the glassy state by cooling at a non-zero stress .....	69
14	Figure 4.2: Pictures and a schematic of the jig used to apply a constant stress to a polymer film above $T_g$ and during the thermal quench .....	73
15	Figure 4.3: Normalized film thickness vs. logarithm of aging time for $M_w = 1440$ kg/mol PS films quenched under stress .....	74
15	Figure 4.4: (top) Physical aging rate vs. applied stress during the quench for PS films of $M_w = 1440$ kg/mol and 650 kg/mol. (bottom) Total strain vs. stress for $M_w = 1440$ kg/mol PS films .....	76
16	Figure 4.5: Strain response of films stressed above $T_g$ in the rubbery regime (same data as Figure 4.4). Bulk rubbery creep compliance is also plotted .....	78

17	Figure 4.6: a) Normalized film thickness vs. logarithm of aging time for $M_w = 289$ kg/mol PS films quenched under stress. b) Physical aging vs. applied stress during the quench for PS films of $M_w = 289$ kg/mol with comparison to the physical aging rate behavior of the $M_w = 1440$ kg/mol and 650 kg/mol PS ..... 79	79
18	Figure 4.7: Schematic potential energy landscape of a typical glass former, showing the dependence on cooling rate ..... 82	82
19	Figure 4.8: Proposed effect of stress during glass formation on local PEL. For large enough stress values, the PEL is sufficiently “tilted” that on cooling the system ends up trapped in a different, higher metabasin, exhibiting correspondingly faster physical aging even after the stress is removed ..... 83	83
20	Figure 5.1: Schematic of modulus vs. time or temperature for entangled PS exhibiting glassy, rubbery, and flow behavior ..... 88	88
21	Figure 5.2: Schematic of the computer-controlled mechanical tensile testing apparatus capable of controlling and monitoring stress and strain on thin polymer films at various temperatures ..... 92	92
22	Figure 5.3: a) Schematic of the stainless steel stretching frame which supports the film in the mechanical tensile testing apparatus b) with removable M-shaped bracket that pins the two halves of the frame together to allow films to be floated onto the frame ..... 93	93
23	Figure 5.4: a) Load cell calibration curve and linear fit. b) Residuals from the difference between the measured voltage and the fit vs. load ..... 95	95
24	Figure 5.5: Example noise recorded for the load cell when the linear actuator is moving ..... 96	96

25	Figure 5.6: a) LVDT calibration curve and linear fit. b) Residuals from the different between the measured voltage and the fit vs. extension ..... 97	97
26	Figure 5.7: Force (N) vs. extension (mm) calculated by multiplying the time by the strain rate or from the LVDT signal ..... 99	99
27	Figure 5.8: a) Force (N) vs. extension or compression (mm) of the spring. b) Residuals from the first two force vs. position curves in a) ..... 100	100
28	Figure 5.9: Position (mm) as measured by the LVDT vs. time for repeated extensions and compressions of the spring as show in Figure 5.8 ..... 101	101
29	Figure 5.10: Force (N) vs. time for a spring extended to a given length and held there to show the lack of any relaxation in the tensile testing device ..... 102	102
30	Figure 5.11: Force (N) vs. time for five different bulk PS films under constant uniaxial strain rate of $0.001 \text{ s}^{-1}$ ..... 104	104
31	Figure 5.12: Stress (Pa) vs. strain for PS films deformed at $140 \text{ }^{\circ}\text{C}$ for the data sets shown in Figure 5.11 ..... 105	105
32	Figure 5.13: Schematic of a standard linear solid spring and dashpot model. 107	107
33	Figure 5.14: Stress/strain rate (Pa s) vs. time (s) for 23 – 33 micron thick PS films deformed at a constant strain rate of $0.001 \text{ s}^{-1}$ at $140 \text{ }^{\circ}\text{C}$ with fits to the standard linear solid ..... 109	109
34	Figure 5.15: a) Stress divided by strain rate vs. time for PS films deformed at four different constant strain rates at $140 \text{ }^{\circ}\text{C}$ . b) Zoomed in version of a) to show separation of stress response by strain rate ..... 111	111

35	Figure 5.16: Standard linear solid fit parameters for PS deformed at constant strain rate at 140 °C. a) $E_R$ , b) $E_G$ , c) $\tau$ vs. strain rate .....	112
36	Figure 5.17: Stress (Pa) vs. time for PS films under constant strain rate deformation of $0.001 \text{ s}^{-1}$ at various temperatures above $T_g = 100 \text{ °C}$ .....	113
37	Figure 5.18: Standard linear solid fit parameters for PS deformed at a strain rate of $1 \times 10^{-3} \text{ s}^{-1}$ . a) $E_R$ , b) $E_G$ , c) $\tau$ vs. temperature .....	114
38	Figure 5.19: a) Stress (Pa) vs. time for PS films from $T = 120 - 140 \text{ °C}$ quickly (see text for discussion) pulled to 10% strain than held at constant length. b) Same data as a) but logarithm of the stress minus the long term average stress plotted vs. time .....	116
39	Figure 5.20: a) Stress vs. time and b) strain vs. time for constant stress applied to a PS film at 130 °C. c) Stress vs. time and d) strain vs. time for constant stress applied to a PS film at 105 °C .....	120
40	Figure 6.1: Example stress (Pa) vs. temperature (°C) for films cooled from 120°C for four different cooling rates .....	131
41	Figure 6.2: a) Temperature at which stress initially increases on cooling, $T_{\text{onset}}$ , vs. cooling rate for PS films cooled at a fixed length. b) Same data, plotted vs. logarithm of cooling rate .....	131
42	Figure 6.3: Stress (Pa) vs. strain for PS films under constant strain rate ( $0.001 \text{ s}^{-1}$ ) deformation at a) 102 °C exhibiting yield as a maximum stress and b) 110°C exhibiting yield as a change in slope .....	133

43	Figure 6.4: Yield stress (Pa) vs. temperature (°C) for $M_w = 1921$ kg/mol PS. The blue bar indicates the range of applied stress in Chapter 4 during the thermal quench over which the aging rate of high molecular weight PS films doubled ..... 134
44	Figure 6.5: Comparison of thermal activation energy (red line) and work done by stress. Work done by stress becomes larger than thermal activation energy at $T = 101.2 \pm 1.2$ °C and corresponding $\sigma = 7.5 \pm 1.2$ MPa ..... 137

# List of Tables

1	Table 3.1: Measured quench rates for PS films supported on silicon cooled on either copper, ceramic, or ceramic and Teflon bases to 30 °C and 65 °C .....	55
2	Table 5.1: Technical specifications of the load cell, linear voltage displacement transducer, and linear actuator used in the construction of the mechanical tensile testing apparatus .....	102
3	Table 5.2: Estimated error in measurements of stress and strain for two example film thicknesses, 1 $\mu\text{m}$ and 20 $\mu\text{m}$ .....	103
4	Table 5.3: Characteristic relaxation time and rubbery modulus from the standard linear solid for constant strain rate deformations and stress relaxation .....	117

# Chapter 1

## Introduction and Scope of Dissertation

### 1.1 Introduction to Glasses and Open Questions

Glasses are ubiquitous materials. A glass is a solid with an amorphous structure, *i.e.* the dynamics of the atoms and molecules resemble a solid but the structure and lack of long range order resemble that of a liquid. From window glass, a small molecule glass former, to the hundreds of millions of tons of plastics made every year,<sup>1</sup> glasses are used in a wide variety of manners. Familiar polymer glasses such as polystyrene (PS) are often used as containers while less familiar ones such as polysulfone (PSF) are used for gas separation membranes in the energy industry.

Molecular and polymeric glasses are formed when an equilibrium liquid is cooled fast enough that the molecules cannot rearrange into an equilibrium structure and become kinetically trapped in a disordered, non-equilibrium state. Some materials, such as atactic polystyrene, have no crystalline state due to the geometry of the molecules. Figure 1.1a shows a schematic of the glass formation (or vitrification) process. At high temperatures the liquid is in equilibrium. As the liquid is cooled the relaxation time of the molecules grows as less thermal energy is available. At some temperature, the cooling rate becomes faster than the timescale over which the system can rearrange and it falls out of equilibrium; this temperature is called the glass transition temperature ( $T_g$ ). Faster cooling rates result in a higher glass transition temperature ( $T_{g2}$  in Figure 1.1a) than slower cooling rates ( $T_{g1}$ ). The initial volume of the glass and the glass's distance from equilibrium (black dashed line extrapolated from the liquid equilibrium line) depend on

the cooling rate. The glass transition may seem like a phase transition at first glance. Vitrification is not a first order phase transition as there is a smooth change in density and not a sharp one when a glass former is cooled from the liquid to the glassy state. The glass transition therefore looks like a second order phase transition. However, the value of  $T_g$  depends on the cooling rate, earning it the moniker of a kinetic transition. An ideal or real glass phase transition has been hypothesized to exist in the limit of infinitely slow cooling, though its theoretical existence is under debate.<sup>2-6</sup>

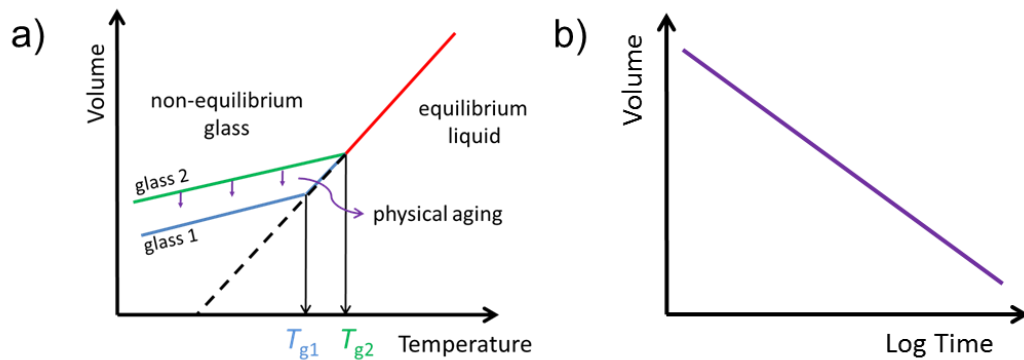


Figure 1.1: a) Volume vs. temperature schematic of the thermal glass formation process (vitrification). As the liquid is cooled, molecular motion slows down until eventually the molecules cannot rearrange and the system falls out of equilibrium into an amorphous glassy state. How quickly the glass is cooled determines the temperature at which the glass falls out of equilibrium: slower cooling rates allows the system to spend more time at a given temperature, allowing it to find equilibrium at lower temperatures than a glass cooled more quickly. Once in the glassy state, the volume decreases over time as a result of physical aging as shown by the purple arrows. b) Schematic of how volume decreases logarithmically with aging time.

Glasses are formed when packing frustration leaves the system trapped in a higher energy configuration that does not correspond to the global energy minimum of the crystalline state (if it exists) or an equilibrium glassy state. This high energy state contains excess free volume; as the glass evolves over time it densifies (as shown in Figure 1.1b), a process generally called structural recovery.<sup>7-9</sup> This small volume change is associated with large changes in physical properties and a slowing down of dynamics

which are often referred to as physical aging.<sup>9</sup> Here, I will use the term physical aging to generally mean the volumetric decrease over time as the glass densifies towards equilibrium. The physical aging rate depends on the distance from equilibrium (among other factors as will be discussed in greater detail later) and therefore is greatly influenced by the glass formation process. As a result of the small decrease in free volume over time (<1%), large changes in physical properties such as an increase in modulus<sup>10</sup> and decrease in permeability<sup>11,12</sup> have been observed.

Figure 1.1 describes the vitrification process by which thermal glasses undergo kinetic arrest. Other materials also undergo kinetic arrest when the *density* of particles is increased or when *external stress* drives the system to jam. For example, colloids (such as milk and paint) can become jammed when the density of particles in the fluid exceeds a critical value. Sand piles can jam when friction is strong enough to prevent grains from sliding down the slopes of the pile. Sand can become unjammed by the application of shear. On the surface, these processes that result in thermal glasses and jammed sands or colloids appear similar and raise some interesting questions. Can comparisons between athermal jamming and thermal vitrification be made? If so, this suggests the possibility that the glass transition may be a universal concept that can explain the behavior of many different system. To what extent do temperature, density, and stress control glass formation? Andrea Liu and Sid Nagel originally proposed a jamming phase diagram,<sup>6,13,14</sup> as shown in Figure 1.2, to unite the physics explaining the kinetic arrest of these varied systems.

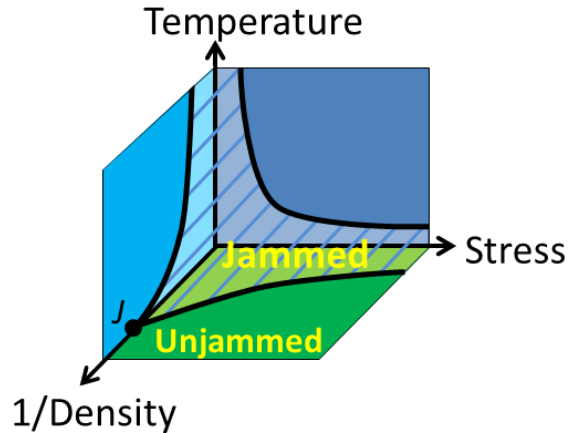


Figure 1.2: Jamming phase diagram based on O’Hern, *et al.*<sup>14</sup> that proposes an equivalence between temperature, density, and stress controlling glassy and jammed systems. For example, granular materials exist in the  $T = 0$  plane.

Liu and Nagel’s jamming phase diagram, originally proposed in 1998,<sup>13</sup> was inspired by work of Cates, *et al.* who proposed that amorphous solids such as granular materials, foams, and colloids should be treated differently from regular solids.<sup>15</sup> As these solids are only solid because they are driven into the jammed state by external stress, the nature of their mechanical stability intimately depends on the details of the applied stress. Additional applied stress in a different direction from the jamming stress would lead to yield, therefore these materials are “fragile” to some types of deformation, violating an elastic model of the material. Cates, *et al.* then argued that this class of solids should be unified under common physics.<sup>15</sup>

Liu and Nagel took this idea and asked if it could be applied to other amorphous solids formed under a broader set of conditions, adding thermal glasses into the picture.<sup>13</sup> The jamming phase diagram has been used to illustrate the concept that the diversity of jammed or glassy systems, from granular materials, foams, and colloids, to polymer glasses, share common attributes. For example, all these systems exhibit dynamic heterogeneities near jamming and have super Arrhenius relaxations in temperature or

density as jamming or the glass transition is approached.<sup>16,17</sup> A peak in low-frequency modes for both jammed and glassy materials not seen in crystalline solids also suggests a similarity between these states.<sup>6</sup> The jamming phase diagram suggests that temperature, density, and stress (mechanical deformation) might act as different control parameters that determine whether the system is jammed or unjammed.

Can these disparate systems, from granular materials to thermal glasses, be united under the same physical description? Some early investigations hinted at this possibility. Langer and Liu<sup>18</sup> measured the viscosity and stress fluctuations in a simulation of a sheared 2D foam. They found that the relation between viscosity and stress fluctuations, a measure equivalent to temperature, were the same as the relation between viscosity and temperature for a supercooled liquid glass-former.<sup>18</sup> Corwin, Jaeger, and Nagel<sup>19</sup> examined the structure and presence of force chains in an athermal, sheared granular material. They described the distribution of forces in the sheared, unjammed granular state with a model that assumed an equilibrated system. They concluded that the concept of the jamming phase diagram was supported by the existence of an equilibrium description for sheared granular media.<sup>19</sup> The shape of the jamming phase diagram evolved over time as well.<sup>13,14,20</sup> Ciamarra, Nicodemi, and Coniglio<sup>20</sup> suggested changes in the shape to the jamming phase diagram in light of studies on soft spheres. They also questioned whether the dependence on protocol of the density at the jamming transition for athermal hard spheres would lead to a jamming segment rather than a jamming point<sup>20</sup> (as shown in Figure 1.2).

More recent studies have critically questioned the jamming phase diagram and have shown a lack of equivalence between the properties governing the jamming and

glass transitions.<sup>21-25</sup> For example, Ikeda, Bertier, and Sollich studied the jamming and glass transition of repulsive colloids as a function of the relative strength of thermal fluctuations (Brownian motion) and viscous dissipation.<sup>24</sup> This system allowed them to study a range of thermal vitrification to athermal jamming without changing material. The glass and jamming transitions were defined by a divergence in viscosity or the emergence of a yield stress. A glass transition was observed for colloids at non-zero temperature and Peclet number ( $Pe$ , the ratio of advection to diffusion)  $< 1$ , where viscous dissipation is small. A jamming transition was observed at  $T = 0$ , as well as at low temperatures and high Peclet number ( $Pe \gg 1$ ). The jamming transition occurred at higher packing fractions and yield stresses than the glass transition. At very low temperatures, but high  $Pe$ , flow was observed above the glass transition packing fraction, resulting in a coexisting jamming transition at higher packing fractions. Their results indicate that the glass transition line does not extrapolate to the jamming point at  $T = 0$ , *i.e.* that there is a crossover in dynamics from the thermal to athermal regime.<sup>24</sup>

Despite the failure to depict the behavior of real systems, the ideas behind the jamming phase diagram are still useful concepts to generate new questions about glassy materials. For instance, how responsive are thermal glasses to external stress?<sup>13</sup> Here, in this dissertation, we will explore how the properties of the glassy state depend on how the glass is formed. We will specifically examine how the stability of the glass, as measured by physical aging, is affected by cooling rate. For the first time, we will address how stress present during the thermal glass formation process (cooling off axis on the jamming phase diagram, Figure 1.2, at a non-zero stress) affects the stability of the glass.

These results imply that the stability of the glassy state can be tuned through careful control of multiple aspects of the glass formation process.

## 1.2 Outline of Dissertation

This dissertation is comprised of seven chapters detailing the research I accomplished towards the goal of understanding the effects of the glass formation process on the subsequent glassy state.

Chapter 2 consists of a literature review detailing experiments, simulations and theory to describe glass formation and glasses under deformation, with a focus on polymers. In addition relevant studies of anomalous physical aging and mechanical properties of polymer thin films will also be summarized. The chapter begins with a description of the potential energy landscape (PEL) framework for glass formers. Next, I present a discussion of experiments and simulations that observe increased molecular mobility in glasses under deformation. The PEL description has been used to explain the observed enhanced mobility in glasses under deformation. These studies were all conducted on glasses nominally formed stress free. However, I will argue that stress is often present during the glass formation process, motivating the study presented in Chapter 4 on the effect of stress during glass formation on the physical aging rate of polymer films. Chapter 2 will continue with a review of “accelerated” (faster) physical aging seen in the literature with decreasing film thickness for films up to several microns thick. Finally, I will conclude the chapter with a description of the mechanical properties of polymer thin films above the glass transition.

Motivated by the anomalous accelerated physical aging observed in polymer thin films at large, micron length scales, Chapter 3 details efforts to probe the cause of these

results. In Chapter 3, I describe experiments that systematically explored the effects of molecular structure, quench depth below the glass transition temperature, and quench rate through  $T_g$ , on the physical aging rate of polymer thin films. We found that polystyrene quenched in a free-standing state exhibited a film-thickness dependent physical aging rate that was not present for films quenched in a supported state. We found that films quenched slower through  $T_g$  aged slower than films quenched faster. This quench rate dependence of aging rate did not explain the film thickness dependent aging rate for films quenched in a free-standing state. Free-standing films quenched faster than supported films, yet aged slower. By process of elimination, we proposed that stresses present during the glass formation process may account for the different behavior of films quenched free-standing or supported. A version of this chapter was published as:

Gray, L. A. G., Yoon, S. W., Pahner, W. A., Davidheiser, J. E. Roth, C. B. Importance of Quench Conditions on the Subsequent Physical Aging Rate of Glassy Polymer Films. *Macromolecules* **45**, 1701 – 1709 (2012).

In Chapter 4, I present a method to directly apply a known stress to a polymer thin film during the glass formation process. For the first time, we probed how deformation imparted to the glass while it forms affects the stability of the glass, even after the stress has been removed. As stress applied during the quench was increased, the physical aging rate remained constant until quickly transitioning to a higher aging rate above a minimum threshold in stress. We suggested that the stress during the glass formation process can deform the potential energy landscape of the glass, causing the glass to fall into a different potential energy state under high stress. A version of this chapter was published as:

Gray, L. A. G., Roth C. B. Stability of Polymer Glasses Vitrified under Stress. *Soft Matter*, **10**, 1572 – 1578 (2014).

Chapter 5 describes the design, construction, and testing of a new experimental apparatus to control stress and strain applied to polymer thin films near and above the glass transition temperature. The details of the mechanical tensile testing apparatus are presented as well as tests of the mechanical properties of bulk polystyrene under uniaxial deformation above  $T_g$  to ensure the operation of the apparatus. These measurements include the stress response to constant strain rate deformation, stress relaxation, and creep above  $T_g$ .

Using the experimental apparatus detailed in Chapter 5, Chapter 6 presents experimental studies aimed to explore the importance of the threshold stress applied during the quench required to increase the physical aging rate as seen in Chapter 4. When a polymer film was cooled at a fixed length, we observed a quench rate dependent stress build up. The temperature at which stress build-up first occurs is well above the glass transition temperature, up to  $T_g + 16$  °C for moderate cooling rates. For temperatures between  $T_g$  and  $T_g + 15$  °C, we measured the yield stress vs. temperature. We found that the work done by the yield stress becomes greater than the thermal activation energy (a measure of potential energy barrier height) below  $\sim 101$  °C. We propose that this indicates that stresses above the yield stress at 101 °C (7.5 MPa) can alter the potential energy landscape as the polymer film is cooled above that value of stress. This value agrees well with the applied stress during the quench required to increase the physical aging rate found in Chapter 4.

# Chapter 2

## Background

### 2.1 Synopsis

In this Chapter, I will present a literature review that will inform our investigations of the effects of glass formation process on the stability of the glass. The potential energy landscape description of glass formers is introduced first. Next, is a summary of experiments and simulations that have found enhanced molecular mobility in glasses under deformation. It has been proposed that stress can “tilt” the potential energy landscape. Simulations and theoretical predictions have linked the increase in potential energy with enhanced mobility. Stress is an important factor to consider not only when applied to the glassy state but also when the glass is being formed. I will discuss a common source of stress during the glass formation process. For the bulk of my dissertation, I will investigate the effect of different glass formation protocols on physical aging. In the literature, accelerated physical aging has been observed with decreasing film thickness for polymer films several microns thick. This phenomenon has been described as a confinement effect governed by the diffusion of free volume out of the film. However, the length scale is much larger than other confinement length scales and free volume diffusion theory does not accurately portray the distribution of free volume in films or describe physical aging under compressive deformation. Finally, I will discuss experiments in the literature that report mechanical stiffening for thin polymer films above  $T_g$ .

## 2.2 Potential Energy Landscape Description of Glasses

The potential energy landscape (PEL) has long been used as a tool to understand the properties of glasses and glass formation.<sup>2,3,26,27</sup> The potential energy landscape is a multidimensional phase space where each configuration of the components of the glass has an associated potential energy. Figure 2.1 presents a schematic example of a potential energy landscape. The nature of the potential energy minima and the saddle points between them depends on the material properties of the glass former.<sup>3</sup> For example, strong glass formers have a uniform rough landscape with one central minimum while fragile glass formers have a more complex landscape like that shown in Figure 2.1.<sup>3</sup> Figure 2.1 represents a simplified picture of a PEL as the landscape is really a  $3N$  dimensional phase space, where  $N$  is the number of particles in the system.

A simple way in which the barriers between configurations can be determined is using elastic theory as discussed by Heuer<sup>27</sup> and Dyre.<sup>4</sup> The intermolecular potential is approximated by a harmonic potential. The energy barrier between two configurations is then proportional to the energy where the harmonic potentials cross. The relaxation time of a molecule can be defined as the mean-squared thermal average displacement around the minimum in potential energy, which in equilibrium is Arrhenius.<sup>4</sup> This allows the energy barrier to be calculated from the relaxation time. The energy barrier has also been proposed to be proportional to the instantaneous shear modulus, which represents the energy needed for other molecules to move out of the way.<sup>4,27</sup> The potential energy landscape can then be built up by applying this model to every molecule and its neighbors. Kinetic energy, proportional to  $k_B T$ , is not included in the calculation of the *potential* energy landscape, making the PEL a material property that does not change as a

function of temperature.<sup>26</sup> Instead, as temperature changes, the accessibility of various potential energy minima changes.

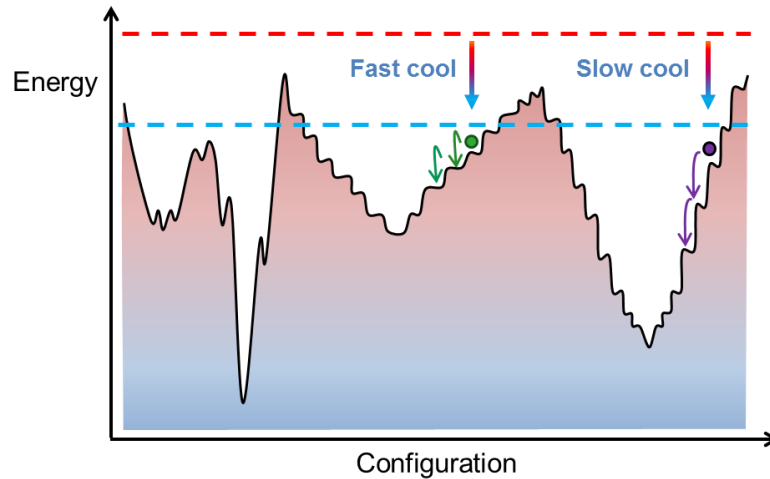


Figure 2.1: Schematic of a potential energy landscape. Each configuration of the glass former has a corresponding energy associated with it.

A few features of the PEL are immediately apparent from Figure 2.1. While individual local minima (also called inherent structures) exist, many of them can be grouped into a larger basin of attraction or metabasin.<sup>2,3,26,27</sup> One way a metabasin can be defined is as a collection of inherent structures with a probability greater than 50% of falling back into the central minimum.<sup>27</sup> While the PEL does not depend on temperature, how the system explores the PEL does. At high enough temperatures in the liquid regime, the system has enough energy to sample all configurations.<sup>27</sup> For systems in the liquid state, the time spent in one metabasin is short and does not depend on the height of the energy barriers between metabasins.<sup>27</sup>  $\alpha$ -relaxations are present and consist of hops between metabasins.<sup>2</sup> As the temperature is lowered, the system samples lower energy metabasins and the transitions between metabasins becomes “activated,” *i.e.* many particles must move in order to overcome the potential energy barrier leading to rare and often sudden rearrangements. Once the temperature has been lowered such that the

system is in the “landscape influenced regime”, the time dependence of molecular motion changes. At high temperatures, the relaxation of the intermediate scattering function,  $F$ , that measures the probability of a molecule moving a given distance over a given time, is exponential in time. As temperature is lowered,  $F$  becomes a stretched exponential of the form  $F = \exp\left(-\frac{t}{\tau}\right)^{\beta_{KWW}}$  where  $t$  is time,  $\tau$  is the characteristic relaxation time, and  $\beta_{KWW}$  is the Kohlrausch-Williams-Watts stretching parameter.  $\beta_{KWW}$  less than one indicates that the system has reached the landscape influence regime,<sup>3,26</sup> and has been shown to indicate heterogeneous dynamics within the system.<sup>17</sup> As temperature is further decreased within the “landscape influenced regime”, the relaxation behavior of the glass former splits into two relaxation times: a slow  $\alpha$ -relaxation and a fast  $\beta$ -relaxation.<sup>2,3</sup> Below the glass transition temperature,  $\alpha$ -relaxations are frozen out and  $\beta$ -relaxations, that only require local rearrangements, within a metabasin, occur.<sup>2</sup> The system is then trapped in a metabasin.

Temperature alone does not define the state of a glass. Cooling rate greatly affects polymer properties, such as the value of the glass transition temperature (illustrated in Figure 1.1), and the physical aging rate. If the system is cooled slower, there is more time at a given temperature to sample the potential energy minima, resulting in the system becoming trapped in a deeper, lower energy metabasin than at faster cooling rates, as drawn in Figure 2.1.<sup>3,26</sup> Faster cooling results in the system becoming trapped in a higher potential energy metabasin that have been shown to be more shallow.<sup>27</sup>

In this dissertation, I will explore the stability of glasses formed under different conditions by measuring the physical aging rate. Physical aging can be thought of as

settling into the metabasin and exploring lower energy inherent structures within that metabasin, consistent with but not precisely equal to  $\beta$ -relaxations between nearby inherent states. Higher potential energy minima further from equilibrium have a larger enthalpic drive towards equilibrium than lower energy states. As physical aging is a change in density over time it is accompanied by a change in configuration of the molecules making up the glass. For systems in a high, shallow metabasin, physical aging requires a larger change in configuration for the same decrease in energy as in a deeper, lower energy metabasin. Therefore, higher, shallower metabasins can be associated with faster physical aging. In Chapter 3, I will discuss experiments concerning the effect of cooling rate on physical aging rate.

Another measure of the stability of the glassy state is the molecular mobility. The potential energy landscape and relaxations within it can also reveal information about the mobility of the glassy system. The distribution of waiting times for hopping out of a metabasin can indicate whether the system is liquid-like or solid-like.<sup>27</sup> The routes into and out of a metabasin are more likely to be correlated for liquid-like systems when the system spends less time in a given metabasin than does a solid-like system. The diffusion coefficient can be defined from the metabasin waiting time.<sup>27</sup> Since the waiting time in a metabasin depends on the depth of the metabasin as well as the temperature, the PEL helps inform the kinetics of the system. As will be discussed below, greater mobility has been experimentally observed in glasses when they are deformed.<sup>19,28-34</sup> The PEL picture provides a framework to interpret the following experiments and simulations; under deformation the PEL itself can be “tilted”,<sup>35,36</sup> allowing the system to transition to another metabasin.<sup>37-45</sup>

## 2.3 Molecular Mobility Enhanced by Deformation

Many studies have been conducted on how glassy mobility is enhanced upon deforming the glass across different systems from granular materials to colloids to polymer glasses.<sup>19,28–34</sup> Corwin, Jaeger, and Nagel observed the distribution of normal forces on the bottom plate of a shear annulus containing a cylindrical pack of granular beads.<sup>19</sup> The normal force distribution in the jammed state did not change with the presence of shear as long as yield was not exceeded. Once flow, or unjamming, was achieved, the distribution of normal forces changed.<sup>19</sup> This result indicates that shear can add mobility to a granular system and bring it out of the jammed state, similar to an increase in temperature for a thermal glass. Viasnoff and Lequeux conducted experiments on sheared colloids and observed the evolution of the relaxation time of the colloidal particles using multispeckle diffusing wave spectroscopy that measures the average displacement of particles.<sup>28</sup> They asked if shear could reduce the effects of aging, *i.e.* reverse the slowing down of dynamics over time? After shearing to 20% strain, the relaxation time increased, independent of shear rate, indicating a “rejuvenation” of dynamics. However, at moderate strains slower relaxation times were observed, which they called over-aging. One question raised by the concept of the jamming phase diagram is how similar are temperature and stress at controlling the jammed or glassy state? Over-aging was marked by an increase in population of long-time relaxations compared to aging under no shear, indicating a more complex response to shear than the simple decrease in relaxation times expected with rising temperature.<sup>28</sup> These experiments in colloids and granular materials suggest that deformation can alter the dynamics and structure of the jammed state, even leading to plastic flow and erasure

of the jammed state, but leave open questions about the similarities between thermal and shear rejuvenation.

Returning to polymeric systems, experiments by Loo, Cohen, and Gleason used NMR to see enhanced chain mobility in the amorphous (glassy, non-crystalline) regions of nylon-6 under uniaxial tensile extension.<sup>29</sup> Colucci, McConnell, and McKenna took a different approach and observed the stress-induced volume relaxation of polycarbonate glasses.<sup>30</sup> Under both uniaxial tension and compression at strains less than yield, they observed faster volume relaxation with increasing strain. As the same results were obtained for compressive and tensile loads, they concluded that the magnitude of free volume in the sample is not the key factor that determines aging.<sup>30</sup> This indicates that stress induces mobility through another mechanism as will be discussed in Section 2.4.

For the rest of this section, I will discuss the experimental studies conducted by Mark Ediger's group on the effect of deformation on polymer glass mobility.<sup>31-34</sup> They studied the molecular mobility of glassy poly(methyl methacrylate) (PMMA) deformed under uniaxial tension using confocal microscopy to observe the recovery of photobleached rotational dyes that are sensitive to the local mobility of the surrounding PMMA matrix.<sup>31</sup> Creep experiments were performed where a constant force was applied to the PMMA glass at  $T_g - 19$  °C.<sup>32</sup> As the strain increased under the load, the molecular mobility increased as well. For stresses causing the sample to reach the flow regime, the mobility increased by two orders of magnitude, peaking at the highest strain rate. After loading stopped, the mobility gradually returned to its pre-deformed value once the sample aged to equilibrium.<sup>32,33</sup> The dye reorientation measurement yielded a distribution of relaxation times that could be fit with a Kohlrausch-Williams-Watts

stretched exponential equation  $r(t)/r(0) = e^{-(t/\tau)^\beta}$  where  $r(t)$  is the anisotropy decay function,  $t$  is time, and  $\tau$  is the characteristic relaxation time of the decay.<sup>31</sup> The KWW  $\beta$  parameter is a measure of how homogenous the dynamics of the sample are; a large  $\beta$  parameter approaching one returns the equation to a single exponential indicating homogenous relaxations.<sup>17,33</sup> As the mobility increased in the glassy PMMA deformed past yield, the KWW  $\beta$  parameter also increased, indicating a narrower distribution of dynamics, *i.e.* a more dynamically homogeneous material.<sup>33</sup> While the correlation between strain rate and mobility breaks down for multistep creep, indicating that no single mechanical variable predicts molecular mobility,<sup>34</sup> in single-step deformation experiments, the strain and strain rate determine the mobility of the glass.<sup>31-33</sup>

Ediger's group also explored the effects of deformation on PMMA glasses with different aging histories.<sup>33</sup> Struik proposed that deformation could erase aging and restore the mobility and energy of an aged glass to that of an unaged glass.<sup>46</sup> Lee and Ediger<sup>33</sup> found that deformation below yield (flow) of an aged glass only enhanced mobility during the deformation. After the deformation stopped, the mobility decreased with time as it had before the deformation began, following the same aging trajectory as an undeformed glass.<sup>33</sup> However, in the post-yield regime after the cessation of deformation, the mobility recovered with a different time dependence than an unaged glass. This suggests that post-yield deformation changes the state of the glass, altering the physical aging process, whereas pre-yield deformation does not.<sup>33</sup>

One of the long-standing debates concerning enhanced mobility in glasses under deformation is focused around the idea of mechanical "rejuvenation."<sup>33,40,47</sup> The central question is, can mechanical deformation erase aging history in the same way that thermal

annealing above the glass transition can? Are glasses deformed post-yield truly rejuvenated as thermal annealing would lead to? Lee and Ediger stated that their results were consistent with rejuvenation, however cautioned that they cannot rule out that thermally quenched glasses and mechanically deformed glasses may age to different equilibrium states.<sup>33</sup> In Section 2.4, this question will be addressed again.

Simulations in collaboration with Ediger's group also showed enhanced molecular mobility similar to that observed in experiments, with the added benefit that relaxation times can be directly obtained from the molecular dynamics simulation data.<sup>34,48-50</sup> Riggleman, Schweizer, and de Pablo revealed that enhanced molecular mobility is isotropic and uniform despite the application of a uniaxial deformation.<sup>49</sup> Further simulations also strengthened the finding of increased dynamic homogeneity under deformation. The fraction of particles involved in non-affine motion grew during a creep experiment, indicating that rearrangements occurred in larger clusters, and thus that dynamics became more homogeneous.<sup>50</sup> Another benefit of simulations is the ability to study mobility under compression (Ediger's films were 10 – 50 microns thick<sup>31</sup> and therefore difficult to compress without bending). In agreement with the experimental findings of Colucci, *et al.*,<sup>30</sup> Riggleman, *et al.* found that molecular mobility depended on the magnitude of the strain rate, and that mobility increased under compression even though the absolute volume decreased.<sup>48</sup> These results indicate that increased free volume is not the key factor responsible for increasing molecular mobility.

In summary, deformation has been shown to increase mobility in many glassy systems, both by experiments<sup>31-34</sup> and simulations.<sup>34,48-50</sup> A strong correlation between strain rate and mobility was observed for single-step deformation experiments.<sup>31-33</sup>

Similar enhancements in mobility were found by experiments<sup>30</sup> and simulations<sup>48</sup> for polymers deformed under both tension and compression, indicating that enhanced free volume was not the cause of the enhanced mobility. How can we then explain the enhanced molecular mobility seen in deformed glasses? Why do the underlying dynamics only appear to change after yield is reached? Theoretical work using the potential energy landscape framework has suggested that external deformation can alter the PEL.<sup>35–40</sup> Under post-yield deformation, simulations have shown that enhanced mobility reflects a transition to a higher energy state,<sup>39–43,48–50</sup> as will be discussed below.

## 2.4 Stress-Induced Landscape Tilting

One possible explanation for the enhanced molecular mobility observed upon deformation is that the potential energy landscape is altered by the deformation. The idea that stress can lower energy barriers between minima was originally proposed by Eyring in 1936 to explain the increase in viscosity upon shearing.<sup>44</sup> In the Eyring model, stress is assumed to linearly decrease the activation energy such that the forward hopping rate (toward a lower energy minimum) is enhanced as  $k_f = \exp(-(E - \sigma V)/k_B T)$  where  $E$  is the activation energy in the absence of stress,  $V$  is the activation volume,  $k_B$  is Boltzmann's constant and  $T$  is temperature. Similarly, the backward hopping rate is lowered by adding  $+\sigma V$  to the activation energy. The net effect is to “tilt” the potential energy landscape, though this terminology was not used until later.<sup>35,36</sup> The relaxation rate, an indicator of the molecular mobility, is then predicted to increase nearly linearly with stress.<sup>44</sup>

Others, such as Daniel Lacks and co-workers, have built substantially upon Eyring's idea.<sup>39–43,45</sup> Malandro and Lacks<sup>39</sup> proposed a “self-diffusion” mechanism by

which shear induces mechanical instabilities in the potential energy landscape, as shown in Figure 2.2. They also conducted non-equilibrium molecular dynamics simulations of Lennard-Jones particles at zero temperature to observe the dynamics and potential energy of the system. As strain was applied, the potential energy barrier height decreased to zero at a given strain. At this strain, they observed a large jump in the mean-square displacement of particles, indicating shear-induced transitions between metabasins,<sup>39</sup> as illustrated in Figure 2.2a.

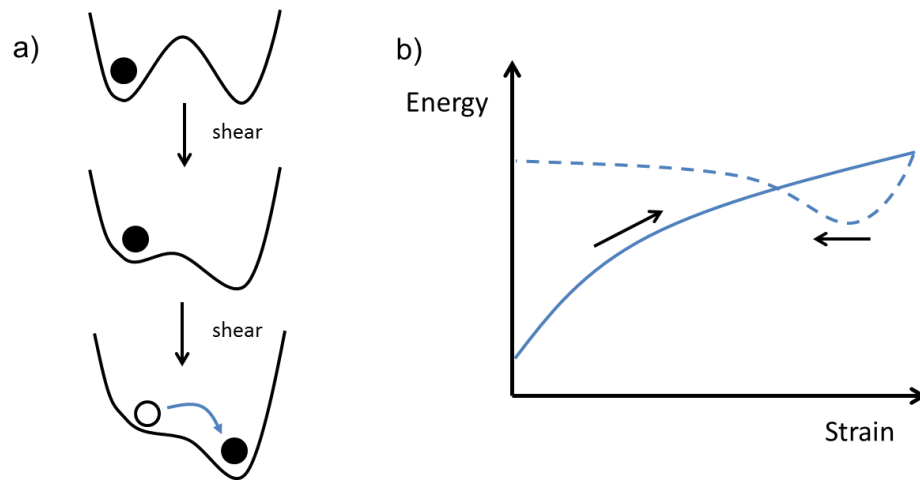


Figure 2.2: a) Schematic of changes to the potential energy landscape upon mechanical deformation that reduces the barriers for hopping events, based on Fig. 3 from Malandro and Lacks.<sup>39</sup> b) Schematic depiction of potential energy vs. strain for large deformation, based on Fig. 4 from Chung and Lacks.<sup>41</sup> The solid line shows the increase in potential energy upon loading while the dashed line shows how the energy remains high even upon unloading.

Lacks and Osborne focused on the effects of applying a cyclic shear to a binary Lennard-Jones glass.<sup>40</sup> The inherent energy of the system increased with the application of shear as one energy barrier after another was overcome, as depicted in Figure 2.2b, allowing the system to transition to a *higher* energy state that had previously been inaccessible.<sup>40</sup> The change in energy is smooth in Figure 2.2b as the barrier heights at finite temperatures do not need to go to zero, as depicted in Figure 2.2a, because the

system can hop over barriers with heights comparable to  $k_B T$ .<sup>40</sup> For large strains, the final energy of the system after loading and unloading was higher than it started out, as shown in Figure 2.2b. For smaller strains, the system was driven lower in the potential energy landscape, reminiscent of over-aging.<sup>40</sup> Further simulations conducted by Chung and Lacks in polymer glasses also showed that deformation can drive the polymer glass into a higher energy state by lowering energy barriers between potential energy minima.<sup>41-43</sup> They also observed enhanced mobility in their simulations of polymer glasses from the mean-squared displacement of individual particles under deformation.<sup>41-43</sup> As discussed earlier, rejuvenation is the idea that mechanical deformation can erase past history similar to annealing at higher temperatures. These simulations of Lennard-Jones and polymer glasses show that the path the system takes through the potential energy landscape under deformation is very different than a simple increase in temperature.<sup>39-43</sup> At low strains, the system is driven deeper into the potential energy landscape, consistent with the idea of over-aging.<sup>40</sup> At higher strains, above yield, the system is driven into a higher potential energy state within a different metabasin than it was cooled into.<sup>40,43</sup> The work of Lacks and coworkers provides evidence for deformation altering the potential energy landscape and thereby changing the dynamics of the glass trapped within the altered PEL.

For a more molecular view of stress altering the PEL, Chen and Schweizer developed a slightly coarse grained segmental statistical mechanical model of stress-induced acceleration of thermal barrier hopping.<sup>35-38</sup> Unlike Eyring,<sup>44</sup> who modeled stress as a linear decrease in energy barrier height, Chen and Schweizer introduced the external force as work contributing to the non-equilibrium free energy.<sup>37</sup> Their model

can be tuned to individual polymers as the non-equilibrium free energy can be determined from the experimentally measurable structure factor. They find that at temperatures below a dynamic crossover temperature (well above  $T_g$ ), a temperature-dependent barrier in the free energy emerges.<sup>37</sup> As stress is applied, the barrier height decreases and reaches zero when the applied stress equals the absolute yield stress. The logarithm of the relaxation time decreases sub-linearly with increasing applied stress. The experimentally defined yield stress is smaller than the absolute yield as viscous and strain rate effects that are not accounted for in the model promote yielding in real systems. They derive an analytic expression for the yield stress in terms of the absolute yield stress, the temperature dependent barrier height, the strain rate, and the barrier activation energy (that relates to a glass's fragility).<sup>37</sup> Chen and Schweizer's landscape tilting model offers predictions of molecular mobility for real polymer glasses under deformation.<sup>35-38</sup>

The idea of stress-induced landscape tilting can be applied to explain many of the findings of Mark Ediger's group.<sup>31-34</sup> Enhanced mobility was shown in simulations to correlate well with the system's position on the potential energy landscape, as given by its inherent energy.<sup>49,51</sup> Higher mobility as strain increased, either in compression or extension, was associated with higher potential energy.<sup>34,49</sup> Lee and Ediger discussed their study of deformed, aged glasses in the context of the PEL as well.<sup>33</sup> They stated that the KWW  $\beta$  parameter can indicate the position of the system on the landscape at a given energy. As deformation changes the KWW  $\beta$  parameter, the system is in a different location on the PEL than it was when aging. As the KWW  $\beta$  parameter decreases, indicating a more homogenous glass, they argue that deformation moves the

system to a higher energy than a thermal quench would.<sup>33</sup> Additionally, Riggleman, Schweizer, and de Pablo<sup>49</sup> fit the predictions of Chen and Schweizer's model<sup>37</sup> to the simulated relaxation time vs. applied stress and found qualitative agreement. Quantitative differences were expected as the theory does not account for stress-induced structure changes that were observed in the simulations.<sup>49</sup>

In summary, post-yield deformation of glasses increases mobility, changing the physical aging trajectory even after the stress is removed.<sup>33</sup> Rather than simply increasing the potential energy of the glass as an increase in temperature would, deformation acts to tilt the potential energy landscape.<sup>35-40,44</sup> This tilting has been proposed to allow the system to overcome lowered energy barriers and move into a higher potential energy metabasin than the original metabasin the glass cooled into.<sup>40</sup> In Chapter 4, I will utilize these ideas of stress-induced landscape tilting when interpreting my results on the effect of stress applied during glass formation on physical aging of the subsequent glass.

## 2.5 Stresses in Glass Formation

In Chapter 4, I will present experimental results on the effect of stress applied to polymer films during the glass formation process.<sup>52</sup> As summarized in Section 2.3, many experiments and simulations have examined the impact of stress and strain on the glass once it is already formed.<sup>19,28-34,48-50</sup> However, no systematic study of the effect of stress during glass formation on the stability of the subsequent glassy state has been conducted even though stress is often present during glass formation. Extruding techniques apply large stresses to polymers as they are sheared and deformed into the desired shape and thickness. Stresses are also present in more subtle ways. Polymers are often molded,

solution-cast, or spin-coated in contact with a solid support such as glass or a metal. They are then heated above the polymer's glass transition temperature, to erase thermal history as well as to fill the mold, and finally cooled into the glassy state. In this section, I will discuss the origin and magnitude of stress imparted to polymer films during the glass formation process upon cooling for films adhered to an underlying substrate.

While cooling through the glass transition temperature, stress can build up in the polymer film due to the differences in thermal expansion of the polymer and the support. Nearly all materials contract as they cool and the thermal expansion coefficient,  $\alpha$ , is defined by the change in volume with temperature:  $\alpha = \frac{1}{V} \left( \frac{\partial V}{\partial T} \right)$ .<sup>53</sup> This volume change with temperature results in a strain given by the thermal expansion coefficient and the change in temperature:  $\varepsilon = \alpha \Delta T$ .<sup>53</sup> Polymers tend to have high thermal expansion coefficients, about two orders of magnitude higher than glasses and most common metals.<sup>54,55</sup> As a polymer is cooled on such a support it cannot contract fully as it is pinned to the rigid support undergoing less contraction. This mismatch in contraction results in a stress in the polymer. Even if the polymer is supported by other polymers stress can still be exerted due to smaller differences in thermal expansion coefficient. The exact form of the stress equation depends on the geometry of the support and the polymer. For example, a polymer film adhered to a substrate experiences a biaxial tensile stress as it cannot contract in the plane of the substrate. The in-plane ( $xy$ ) strain,  $\varepsilon$ , is equal to  $(\sigma + \nu\sigma)/E$  where  $E$  is Young's modulus and  $\nu$  is Poisson's ratio, if the stress,  $\sigma$ , in  $x$  and  $y$  are the same.  $E/(1+\nu)$  is called the "biaxial modulus."<sup>53</sup> From Hooke's law, strain is equal to the modulus multiplied by stress. Recall, that  $\varepsilon = \alpha \Delta T$ . Therefore, the stress is then given by

$$\sigma = \frac{E}{1-\nu}(\alpha_{polymer} - \alpha_{substrate})\Delta T \quad \text{Eq. 2.1}$$

where  $E$ ,  $\nu$ , and  $\alpha$  are all functions of temperature.<sup>53</sup> In Chapter 3, this geometry will be discussed in more detail. Above  $T_g$ , little or no stress builds up as the modulus is small.<sup>56</sup> Stress can relax with time as  $\sigma(t) = \sigma_0 \exp(-t/\tau)$  where  $\sigma_0$  is the initial stress and  $\tau$  is a stress relaxation time constant.<sup>57</sup> Above  $T_g$ , stress may continue to relax on cooling if the cooling rate is slower than the relaxation time. In Chapter 5, we will measure the stress build up as a function of temperature for a free-standing polymer film held between two opposite ends of a rigid support. In this geometry, the film experiences a uniaxial stress equal to  $\sigma(T) = E(T)\Delta\alpha\Delta T$ .<sup>53</sup>

Within the literature, there have been some investigations of stress buildup in polymers. Zhao, *et al.*<sup>58</sup> directly observed the stress build up on cooling in PS films spin cast on silicon substrates by measuring the bending of the substrate. Above the glass transition temperature, there was no stress in the PS film. As the PS film cooled to room temperature, stress began to build up below the glass transition temperature, reaching 15 MPa for bulk films.<sup>58</sup> Others have investigated residual stress from spin coating as a function of thermal annealing time in thin PS films using surface wrinkling<sup>59</sup> or cantilever bending<sup>60</sup> to quantify stress. The stress in the film from spin coating was initially high (up to ~140 MPa<sup>60</sup>) and decayed over time as the polystyrene film was annealed above  $T_g$ .<sup>59,60</sup> In the surface wrinkling experiments of Chung, *et al.*,<sup>59</sup> after 168 hours of annealing the residual stress of PS films spin cast and quenched on mica plateaued to a constant value that they attributed to stress build up from the thermal expansion coefficient difference between PS and the mica support, following Equation 2.1 above.

In summary, large stresses can build up on cooling polymer films due to thermal expansion coefficient mismatch between the polymer and its necessary support. The effects of this stress on the physical aging of the polymer have not been explored systematically. Below, in Section 2.6, I will present studies of accelerated physical aging of polymer glasses with decreasing film thickness. In Chapter 3, I will relate experiments that show, by process of elimination, that stress present during the glass formation process likely explains the accelerated physical aging observed.<sup>61</sup> The experiments in Chapter 4 confirm that stress present during glass formation leads to faster physical aging.<sup>52</sup>

## **2.6 Anomalous Physical Aging and Mechanical Properties in Polymer Thin Films**

### *2.6.1 Accelerated Physical Aging with Decreasing Film Thickness*

Many studies have been conducted over the past 20 years, beginning with Keddie, Jones, and Cory's seminal work,<sup>62</sup> investigating the properties of polymers under confinement. It has been observed that the free surface of polymer films has extra mobility and resembles a liquid-like layer.<sup>63</sup> As film thickness is decreased the free surface becomes a larger portion of the film. Therefore, reductions in the glass transition temperature have been observed for free-standing polymer films<sup>64</sup> and for supported polymer films that do not have specific interactions with the substrate they are on.<sup>65</sup> Confinement is of interest not just as a means to study the glass transition but also due to the increasing use of confined polymers in technological applications. Gas separation membranes utilize thin polymer films as the separation layer while thin films are used as templates for nanolithography.

The physical aging behavior of confined polymer films has been studied in our lab<sup>66</sup> and by others.<sup>67-71</sup> Volumetric physical aging rate was originally defined by Struik<sup>7</sup> as  $\beta = -1/V_{\infty} dV/d(\log t)$  where  $V_{\infty}$  is the equilibrium volume of the glass. Baker, *et al.*,<sup>72</sup> established a streamlined ellipsometry technique in our lab to measure physical aging rate from the time-dependent film thickness of a polymer film pinned to a silicon wafer. As the film is adhered to the wafer, contraction in volume only occurs in the thickness of the film, perpendicular to the substrate. Thus, the physical aging rate can be defined as  $\beta = -1/h_{\infty} dh/d(\log t)$ . The equilibrium film thickness is difficult to determine so Baker, *et al.* instead proposed to normalize by the well-defined film thickness at an aging time of 10 minutes, resulting in  $\beta = -1/h_0 dh/d(\log t)$ .<sup>72</sup> This measure of physical aging rate agrees well with physical aging rates determined from dilatometry.<sup>8,72</sup> Using this technique, the effect of confinement on physical aging rate was studied by Pye, Rohald, Baker, and Roth.<sup>66</sup> They studied PS thin films supported on silicon wafers 29 – 2700 nm thick. Physical aging rate was found to decrease with decreasing film thickness for PS films thinner than ~60 nm.<sup>66</sup> They correlated the decrease in average physical aging rate with the gradient in local  $T_g$  upon confinement.<sup>66</sup> Prior studies of physical aging of confined polymers also observed reduced physical aging for films thin enough to exhibit  $T_g$  reductions.<sup>67-71,73</sup>

In contrast, physical aging studies conducted on free-standing gas permeation membranes have shown an increase in physical aging rate with decreasing film thickness for films “under confinement” thinner than several microns.<sup>11,12,74-81</sup> Confinement effects are of interest as gas permeation membranes are often less than 100 nm thick.<sup>12</sup> Physical aging greatly affects performance as the permeability and selectivity of the membrane are

extremely sensitive to changes in free volume.<sup>12</sup> Small decreases in fractional free volume (< 1%) can lead to greater than 50% decrease in permeability.<sup>11,12</sup> Glassy polymers with rigid backbones and high free volume are often used as gas permeation membranes. Polysulfone (PSF),<sup>11,12,74</sup> polyimide,<sup>11,74</sup> poly(2,6-dimethyl-1,4-phenylene oxide) (PPO),<sup>11</sup> polynorborene,<sup>75</sup> and poly(1-trimethylsilyl-1-propyne)<sup>76</sup> have all been shown to exhibit accelerated physical aging with decreasing film thickness.

For the rest of the discussion on physical aging of gas permeation membranes, I will focus on the work of Don Paul and coworkers studying PSF. They characterized physical aging by the change in gas permeability over time<sup>11,12,78</sup> or the change in index of refraction as measured by ellipsometry.<sup>79,80</sup> Polymer films were spin-cast or solution cast on silicon then floated off the substrate onto rectangular wire frames such that the film was held on two sides.<sup>11</sup> Films were then annealed above  $T_g$  to erase thermal history and cooled to room temperature in the free-standing state. Films were then stored at the aging temperature (35 °C,  $T_g - 151^\circ\text{C}$ ) for the desired aging time. After aging, the samples were prepared for the gas permeation measurement. In order to perform the measurement, the free-standing films were masked by mounting the film onto an anodized disk and sealing the edges with aluminum tape to create a well-defined surface area.<sup>11</sup> Long aging from weeks to months were required to ensure that the aging time was sufficiently longer than the masking and measurement time of ~1 hour.<sup>11</sup> Permeability vs. aging time curves were collected by measuring the permeability of different films aged for various times.<sup>11</sup> The permeability was found to decrease logarithmically with aging time. As the film thickness was decreased below several microns, the absolute change in permeability over time increased, indicating that

accelerated (faster) physical aging occurred for films thinner than several microns.<sup>11,12,78</sup> For example, the permeability after 4000 hours for a 413 nm thick PSF film was ~35% lower than the permeability of a 35.6 micron thick film after the same aging time.<sup>11</sup> Films as thick as 8.5 micron had an accelerated aging rate resulting in an ~5 % faster reduction in permeability compared to bulk.<sup>11</sup>

The other technique used by Paul and coworkers to quantify physical aging was to measure the time-dependent index of refraction of aging polymer films using ellipsometry.<sup>79,80</sup> Similar to the sample preparation for gas permeation measurements,<sup>11</sup> films that were later measured with ellipsometry were also annealed, quenched, and stored at the aging temperature in the free-standing state before transfer to silicon for the measurement.<sup>78</sup> The index of refraction was then measured for different films aged for times from 0.2 hours to 4000 hours.<sup>79,80</sup> As polymer glasses densify over time due to structural relaxation,<sup>9,82</sup> the index of refraction increases. Huang and Paul observed that the slope of the index of refraction vs. aging time increased with decreasing film thickness, indicating accelerated physical aging for films aged at temperatures from 35 to 55 °C.<sup>79,80</sup> Only films from 375 – 1000 nm thick were measured using ellipsometry, but they were determined to be in good agreement with measures of accelerated aging seen by permeation measurements.<sup>79,80</sup>

The observed length scale of several microns below which accelerated physical aging is observed<sup>11,12,74–81</sup> is much larger than the length-scale where  $T_g$  reductions are observed.<sup>66–71,73</sup> As described above, Pye, *et al.* observed a *decrease* in physical aging rate for PS films less than 60 nm thick tied to the reduction in  $T_g$ .<sup>66</sup> Rowe, *et al.* observed a decrease in relaxation times associated with physical aging measured from gas

permeability and positron-annihilation spectroscopy for ultrathin PSF films thinner than ~100 nm and linked them to reductions in  $T_g$ .<sup>71,73</sup> As the glass transition is not reduced for films several microns thick and an increase in physical aging rate is observed, another mechanism has been proposed to explain accelerated aging.

### 2.6.2 Free Volume Diffusion Model

Free volume can be defined as the occupied volume of the molecules subtracted from the total volume of the sample.<sup>82</sup> Free volume is necessary for molecular rearrangements to occur, if no free volume existed molecules would be incapable of moving past each other. Struik<sup>82</sup> described structural relaxation in terms of the evolution of free volume. The out of equilibrium glassy system is driven to rearrange and densify into a lower energy state. The mobility, or amount of rearrangements allowed, is determined by the available free volume. As the free volume decreases with time, the mobility also decreases, causing the system to have less ability to densify over time.<sup>82</sup> This negative feedback loop is reflected in the logarithmic time dependence of the volumetric decrease associated with structural relaxation. “Lattice contraction” describes a uniform free volume relaxation resulting in chains moving closer together over time.<sup>83</sup>

The idea of free volume diffusion has been used by Paul and coworkers to explain the observation of accelerated physical aging with decreasing film thickness.<sup>84,85</sup> The basic idea proposed by Alfrey, *et al.* is that free volume pockets can diffuse through the polymer<sup>86</sup> at a rate limited by the chain segmental mobility.<sup>83</sup> The diffusion constant depends on the amount of free volume and the driving force for diffusion is the gradient in free volume, with less free volume at the surfaces of the film. In the free volume diffusion model, free volume annihilates after some internal length scale. McCaig and

Paul used this free volume diffusion model to model the film thickness dependent aging seen in gas permeability measurements where the internal diffusion length scale was the film thickness.<sup>85</sup> Therefore, over a given amount of time, thinner films have more free volume diffuse out of them than thicker films, leading to accelerated physical aging.<sup>84,85</sup>

However, several studies contradict this interpretation. From the free volume diffusion model, supported films should also exhibit faster physical aging with decreasing film thickness as they have one free surface for free volume to annihilate at. However, as mentioned above, studies only found reduced physical aging rate for confined, supported polymer films.<sup>66-69</sup> Measurements of free-volume as a function of depth within a polymer film using positron annihilation spectroscopy found that although the free volume pockets were smaller near the surface, the size and number of free volume holes remained constant with aging time.<sup>73</sup> This is contrary to the predictions of the free volume diffusion model used to fit the gas permeability aging data.<sup>85</sup> As discussed in Section 2.3, experiments measuring volume relaxation of polymers under compression saw enhanced relaxation even though the free volume was reduced.<sup>30</sup> Enhanced mobility under compression was also observed in simulations.<sup>48</sup> In Chapter 3, I will present arguments for an alternative explanation for the film thickness dependent physical aging rate observed in films annealed and quenched in the free-standing state for gas permeation measurements.

### *2.6.3 Rubbery Stiffening in Polymer Thin Films*

In Chapter 4, we will apply stress to polymer films above the glass transition temperature. Above  $T_g$ , the polymers we will use have mechanical integrity and can support stress due to entanglements, which temporarily act like effective cross-links and

prevent the chains from flowing past each other on time scales less than the reptation time.<sup>87,88</sup> Here, I will discuss studies conducted above  $T_g$  that have observed an unexpected stiffening of thin films for thicknesses less than 200 nm.<sup>89-96</sup> The magnitude and film thickness dependence of the stiffening differ from study to study and polymer to polymer but the overall trend of stiffening is observed<sup>89-92,95,96</sup> except for Bodiguel and Fretigny who claim they see no change with confinement.<sup>93,94</sup>

Greg McKenna's group at Texas Tech has conducted many studies measuring the rubbery plateau creep compliance of thin polymer films using a nanobubble inflation technique they developed.<sup>89-91</sup> A thin polymer film was draped over a gold-coated silicon substrate with 1.2 micron sized holes. Pressure was applied to one side of the film resulting in a nearly constant biaxial stress on the free-standing films spanning the holes.<sup>89</sup> Creep was observed by measuring the profile of the bubble formed using an AFM.<sup>89</sup> In this manner, polystyrene,<sup>90</sup> polyvinyl acetate (PVAc),<sup>89,90</sup> poly(butyl methacrylate) (PBMA),<sup>91</sup> and polycarbonate (PC)<sup>91</sup> films from 10 – 200 nm in thickness were studied. Stiffening of up to 1000x for films 10 nm thick (1000x smaller creep compliance) at temperatures just above  $T_g$  was reported. The dependence of creep compliance on film thickness followed a power law. PS, PVAc, and PC had similar film thickness dependencies on creep compliance despite having different  $T_g$  reductions. PBMA also followed a power law, but with a shallower slope resulting in less stiffening. Bulk creep compliance was projected to be reached for films ~300 nm thick, however this was not experimentally verified as the membrane assumption necessary for their calculation of stress on the film breaks down above ~200 nm in film thickness. Another interesting note is that they do not observe flow in many of their polymers.<sup>91</sup>

Karim and McKenna have also observed stiffening in polymers in the rubbery regime using a nanoembedding technique.<sup>96</sup> Silica or gold nanoparticles were placed on the surface of a thin film above its  $T_g$  and the height of the nanoparticle was observed as it sank into the polymer film, from which the shear creep compliance can be extracted.<sup>96</sup> For poly( $\alpha$ -methylstyrene), a polymer without enhanced surface mobility according to Paeng & Ediger,<sup>97</sup> the creep compliance was reduced 10x from the bulk value.<sup>96</sup> (However,  $T_g$  reductions have been measured for supported films of P $\alpha$ MS.<sup>97</sup>) Above  $T_g$ , the amount of stiffening was approximately constant with increasing temperature.<sup>96</sup>

Other methods have also been used to investigate the effects of confinement on modulus. Rowland, *et al.*, observed stiffening for PS above  $T_g$  that was squeezed into a mold.<sup>92</sup> As the film thickness decreased (and strain increased), the confined PS melt resisted flow more than predictions based on bulk parameters would suggest. They observed up to 100x smaller creep compliance, however, they did not discuss this result and instead focused on PS squeezed below  $T_g$ .<sup>92</sup> Evans, *et al.*, reported stiffening as measured by a 3x longer relaxation time of surface capillary waves for 29 nm thick compared to 115 nm thick films.<sup>98</sup> Interestingly, confinement effects disappeared for temperatures above  $T_g + 40$  °C.<sup>98</sup>

Dewetting experiments of PS floating on glycerol have also been used to interrogate the creep compliance of thin films. A biaxial compression in the plane of a glycerol/PS surface or uniaxial tension perpendicular to the support drove the creep. Observations of the shrinking area of the film as it dewetted led to a measurement of the creep compliance. Experiments by Bodiguel and Fretigny found no change in creep compliance with decreasing film thickness and observed a very small (< 5 °C) decrease

in  $T_g$  for a 20 nm thick film.<sup>93,94</sup> Wang and McKenna<sup>95</sup> repeated these experiments but included a non-constant stress term due to the increase in film thickness as the film dewets in their analysis. This led them to observe stiffening of up to two orders of magnitude for 4 nm thick films. In comparison with the nanobubble inflation method, this effect is an order of magnitude or more smaller than expected. The compliance measured was also much higher than in the nanobubble inflation experiments such that larger than bulk compliance was measured for films greater than 10 nm thick.<sup>95</sup>

One possible cause for stiffening has been proposed by Ngai, *et al.* that specifically tried to address McKenna's nanobubble inflation experiments.<sup>99</sup> Different relaxation regimes are dominated by different motions within the polymer. The timescale for glassy behavior is determined by the timescale of cooperative segmental relaxation<sup>100</sup> (a segment being a few monomers) which is called the  $\alpha$ -relaxation. Sub-Rouse modes are proposed to occur on slightly longer timescales and have been proposed to correspond to the motion of several monomers along the chain but less than a single Rouse mode submolecule.<sup>101</sup> Rouse modes occur on even longer timescales and more monomers participate. These three different modes are responsible for the compliance measured in the softening dispersion – the region between the glassy and rubbery plateaus. Ngai, *et al.* proposed that as film thickness is decreased, extra constraints on molecular motion shift  $\alpha$ -relaxations and sub-Rouse modes to shorter times, increasing the separation between  $\alpha$ -relaxations, sub-Rouse modes, and Rouse modes.<sup>99</sup> They propose that while Rouse modes are not affected by confinement as no cooperativity is associated with them, shorter relaxation times ( $\alpha$ -relaxations and the lower sub-Rouse modes) are shifted more than longer relaxation times. Stiffening is therefore accounted for because the thinnest

films would be dominated by the shifted  $\alpha$ -relaxations which have a corresponding lower creep compliance than sub-Rouse and Rouse modes.<sup>99</sup> Ngai, *et al.*<sup>99</sup> used this conceptual framework along with their Coupling model to explain the stiffening measured by the nanobubble inflation technique. However, the Coupling model, when applied to Pye and Roth's observation of two  $T_g$ s in free-standing, high molecular weight, confined PS films,<sup>102</sup> breaks down.<sup>103</sup> The upper transition Pye and Roth see is predicted by the Coupling model to be a signature of sub-Rouse modes and not a "genuine" glass transition.<sup>104</sup> Pye and Roth later observed physical aging below the upper transition and above the lower transition, indicating that the upper transition is a glass transition as physical aging would not be observed above  $T_g$ .<sup>103</sup>

## 2.7 Summary

In this chapter, I have summarized the existing research literature concerning deformation induced mobility in glasses and how the potential energy landscape "tilting" mechanism can be used to interpret enhanced mobility. These studies focused on deforming glasses nominally formed stress-free. However, stress is often present during the glass formation process due to thermal expansion coefficient mismatch between polymer and support. A systematic study of the effect of stress applied during the glass formation process on physical aging will be presented in Chapter 4. In this chapter I also described measurements of accelerated physical aging with decreasing film thickness for films much thicker than the film thickness at which  $T_g$  reductions are seen. These observations were not satisfactorily explained by free volume diffusion. In Chapter 3, I will present an investigation into the causes of this accelerated aging.

# Chapter 3

## Physical Aging Behavior of Glassy Polymer Films: Effect of Quench Conditions

A version of this chapter was published as L. A. G Gray, Suk W. Yoon, William A. Pahner, James E. Davidheiser, Connie B. Roth, *Macromolecules*, 45, 1701 – 1709, 2012.

“Copyright 2012 by the American Chemical Society”

### 3.1 Synopsis

In this chapter I will detail our efforts to probe the cause of the “accelerated” physical aging rate of polymer films with decreasing film thickness, as observed by the gas permeation community. These deviations in aging rate from bulk behavior occur at film thicknesses of several microns, much larger than other confinement length scales seen in the literature and in our lab. Here, I address how we systematically explored the effects of molecular structure, quench depth below  $T_g$ , and quench rate through  $T_g$ . We demonstrated that how you hold the film during the quench, either free-standing or supported, affects the film thickness dependence of the aging rate. Films quenched in a free-standing state exhibited faster aging rates with decreasing film thickness whereas supported films showed no thickness dependence to the aging rate for films thicker than 100 nm. We also found that films quenched slower through  $T_g$  age slower if the cooling rate is less than  $\sim 100$  °C/min. However, this does not explain the accelerated physical aging observed for free-standing films as free-standing films age slower than supported

films even though the quench rate is much faster for free-standing films. The other possible factor that could be different during the quench for free-standing vs. supported films is the stress imposed on the film during the quench. Stress on a supported film is due to the thermal expansion coefficient mismatch between the support and film and is independent of film thickness. Stress on a free-standing film however depends inversely on film thickness. From the studies discussed below, we concluded that different sample holders may impose different stresses to the film that affect the subsequent physical aging.

## 3.2 Introduction

Glassy materials are inherently unstable, existing as ‘frozen liquids’ below their glass transition temperature. Structurally trapped far from equilibrium, the system uses what little mobility that is available to decrease its free volume in a process called structural relaxation.<sup>7-9,72</sup> Associated with this slow densification of the material is a host of other property changes, such as increased modulus<sup>10</sup> and decreased permeability,<sup>11,12</sup> that fall under the general heading of physical aging. Within the potential energy landscape picture,<sup>2,3</sup> a glassy system can be viewed as being trapped within a local energy minimum with the aging process driving it deeper in towards a given minimum.<sup>40</sup> Numerous fundamental issues about the nature of glasses still remain unresolved:<sup>33,47,105</sup> What traps a glassy system within a particular energy minimum? What can be done to move the system within this potential energy landscape, say from one minimum to the next? For instance, what effect does stress or deformation have on the glassy material? And above all, what about the microscopic structure of the system determines the state, dynamics, and stability of the material?

Glassy systems have been studied in confined geometries as a means of probing the essential length scales and elucidating the underlying properties of the glass. Polymer thin films, with their ease of fabrication and industrial importance, have been a natural venue for such studies.<sup>106,107</sup> Over the past decade, several studies have been able to link various anomalous physical aging characteristics to boundary effects associated with the large surface-to-volume ratio of thin films.<sup>66–69,71,108–110</sup> For length scales of order 100 nm or less, the presence of a free surface or attractive substrate interaction can result in  $T_g$  changes near the boundary, and hence concomitant changes in the physical aging rate.<sup>66</sup> For example, the physical aging rate of supported polystyrene (PS) films on silicon decrease for films thinner than 100 nm, as shown by our lab,<sup>66</sup> corresponding to the same length-scale at which  $T_g$  decreases due to the presence of the free surface.<sup>66–69</sup> However, there exists a second large body of work whose studies have observed deviations from bulk physical aging rates for film thicknesses already several microns in thickness.<sup>11,12,74–81,84</sup> The cause of these unresolved effects at this much larger length scale of several microns is the focus of the present study.

Over the past 20 years, observations of increased physical aging rate for micron-thick polymer films as film thickness is decreased have been made by the gas permeation community, a phenomenon that has been termed “accelerated” physical aging.<sup>11,74,76–81</sup> The polymers used in gas permeation studies include polysulfone (PSF),<sup>11,74</sup> polyimide,<sup>11,74</sup> poly(2,6-dimethyl-1,4-phenylene oxide),<sup>11</sup> polynorborene,<sup>75</sup> and poly-1-(trimethylsilylyl)-1propyne.<sup>76</sup> These industrially relevant polymers typically have high free volume, desired for good permeability, and relatively high  $T_g$ s above 150 °C. These properties arise from the chemical structure of the polymers which contain stiff aromatic

groups in the backbone of the polymer chain, resulting in poor packing and therefore high free volume. Although physical aging results in very small decreases in free volume (typically <1%),<sup>72,84</sup> as gas permeability is extremely sensitive to free volume<sup>11</sup> this small decrease in free volume can lead to > 50% decrease in gas permeability.<sup>11,12</sup> To increase overall permeability, gas separation membranes can be thinner than 100 nm in thickness.<sup>12</sup> Thus the long-term stability of thin glassy membranes is of great interest.

What is most surprising about the gas permeation studies is that the accelerated physical aging behavior is observed at micron length scales, i.e., deviations of the aging rate from bulk behavior with decreasing film thickness occur already at film thicknesses of several microns.<sup>11,74,76-81</sup> This length scale is much larger than the ~100 nm at which  $T_g$  and other physical aging effects have been observed in polymers due to boundary effects.<sup>66-69</sup> Frequently, these studies at the smaller length scale observe reduced or suppressed physical aging, but they are typically done on flexible, C-C backbone polymers with lower  $T_g$ s, and perhaps most significantly on films supported on rigid substrates. Thus, the cause of the anomalous physical aging characteristics at micron length scales continues to be a mystery, with numerous possibilities remaining unexplored. (1) Are there fundamental differences in how packing is frustrated in the glassy state associated with the molecular structure of the polymer chain? Do stiff backbone chains pack differently than flexible, C-C backbone polymers limited by bulky side-groups leading to distinct free volume distributions that age differently? Perhaps the depth below  $T_g$  at which the material is aged plays a significant role (high vs. low  $T_g$  polymers)? (2) Are there differences associated with the experimental techniques and

sample preparation used? (3) Are there hidden or unintended stresses imparted to the films (e.g., spin-coating stresses)?

In order to determine the cause of the accelerated physical aging seen with decreasing film thickness at micron-length scales, we systematically varied polymer chemical structure and quench conditions. Our recently developed streamlined ellipsometry procedure<sup>72</sup> is able to characterize the physical aging rates of polymer films with varying chemical structure. Here we show that faster physical aging rates with decreasing film thickness at large micron length scales can be observed in a flexible C–C backbone polymer, with a lower  $T_g$  than the polymers typical of separation membranes, when these films are quenched in a free-standing state matching the sample preparation procedure used in the gas permeation work. Based on process of elimination, we believe the film thickness dependence of the aging rates observed at micron length scales in the gas permeation studies is due to small differences in stress inadvertently applied to the free-standing films by the film support during the thermal quench. Since all thin films must be supported in some manner, understanding the unintended stresses resulting from thermal expansion mismatches between film and support are important. These studies indicate that even small stresses, only present during the formation of the glassy state, can strongly influence the subsequent stability of these films even when this stress is removed during the aging process. We find that different quench conditions trap the glassy films into different states (potential energy minima) influencing the subsequent physical aging rate of the films. An improved understanding of how quench conditions affect glass formation could be used to control glassy film properties leading to materials with improved stability.

### 3.3 Experimental Methods

For the following studies, two different polymers were used: polystyrene (PS),  $M_n = 132$  kg/mol and  $M_w = 289$  kg/mol, and polysulfone (PSF),  $M_n = 26.9$  kg/mol and  $M_w = 67.5$  kg/mol that were purchased from Scientific Polymer Products. Polymer films were made by dissolving PS in toluene or PSF in cyclopentanone and spin-coating onto silicon wafers (to make supported films) or onto freshly cleaved mica substrates (to make free-standing films). All films were annealed after spin coating for at least 12 hours at 120 °C for PS or 150 °C for PSF in order to remove residual solvent from the film. Free-standing PS films were then created by floating the hydrophobic PS films from the hydrophilic mica onto water. The films were then caught with a choice of frame: either a springy stainless steel wire frame, a rigid stainless steel, or rigid nylon-6,6 frame. The wire frames were rectangular, approximately 2.0 x 2.5 cm in extent, and made from 0.009 in. diameter stainless spring steel wire. The rigid frames had circular (1.9 cm in diameter) or rectangular (1.3 x 2.5 cm) holes punched from 0.020 in. thick nylon-6,6 or 0.004 in. thick stainless steel sheets. Pictures of the three different free-standing geometries are shown below in Figure 3.1.

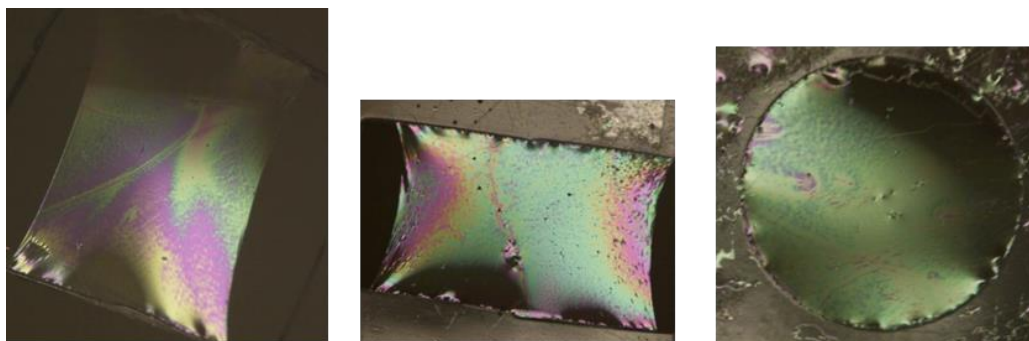


Figure 3.1: Depictions of the free-standing frames with PS films used in the following studies. From left to right: wire frame, rigid nylon frame with rectangular hole, rigid nylon frame with circular hole. The rigid stainless steel frames have the same dimensions and shape as the rigid nylon frames.

Immediately prior to the physical aging measurements, free-standing or supported films were annealed above  $T_g$  for 30 minutes. The films were then quenched to a temperature  $T_q$ , room temperature unless otherwise noted, by quickly removing the films from the oven and placing them in contact with a large aluminum block equilibrated to  $T_q$ . To control the quench rate of supported PS films a series of base plates with different heat transfer properties were used to change the cooling rate. Free-standing films were rapidly quenched by opening the door to the oven, thus allowing room temperature air to enter the chamber. All aging measurements were conducted in the supported state; free-standing films were gently transferred to a silicon wafer just prior to the aging measurement. The annealing and quench temperatures as well as the rate at which the films were cooled are all factors which we will explore below.

Immediately after quenching (and transferring to silicon wafer for the free-standing films) films were placed on the ellipsometer hot stage (Instec HCS 302) pre-equilibrated to the aging temperature. Physical aging rates are often quantified by measuring volume relaxation as a function of time that is a result of the densification which occurs during structural relaxation of the glass. The physical aging rate was determined by measuring the film thickness decrease over time using spectroscopic ellipsometry (J. A. Woollam M-2000). Ellipsometry measures the change in polarization of light after it is reflected off the sample, yielding two ellipsometric angles  $\psi(\lambda)$  and  $\Delta(\lambda)$ . The tangent of  $\psi$  is the ratio of the magnitudes of the total reflection coefficients while  $\Delta$  is the phase difference that occurs upon reflection.<sup>111</sup> The film thickness  $h$  and index of refraction  $n$  are calculated by fitting  $\psi$  and  $\Delta$  for wavelengths ranging from 400 – 1000 nm. The polymer film is modeled as a Cauchy layer with index of refraction  $n(\lambda)$

=  $A + B/\lambda^2 + C/\lambda^4$  atop a native silicon oxide layer 2 nm thick on a silicon wafer. As the polymer films are pinned to the silicon substrate and cannot relax in the plane of the substrate, we can measure the volume reduction as a reduction in the film thickness of the polymer.<sup>72</sup> Generally, the ellipsometric angles  $\psi(\lambda)$  and  $\Delta(\lambda)$  were measured every 2 minutes, averaging over a 30 second period, for at least 6 hours following the procedure in Baker, *et al.*<sup>72</sup> The physical aging rate,  $\beta$ , was determined from the slope of normalized film thickness vs. logarithmic aging time

$$\beta = -1/h_0 dh/d(\log t) \quad \text{Eq. 3.1}$$

where  $h_0$  is the film thickness at an aging time of  $t = 10$  minutes. A representative physical aging measurement is shown below in Figure 3.2. PS samples were aged at 65 °C, which was previously found to be the temperature at which PS ages fastest.<sup>72</sup> PSF samples were aged at 100 °C, the middle of the plateau in peak aging rate.<sup>7</sup> Due to this elevated aging temperature, PSF films were aged under a flow of dry nitrogen gas to ensure the samples did not degrade during the aging measurement.

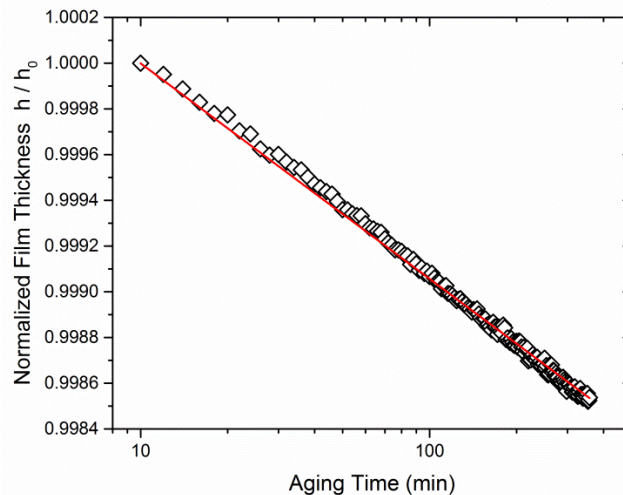


Figure 3.2: Normalized film thickness vs. logarithm of time for a PS film ( $h = 460$  nm) spin coated, annealed, quenched, and aged supported on a silicon wafer. Red line is fit to Eq. 3.1 yielding  $\beta = 9.4 \times 10^{-4}$ .

## 3.4 Results and Discussion

### 3.4.1 Effect of Polymer Chemical Structure: Stiff Backbone vs. Flexible C–C Backbone with Bulky Side-Groups

Here, we will use a common experimental technique to compare the physical aging rate as a function of film thickness of PS and PSF supported on silicon. Figure 3.3 plots the normalized film thickness,  $h/h_0$ , as a function of the logarithm of the aging time for films supported on silicon as measured by ellipsometry. Although not explicitly calculated, the aging rate is essentially the slope of the data plotted in this manner.<sup>72</sup> Polystyrene (Fig. 3.3a) is a common C–C backbone polymer with a large bulky aromatic side-group that limits packing ( $T_g = 100$  °C, fractional free volume FFV = 0.176). Polysulfone (Fig. 3.3b) is a common polymer used in gas separation membranes, whose packing is limited by the stiff aromatic groups along its backbone ( $T_g = 186$  °C, FFV = 0.156). For each polymer, the same aging rate is observed independent of film thickness: for  $570 \pm 50$  nm and  $1400 \pm 100$  nm thick PS films aged at 65 °C for 6 h, and for  $400 \pm 10$  nm and  $1000 \pm 20$  nm thick PSF films aged at 100 °C for 12 h. The aging temperature of 65 °C corresponds to the peak in aging rate for PS measured previously by our group using this ellipsometry technique,<sup>72</sup> while the aging temperature of 100 °C corresponds to the middle of the plateau in peak aging rate exhibited by PSF.<sup>7</sup>

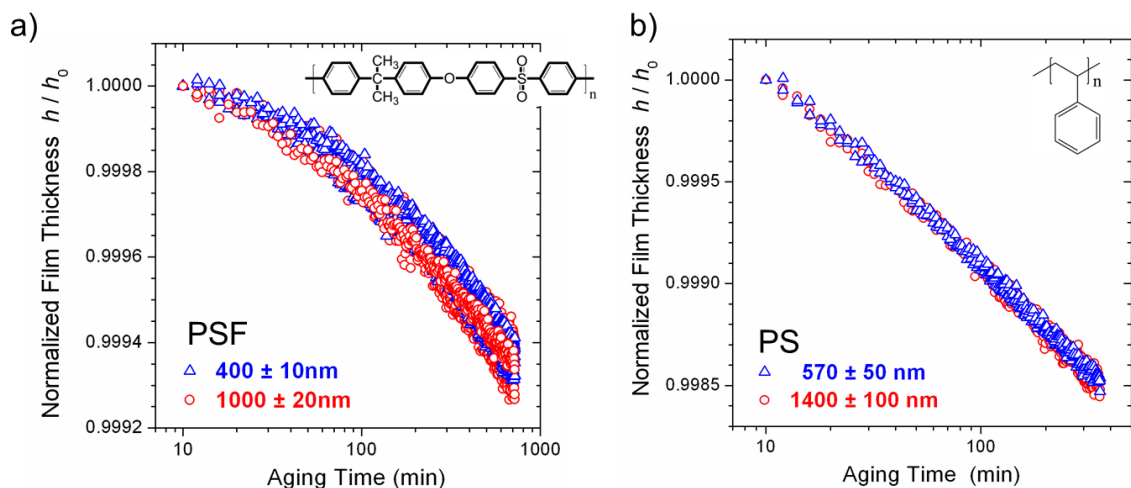


Figure 3.3: Normalized film thickness vs. aging time showing the physical aging of a) PSF films and b) PS films for two different film thicknesses. The physical aging behavior for thinner films (blue) follows the physical aging for thicker films (red). Shown in the inset of each figure are the chemical structures of PSF and PS, respectively.

The limited data presented in Figure 3.3 are used to illustrate the aging behavior of supported films. We have recently published an extensive study on the film thickness and temperature dependence of the physical aging rate  $\beta$  for supported PS films.<sup>66</sup> The aging rate was found to be independent of film thickness for films between 100–2500 nm in thickness. Below  $\sim 100$  nm in film thickness, the aging rate was found to decrease at all aging temperatures in a manner consistent with a reduced  $T_g$  near the free surface penetrating several tens of nanometers in from the boundary.<sup>66</sup> These results were consistent with other aging studies in the literature on supported films of PS,<sup>67,68</sup> poly(methyl methacrylate) (PMMA),<sup>68,69,109</sup> and poly(iso-butyl methacrylate) (PiBMA).<sup>112</sup> As discussed above, the focus of the present study is on the thickness range of hundreds of nanometers to several microns, and not on boundary effects in films less than  $\sim 100$  nm in thickness. The data presented in Fig. 3.3b indicate that PSF films behave in a manner similar to that of PS films showing no thickness dependence of the

aging rate between 400–1000 nm in thickness when quenched and aged in a supported state.

The results presented in Figure 3.3 are significant when compared to those observations from the gas permeation community. Paul and coworkers have extensively characterized the aging characteristics of PSF films.<sup>11,12,71,73,78,79</sup> Using oxygen permeation, Huang and Paul observed faster aging rates with decreasing film thickness (i.e., accelerated aging) for PSF films below  $\sim 4$   $\mu\text{m}$  in thickness measured at an aging temperature of 35 °C.<sup>11</sup> Similar behavior was seen with other polymers, e.g., polyimide and PPO,<sup>11,12,79,84</sup> and in studies by other groups.<sup>74–76</sup> The study that is most relevant to our results presented in Fig. 3.3b is that by Huang and Paul, who observed the accelerated physical aging behavior using ellipsometry for PSF film thicknesses between 375–1000 nm,<sup>79,80</sup> which would appear to contradict our results. However, as we now address, these differences between our results presented in Figure 3.3 and those from the permeation community appear to be due to the details of sample preparation prior to the aging measurements. We note there are also recent measurements by Rowe *et al.*<sup>71</sup> on ultrathin PSF films that have observed decreases in the glassy relaxation time associated with physical aging for film thickness below  $\sim 100$  nm, which were linked to  $T_g$  reductions and boundary effects at these smaller length scales.

For the ellipsometry studies by Huang and Paul<sup>79,80</sup> in which faster physical aging rates were observed with decreasing film thickness for 375–1000 nm thick PSF films, the sample preparation procedure used was chosen to match that of the gas permeation studies as closely as possible.<sup>11,78</sup> Physical aging studies using gas permeation are typically initiated by annealing the films at an elevated temperature above  $T_g$  in a

freestanding state held by a thin wire frame,<sup>78</sup> and then quenching the films to room temperature prior to “masking” them for permeability measurements. The process of masking involves mounting the freestanding films onto anodized grids for support and sealing the perimeter of the films by an aluminum mask to create a well-defined surface area for exposure to the gas permeate.<sup>11</sup> The masking process can take ~20 min while sample mounting, conditioning, and measurement can last ~30 min. Thus, aging studies using gas permeation are typically carried out over many weeks or even months to ensure that the overall aging time is significantly longer than the individual measurement time. For the ellipsometry studies done by Huang and Paul, the PSF films were also annealed above  $T_g$  and then quenched in a freestanding state.<sup>79,80</sup> However instead of masking, the films were instead gently transferred onto silicon wafers for the aging measurements in which ellipsometry was used to determine film thickness and index of refraction of the film every few days over many weeks. In between measurements, the samples were stored at the aging temperature of 35 °C. Physical aging rates determined from these ellipsometry measurements by Huang and Paul were found to be in good agreement with the gas permeation studies showing accelerated aging for thinner films.<sup>79,80</sup>

There are a number of important differences between our PSF aging measurements and those from Huang and Paul. We consider here which factors are important and affect the subsequent stability and mobility of the glassy state. The most significant factor, which we will demonstrate strongly affects the physical aging rate of the film, is the manner in which the films are held during the thermal quench that forms the glassy state. We discount differences in aging time and temperature because similar

aging rates are obtained as a function of temperature for aging times between 6 h and 24 h,<sup>72</sup> and between 24 h and 12 days.<sup>8</sup>

### 3.4.2 *Free-Standing vs. Supported Quench*

By their very nature, thin films must be held in some fashion by an underlying support. Freestanding films are draped across a frame and held only by their edges, while supported films are those resting uniformly on an underlying material. Following the sample preparation procedure described by Huang and Paul,<sup>11,78–80</sup> we compare the physical aging rate of PS films quenched in a freestanding geometry held by a thin square wire frame (as described by McCaig and Paul<sup>77</sup>) vs. films quenched in a supported geometry on a silicon wafer. We chose to focus these studies on PS because of its ease of use in sample preparation, and because it has been more extensively characterized by us<sup>66,72</sup> and in the literature.<sup>8,113</sup>

Figure 3.4 compares the physical aging behavior of PS films that have been thermally quenched under different conditions at the start of the aging measurement. The graphs plot the normalized film thickness,  $h/h_0$ , as a function of the logarithm of the aging time for films aged at 65 °C for 6 h. In Fig. 3.4a, data for a 1260 nm thick PS film is shown, where the circles (upper line with slope corresponding to an aging rate  $\beta = 6.0 \times 10^{-4}$ ) were obtained when the film was quenched in a freestanding state held by a square wire frame and then gently transferred to a silicon wafer for the aging measurement. The triangles (lower line with slope corresponding to an aging rate  $\beta = 9.7 \times 10^{-4}$ ) were obtained when this same film was subsequently re-annealed above  $T_g$  and quenched in a supported state on the silicon. For comparison, data for a 1210 nm thick PS film spin coated directly onto silicon and quenched in a supported state is also shown

(gray diamonds,  $\beta = 9.2 \times 10^{-4}$ ). Similar measurements on multiple samples produced identical results. Physical aging rates for an average of five samples with film thicknesses of  $1380 \pm 100$  nm gave  $\beta = (6.1 \pm 0.6) \times 10^{-4}$  when quenched in a freestanding state and gently transferred onto silicon for aging, in comparison to a much faster aging rate of  $\beta = (9.5 \pm 0.6) \times 10^{-4}$  for the same films reheated and quenched in a supported state. Measurements of additional films all quenched in a supported state, whether spin coated directly onto silicon or floated from mica onto silicon, and measured immediately or after multiple annealing repetitions, all resulted in the much faster aging rate of  $\beta \approx 9.5 \times 10^{-4}$  when they are quenched on silicon in a supported state.

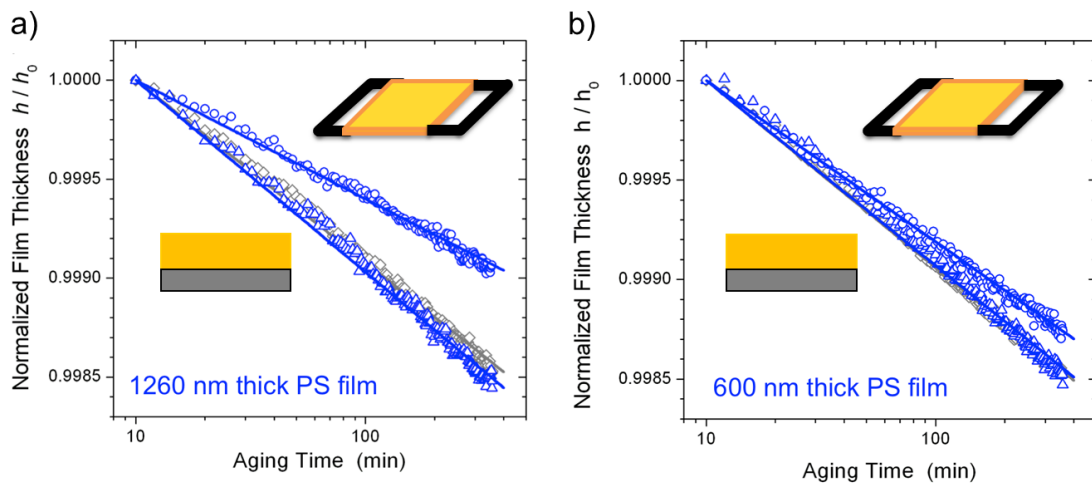


Figure 3.4: Semi-log plot of normalized film thickness  $h/h_0$  as a function of aging time comparing PS films quenched in a freestanding vs. supported state; all films were subsequently aged in a supported state. Blue circles correspond to a) 1260 nm or b) 600 nm thick PS film quenched in a freestanding state held by a wire frame, then gently transferred onto silicon for the aging measurement ( $\beta = 6.0 \times 10^{-4}$  for 1260 nm and  $\beta = 8.1 \times 10^{-4}$  for 600 nm). Blue triangles correspond to this same film subsequently reheated above  $T_g$  and quenched in a supported state prior to a second aging measurement ( $\beta = 9.7 \times 10^{-4}$  for 1260 nm and  $\beta = 9.3 \times 10^{-4}$  for 600 nm). Gray diamonds correspond to PS films spin coated directly onto silicon and therefore also quenched in a supported state ( $\beta = 9.2 \times 10^{-4}$  for 1210 nm and  $\beta = 9.4 \times 10^{-4}$  for 460 nm).

Figure 3.4b shows data corresponding to films thinner by a factor of two. The circles (upper line,  $\beta = 8.1 \times 10^{-4}$ ) were obtained when a 600 nm thick PS film was

quenched in a freestanding state and gently placed onto a silicon wafer, while the triangles (lower line,  $\beta = 9.3 \times 10^{-4}$ ) were obtained when the same film was subsequently re-annealed above  $T_g$  and quenched in a supported state. The (barely visible) gray diamonds ( $\beta = 9.4 \times 10^{-4}$ ) are for a 460 nm thick PS film spin coated directly onto silicon and quenched in a supported state. An average of three samples with film thicknesses of  $570 \pm 50$  nm gave  $\beta = (8.1 \pm 0.6) \times 10^{-4}$  when quenched in a freestanding state and gently transferred onto silicon, relative to an aging rate of  $\beta = (9.3 \pm 0.6) \times 10^{-4}$  for the same films reheated and quenched in a supported state. Clearly, the difference in physical aging rates between films quenched in a freestanding vs. supported state is much less for the thinner ( $\sim 600$  nm thick) films.

The data shown in Fig. 3.4 demonstrate that accelerated aging, *i.e.*, faster physical aging rates for thinner films, is observed when PS films are quenched in a freestanding state, consistent with the measurements from the gas permeation community. However, no film thickness dependence to the aging rate is observed when the films are quenched in a supported state. This is consistent with oxygen permeation measurements of PMMA films by Baker *et al.*, which saw no film thickness dependence to the aging behavior for films quenched in a supported state on mica, then floated, masked, and measured in a freestanding state.<sup>72</sup> Thus, the factor that affects the aging characteristics of the film is the state of the film during the thermal quench and formation of the glassy state. The state of the film in the glassy state during the aging measurement, freestanding vs. supported, does not affect the physical aging rate.

### 3.4.3 *Effect of Annealing Conditions on Physical Aging Rate*

We attribute the differences in Figure 3.4 between the aging characteristics of films annealed and quenched in a free-standing or supported state to the thermal quenching process, and not to the annealing step, for reasons we now discuss. The adequate removal of residual solvent or relaxation of stresses from the spin-coating process has long been a concern in studies of ultrathin polymer films.<sup>59,60,114–117</sup> It is known that changes in  $T_g$  associated with nanoconfinement effects in films less than  $\sim 100$  nm in thickness can be strongly suppressed by the presence of only a few wt% of intended (or unintended) solvent or other small molecule acting as a plasticizer.<sup>118–120</sup> The difference in physical aging rates observed between the free-standing and supported films cannot be attributed to the presence of residual solvent because all our films have been annealed for at least 12 h under vacuum at 120 °C, conditions which have been previously demonstrated to remove trace levels of solvent even for films as thick as 2500 nm.<sup>72</sup> It is also understood that spin coating leads to extended chain conformations both globally and locally, with generally larger effects seen for larger spin speeds.<sup>117,121,122</sup> Previous studies have found distortions in global chain conformations to be unimportant to the  $T_g$  and physical aging behavior of ultrathin polymer films as these are local properties that are independent of chain length and molecular weight.<sup>100,122–125</sup> This is in contrast to properties such as dewetting<sup>126,127</sup> that depend on motion of the entire chain. Studies have found that local chain conformations can be easily relaxed by annealing films for  $\sim 20$  min at  $T_{g\text{bulk}} + 20$  °C, resulting in samples with consistent  $T_g$  and physical aging values.<sup>122,123,127</sup> These are equivalent to the conditions originally proclaimed by

Struik to be sufficient to erase prior thermal history and physical aging of the material, giving reproducible aging results.<sup>7</sup>

Regardless, we have varied the temperature and time of the annealing step above  $T_g$  prior to the aging measurements for both supported and free-standing films to further test and address these concerns. For supported PS films, we have annealed 1200 nm thick films for 25 min as low as 110 °C,  $\beta = (9.2 \pm 0.6) \times 10^{-4}$ , or as high as 170 °C,  $\beta = (9.3 \pm 0.6) \times 10^{-4}$ , and obtained physical aging rates within experimental error of the films annealed for 20 min at 120 °C,  $\beta = (9.7 \pm 0.6) \times 10^{-4}$ . For free-standing PS films, our ability to vary the annealing conditions was much more limited because hole formation was prone to occur for long annealing times and higher temperatures. No difference in aging rate was observed for free-standing films of the same thickness held on wire frames that were annealed above  $T_g$  between 120 °C and 125 °C for 15–30 min. For the free-standing films, we also investigated the influence of spin speed on the annealing step as free-standing films were found to thicken substantially overtime when held above  $T_g$ . PS films were spin coated onto mica between 500 and 3000 rpm, using different solution concentrations, to achieve the same film thickness of  $730 \pm 40$  nm. After annealing the films on mica at 120 °C for at least 12 h to remove residual solvent, they were floated onto wire frames and dried. The films were then further annealed at 120 °C for 20 min in a free-standing state, where they thickened to a final film thickness of  $1200 \pm 100$  nm. Supported films, pinned to an underlying substrate, do not thicken when annealed above  $T_g$ . No clear relationship was found between spin speed and amount of film thickening that occurred in the free-standing films. For films spin coated between 500 and 3000 rpm, we obtained similar aging rates, within experimental error, for films of equivalent

thickness. In summary, we observe no difference in aging rate for films of a given thickness that are annealed under different conditions, as long as they are all quenched in the same geometry to the same quench temperature,  $T_q$ .

#### 3.4.4 *Effect of Quench Rate on Physical Aging Rate*

From the above discussion, we conclude that the difference in aging rates between freestanding and supported films must result from the manner in which the films are held during the thermal quench. We consider now if differences in heat transfer could account for the observed effects. It is well known, but little characterized, that cooling (quench) rate can strongly affect the glassy state formed.<sup>3,8,9,47,54,56</sup> At faster cooling rates, the material becomes kinetically trapped at higher temperatures forming a less stable glass. Thus, glasses formed at faster cooling rates would be expected to have faster physical aging rates, representative of the faster structural relaxation that is occurring in the material. At slower cooling rates, the more stable glasses would be expected to exhibit slower physical aging rates, with the theoretical limiting case of an equilibrium glass formed at an infinitely slow cooling rate.<sup>9,32,47</sup> In order to quantify this effect, we have characterized the physical aging rates of  $1400 \pm 45$  nm thick supported PS films quenched through  $T_g$  at different rates.

Different cooling rates were obtained by changing the material and thickness of a base plate to which the silicon wafer and PS film were clamped. The entire base with the sample attached was placed in the oven at the annealing temperature of  $135$  °C to equilibrate the film. The temperature quench then occurred by removing the base and sample from the oven, and immediately placing the base in thermal contact with a large aluminum block equilibrated to  $30$  °C using a hot plate, as depicted in Figure 3.5a. Base

plates were made of 1/16" thick copper, 1/4" ceramic, or 1/4" ceramic with a 0.02" Teflon bottom layer. The quench rate PS films supported on silicon experienced on each base was determined experimentally by attaching a thermocouple to the top of a bare silicon substrate. The silicon substrate was clipped to the base by a small brass clamp to ensure good thermal contact with the base. The temperature of the sample during the thermal quench was recorded every 1.0 s with the cooling rate through  $T_g$  (100 °C) defined as the slope of the recorded temperature vs. time curve between 115 and 85 °C. A representative temperature profile vs. time is shown for a silicon wafer on a copper base in Figure 3.5b.

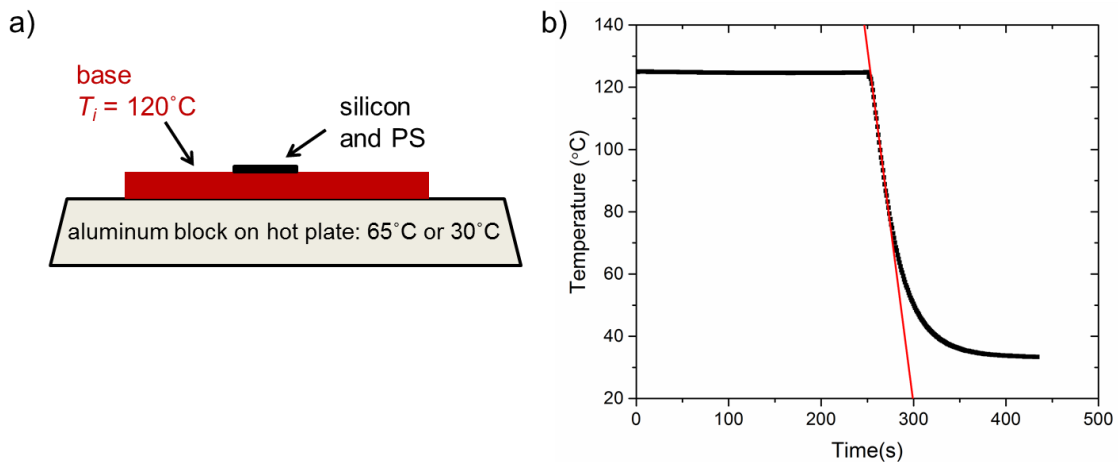


Figure 3.5: a) Schematic of how supported PS films are cooled after removal from vacuum oven. The thermal conductivity of the base and the quench temperature determine the cooling rate. b) Example temperature profile of the top of a silicon wafer atop the copper base cooled to 30 °C.

Table 3.1 details the cooling rates calculated for each of the three bases cooled to the two different quench temperatures. All quench rates are averaged over five measurements of cooling rate. For a quench temperature of 30 °C, we obtained cooling rates of  $135 \pm 13$  °C/min for silicon on the copper base,  $75 \pm 10$  °C/min for the ceramic base, and  $30 \pm 0.8$  °C/min for the ceramic and Teflon base. For a quench temperature of 65 °C, we obtained cooling rates of  $75 \pm 2.5$  °C/min for the copper base and  $55 \pm 1.4$

$^{\circ}\text{C}/\text{min}$  for the ceramic base. To explore the effects of cooling rate on physical aging rate, we annealed PS films supported on each of the three bases and cooled them through  $T_g$  to  $30^{\circ}\text{C}$ . Additionally, we annealed some samples on the temperature controlled ellipsometer hot stage and cooled at  $1^{\circ}\text{C}/\text{min}$ . Supported films quenched in a glass Petri dish (as those shown in Figure 3.4) had a cooling rate of  $50^{\circ}\text{C}/\text{min}$ . These results are shown in Figure 3.6.

Base	Quench to $30^{\circ}\text{C}$	Quench to $65^{\circ}\text{C}$
Copper	$135 \pm 13^{\circ}\text{C}/\text{min}$	$75 \pm 2.5^{\circ}\text{C}/\text{min}$
Ceramic	$75 \pm 10^{\circ}\text{C}/\text{min}$	$55 \pm 1.4^{\circ}\text{C}/\text{min}$
Ceramic and Teflon	$30 \pm 0.8^{\circ}\text{C}/\text{min}$	

Table 3.1: Measured quench rates for PS films supported on silicon cooled on either copper, ceramic, or ceramic and Teflon bases to  $30^{\circ}\text{C}$  and  $65^{\circ}\text{C}$ .

In Figure 3.6, the aging rate is represented by the slope of the data in the semi-log plot of normalized film thickness  $h/h_0$  as a function of aging time. It is clear from the data that faster physical aging rates are observed for films cooled at faster rates as expected. Figure 3.7 plots the measured physical aging rates as a function of cooling rate demonstrating that the aging rate saturates for quench rates in excess of  $\sim 100^{\circ}\text{C}/\text{min}$ . We note that the temperature  $T_q$  to which the films were cooled before being aged at  $65^{\circ}\text{C}$  was varied between  $25$  and  $65^{\circ}\text{C}$ , and found to have no effect on the observed physical aging rate provided that the cooling rate was held constant. For supported films, the rate of heat transfer from the polymer film to the silicon wafer is dictated by the thermal properties of the silicon substrate and underlying base, and is thus independent of polymer film thickness. Ultimately, the cooling rate of the sample is controlled by the large thermal mass of the base. For the supported film data presented in Figures 3.3 and 3.4, the underlying base during the thermal quench was actually a glass Petri dish resulting in a reproducible quench rate of  $50^{\circ}\text{C}/\text{min}$  for these samples.

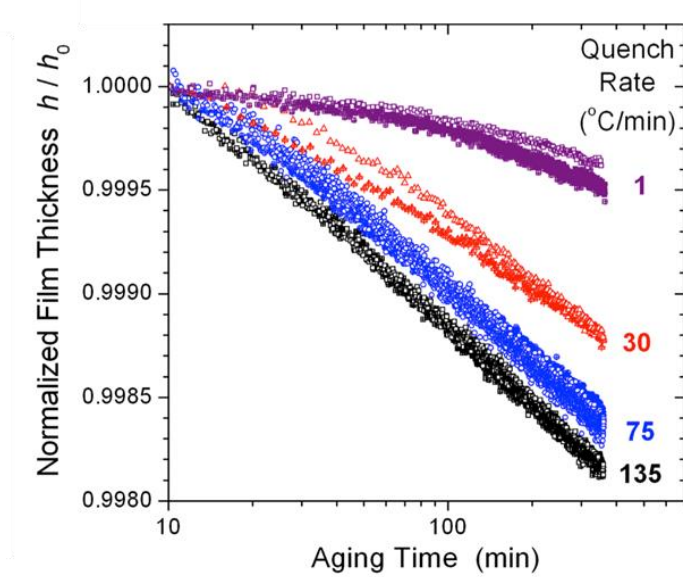


Figure 3.6: Supported PS films,  $1400 \pm 45$  nm thick, aged at  $65$  °C for 6 h after being quenched through  $T_g$  at different cooling rates: 1, 30, 75 and 135 °C/min.

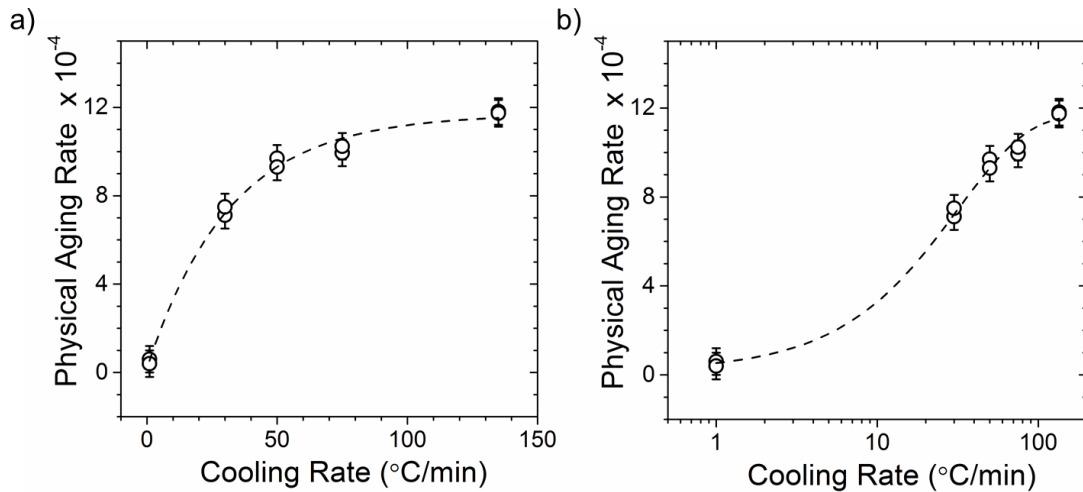


Figure 3.7: a) Physical aging rate of PS supported films cooled at different rates through  $T_g$ . The line is an exponential decay fit to the data. b) Physical aging rate vs logarithm of cooling rate.

Clearly, the quench rate plays a large role in determining the aging rate of thin polymer films. The physical aging rate increases by a factor of  $\sim 10$  as the cooling rate increases by a factor of  $\sim 100$ . However, as the cooling rate becomes faster its influence on the physical aging rate decreases. The temperature  $T_q$  to which films were cooled before aging was varied between 25 and 65 °C and was found to have no effect on the

observed physical aging rate, provided that the cooling rate was held constant. PS films cooled on the ceramic base to 30 °C ( $\beta = (10.6 \pm 0.6) \times 10^{-4}$ ) or cooled on the copper base to 65 °C ( $\beta = (10.1 \pm 0.6) \times 10^{-4}$ ) both had a quench rate of 75 °C/min and resulted in the same physical aging rate within experimental uncertainty.

How do these cooling rates compare to the cooling rates the supported and free-standing films in Figure 3.4 experienced? The supported films discussed earlier and in Figure 3.4 all cooled at 50 °C/min as determined by measuring the cooling rate of a silicon wafer in a glass Petri dish annealed and cooled as described above. For free-standing PS films, we could not measure the cooling rate directly as attaching a thermocouple would break the fragile film as well as change the heat transfer properties of the system. Therefore we used a standard heat transfer model to compute the quench rate for free-standing films.

Free-standing films were quenched by quickly taking them out of a vacuum oven at 120 °C and placing them in room temperature air. Thermal heat transfer through the edges of the film from the free-standing wire frame is very slow and therefore can be neglected. The main source of heat transfer is then convection from the air to the film. Although polymer films are poor thermal conductors, we can approximate the film with the lumped capacitance model, which assumes that the temperature across the entire thickness of the film is constant. The lumped capacitance model can be used when the Biot number,  $Bi = h_{\text{conv}} L/k$  is less than 0.1, where  $h_{\text{conv}}$  is the average convective heat transfer coefficient,  $L$  is half the film thickness, and  $k$  is the thermal conductivity of PS. The thermal conductivity of PS at 100 °C is  $k = 0.128 \text{ W/(mK)}$ .<sup>54</sup> The average convective heat transfer coefficient depends on the flow of air next to the film and will

also depend on the sample size and orientation.<sup>128</sup> In order to estimate a value for  $h_{conv}$ , we measured the cooling rate of a 0.33 mm thick copper plate the same size and in the same orientation as our sample. From this we obtained a value of  $h_{conv} = 10 \text{ W}/(\text{m}^2 \text{ K})$ , in good agreement with expected values for convection of air in a room, typically between 2 and  $25 \text{ W}/(\text{m}^2 \text{ K})$ .<sup>128</sup> These values result in PS having a Biot number of  $< 0.1$  as long as the film thickness is less than 100  $\mu\text{m}$ . The thickest film used in this study was  $\sim 1600 \text{ nm}$  thick, resulting in  $Bi < 0.0001$ .

Using the lumped capacitance model, we can determine the temperature of the film at any time,  $T_{film}(t)$ . The temperature is determined by equating the rate of heat flux out of the film,  $-h_{conv} A_{surf} (T_{film} - T_{\infty})$ , to the rate of heat loss in the film,  $\rho(A_{surf} L)c_p dT_{film}/dt$ , satisfying an energy balance on the film.  $A_{surf}$  refers to the surface area of the free-standing film on both sides, such that  $A_{surf}L$  is equal to the volume as  $L$  is half the film thickness. The values for density of PS ( $\rho = 1020 \text{ kg}/\text{m}^3$ ) and specific heat capacity at constant pressure ( $c_p = 1838 \text{ J}/(\text{kg K})$ ) were found in handbooks.<sup>54</sup> Integrating the energy balance gives

$$\frac{T_{film}(t) - T_{\infty}}{T_o - T_{\infty}} = \exp\left[-\frac{h_{conv}}{\rho L c_p} t\right]$$

where  $T_o$  is the initial annealing temperature and  $T_{\infty}$  is the temperature of the film at long times, the same as the temperature of the surrounding air.

Using the above equation, we can calculate the time to reach a desired temperature and extract a cooling rate for a given film thickness. If we now consider the 1260 nm PS films from Figure 3.4a the cooling rate is of the order of  $500 \text{ }^{\circ}\text{C}/\text{s}$ , i.e.  $\sim 30000 \text{ }^{\circ}\text{C}/\text{min}$ . The cooling rates for free-standing films are therefore much faster than for supported films, yet films quenched free-standing have *lower* physical aging rates

than those quenched in a supported state. Specifically, the 1260 nm film quenched free-standing in Figure 3.4a had a physical aging rate of  $6.0 \times 10^{-4}$  when cooled at  $\sim 30000$  °C/min whereas the same film quenched in a supported state had a physical aging rate of  $9.7 \times 10^{-4}$  when cooled at 50 °C/min. For the thinner films in Figure 3.4b, the 600 nm film will experience a cooling rate that is approximately double that of the 1260 nm film, while the supported film's cooling rate remains unchanged. In Figures 3.6 and 3.7 we showed that increased cooling rate results in an increased physical aging rate. Therefore, if cooling rate was responsible for the difference in aging behavior for films quenched free-standing vs. supported, the free-standing films should always have a slightly *higher* physical aging rate than the supported films quenched at 50 °C/min. Even though there is a film thickness dependence to the cooling rate of free-standing films, with thinner films experiencing faster cooling rates, this cannot be the cause of the accelerated aging rates observed for thinner films quenched in the free-standing state. Even a 100  $\mu\text{m}$  thick free-standing film will have a cooling rate of  $\sim 400$  °C/min, well above the cooling rates of the supported films which exhibit faster physical aging, contrary to the trend shown in Figure 3.7.

#### 3.4.5 *Applied Stress during Quench due to Thermal Expansion Mismatch*

The final factor we consider here is the effect on the physical aging rate resulting from unintended stresses imparted to the film during the quench by the thermal expansion mismatch between the polymer film and the support. It is well known that thermal expansion mismatch between film and support can lead to stress build-up below  $T_g$ .<sup>56,58-60,114</sup> During a thermal cool, the PS film will try to thermally contract more than the underlying silicon because of its larger thermal expansion coefficient;  $\alpha_{\text{PS}}$  is

approximately two orders of magnitude greater than  $\alpha_{Si}$ . The strain of the  $\sim 1 \mu\text{m}$  thick PS film is constrained to match the thermal expansion of the  $500 \mu\text{m}$  thick silicon substrate:<sup>53</sup>

$$\frac{1 - \nu_{PS}}{E_{PS}} \sigma_{PS} + \alpha_{PS} \Delta T = \alpha_{Si} \Delta T.$$

This results in a biaxial tension on the PS film given by

$$\sigma_{PS} = \frac{E_{PS}}{1 - \nu_{PS}} (\alpha_{PS} - \alpha_{Si}) \Delta T \quad \text{Eq. 3.2}$$

for the condition of plane-stress (no stress normal to the film plane,  $\sigma_z = 0$ , as the film is unconstrained in this direction).<sup>53</sup> In the literature, it is common to treat  $\alpha_{Si} \approx 0$  such that this term is frequently omitted.<sup>56,114</sup> In addition, it should be explicitly recognized that the elastic modulus  $E_{PS}$  and Poisson's ratio  $\nu_{PS}$  of PS, as well as  $\alpha_{PS}$ , all depend on temperature<sup>56</sup> quite significantly through  $T_g$ , implying that the temperature change  $\Delta T$  in Eq. 3.2 should be formally treated as an integral.<sup>58</sup>

The relevant temperature range to consider in Eq. 3.2 would normally be from the initial annealing temperature  $T_0$  to the temperature the sample is quenched  $T_q$ :  $\Delta T = T_0 - T_q$ . However, Zhao *et al.* demonstrated that no stress builds up in the film above  $T_g$ , i.e., as long as the film is an equilibrium liquid.<sup>58</sup> This is consistent with our experimental observations, described above, in which varying the annealing temperature  $T_0$  did not affect the measured physical aging rate. Consequently, the upper end of the temperature range in Eq. 3.2 should be replaced by a temperature close to  $T_g$ . We note that for a faster cooling rate the PS film will fall out of equilibrium sooner such that stress may start to build up in the film a few degrees earlier. The shift in  $T_g$  with cooling rate is only 3–4 °C per decade of cooling rate.<sup>54</sup> Because the film modulus  $E_{PS}$  is several orders of magnitude smaller near  $T_g$  than at lower temperatures in the glassy state,<sup>56</sup> the precise

value of the upper temperature considered in Eq. 3.2 does not substantially affect the predicted stress. The lower end of the temperature range in Eq. 3.2 can also be replaced because any stress built up in the film when cooled for a short period of time to a temperature  $T_q$  below the aging temperature,  $T_{\text{aging}}$ , will be relieved when the sample is returned to  $T_{\text{aging}}$ . This reasoning is consistent with our experimental observations that varying  $T_q$ , while keeping the cooling rate constant, did not affect the measured aging rate of the film. Thus, in Eq. 3.2, the relevant temperature range to consider is  $\Delta T = T_g - T_{\text{aging}}$ .

Based on Eq. 3.2 for a temperature range  $\Delta T = T_g - T_{\text{aging}}$ , we calculate that the tensile stress imparted to a PS film supported on silicon during the thermal quench is approximately 12 MPa. This is in good agreement with the 15 MPa residual thermal stress measured by Chung *et al.*<sup>59</sup> for a PS film cooled while supported on mica. Although still below the yield stress of PS, this strong tensile stress could be expected to affect the subsequent physical aging rate of the film. We note that there is no film thickness dependence to this residual thermal stress for supported films, which is consistent with our experimental observations that the physical aging rate of PS films cooled in a supported state is independent of film thickness for films greater than 100 nm.<sup>66</sup>

For free-standing films held by the wire frame, the PS films are only attached on two sides, draped across the narrower width of the rectangular frame. Although it is not possible to directly calculate the stress imparted to the free-standing films by the wire frame during cooling, we can rationalize the frame's impact on the film as follows. The thin wire frame made of 0.009" diam. spring steel flexes slightly as the film becomes taut

above  $T_g$ , an observation described by Huang and Paul.<sup>78</sup> As such, the wire frame effectively acts as a small spring pulling on the two ends of the film with some force  $F = k x$  that will depend on the displacement  $x$  of the frame and some effective spring constant  $k$ . Unfortunately, the displacement is too small for us to characterize experimentally. The stress (uniaxial tension) applied to the film by the wire frame will be given by  $\sigma = F/A = F/(h w)$ , where the cross sectional area  $A$  of the film is equal to the film thickness  $h$  times the film width  $w$ . Thus, we expect the stress imparted to free-standing films by the wire frame to depend on film thickness, and get larger with decreasing thickness.

Many studies have investigated how mechanical stress and deformation enhance mobility of glassy systems. This is an active field of research with some commonalities found between polymer glasses, colloidal glasses, and jammed granular systems.<sup>105</sup> One of the big outstanding questions in this field is to what extent can mechanical deformations or stress act to “rejuvenate” a glass (make it appear younger), vs. “overage” a glass (speed up the aging process).<sup>33,40,47</sup> In virtually all these studies, the initial glass is formed stress free, and then the mobility or aging behavior is investigated by subjecting the glass to various types of stresses. Very few studies, by comparison, have looked at how stress present during the formation of the glassy state affects the subsequent mobility, or physical aging, of the glass. The closest study for comparison with our free-standing films is by Shelby and Wilkes on uniaxially hot drawn PS and polycarbonate samples.<sup>129,130</sup> In their study, PS was elongated above  $T_g$  and cooled under tension; the physical aging rate was then measured in a stress free state using dilatometry. The aging rate of the stressed samples was found to increase by 50% with increasing tension.<sup>129</sup>

The effect also appeared to saturate, with further stress not increasing the aging rate beyond a certain point.

We now return to the results presented in Figure 3.4 and compare our physical aging rates observed for films quenched in free-standing vs. supported states. The 1260 nm thick PS film quenched in a free-standing state would be expected to experience the least amount of stress. Its aging rate of  $\beta = 6.0 \times 10^{-4}$  is quite close to that of (stress free) bulk PS as measured by dilatometry,  $\beta = (6.8 \pm 0.3) \times 10^{-4}$ , for an aging period of  $\sim 1$  day at  $65^\circ\text{C}$ .<sup>8</sup> On average  $1380 \pm 100$  nm thick films quenched in a free-standing state gave aging rates of  $\beta = (6.1 \pm 0.6) \times 10^{-4}$ , and we have previously demonstrated by Baker, *et al.*<sup>72</sup> that this ellipsometry method of measuring physical aging should be comparable to volume dilatometry. The 600 nm thick PS film quenched in a free-standing state on the wire frame is expected to be subjected to a stress that is approximately twice as large as that for 1260 nm thick films because the cross-sectional area of the film has been reduced by a factor of two. Its aging rate of  $\beta = 8.1 \times 10^{-4}$  is significantly higher and quite close to that of supported films known to experience a large (thickness independent) stress during cooling due to the thermal expansion mismatch with the substrate. On average  $570 \pm 50$  nm thick films quenched in a free-standing state gave aging rates of  $\beta = (8.1 \pm 0.6) \times 10^{-4}$ , quite close to the aging rates of supported films,  $\beta = (9.4 \pm 0.6) \times 10^{-4}$ , which are independent of film thickness. From our thickest free-standing quenched films, which we believe experience a sufficiently low stress to be comparable to stress free bulk PS, to supported films, which experience the largest stress, we observe an  $\sim 50\%$  increase in physical aging rate, in good agreement with the results by Shelby and Wilkes<sup>129</sup> on uniaxially hot drawn PS.

This analysis strongly suggests that the cause of the accelerated (faster) physical aging observed for thinner films quenched on free-standing wire frames is due to an increased stress experienced by the thinner films due to the spring-like nature of the wire frame and arising from a decrease in the cross-sectional area of the film. To try to verify this conclusion, we have fabricated rigid frames for free-standing films that do not flex in response to the tension of the film by punching rectangular or circular openings nylon and stainless steel frames. For this type of frame, the applied stress due to the PS film during the thermal quench can be calculated following the same procedure used to determine the stress applied to the supported films. For a free-standing film draped across the rectangular opening of a rigid frame with the film only held on two sides, the uniaxial tension applied to the PS film due to the thermal expansion mismatch between the film and the frame is given by:<sup>53</sup>

$$\sigma_{PS} = E_{PS} (\alpha_{PS} - \alpha_{frame}) \Delta T.$$

For a circular opening of a rigid frame, with the film spanning the entire opening, the biaxial tension applied to the PS film is actually equivalent to that experienced by the supported films, and is given by:<sup>53</sup>

$$\sigma_{PS} = \frac{E_{PS}}{1 - \nu_{PS}} (\alpha_{PS} - \alpha_{frame}) \Delta T.$$

Note that in contrast to the wire frames, the stress experienced by the PS films during cooling on either geometry of the rigid frames, due to thermal expansion mismatch between film and support, is predicted to be independent of film thickness.

We tested an extensive number of free-standing films quenched on rigid nylon or stainless steel frames with both rectangular and circular openings, but were not able to obtain reproducible aging rates for nominally identical samples. As shown in Figure 3.8,

free-standing films supported on rigid frames wrinkled extensively, much more than the films on wire frames.

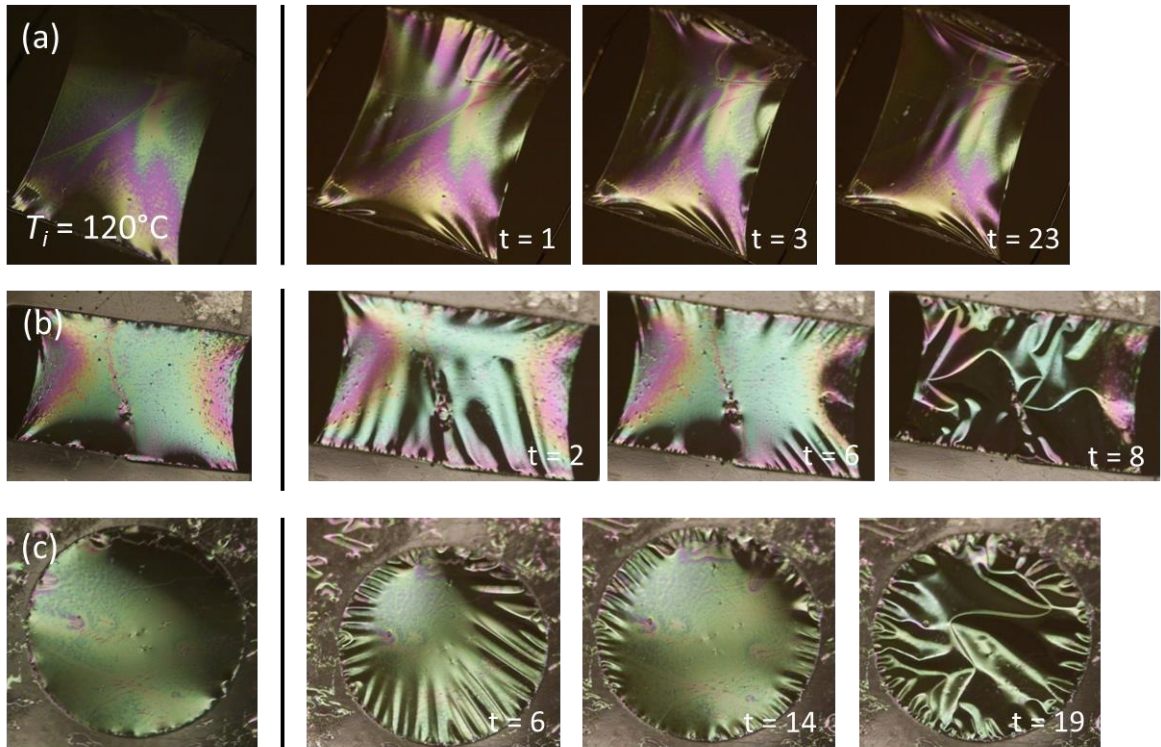


Figure 3.8. Photographs of free-standing films being cooled through  $T_g$  held on a a) wire frame, b) rigid nylon frame with rectangular hole, or c) rigid nylon frame with circular hole. Time after cooling for each frame is given in seconds.

Although the free-standing films quench through  $T_g$  in a fraction of a second as they were exposed to room temperature air, the rigid frames cool much slower due to their larger thermal mass. Thus, the film cools through  $T_g$  and becomes solid before the frame thermally contracts. As the frame thermally contracts, the glassy polymer film wrinkled and buckled extensively. However, the free-standing films held on the wire frames experienced a small tension keeping the films reasonably taut during cooling. Wrinkling persisted on the rigid frames even when the samples were cooled slower, at a controlled rate of  $10\text{ }^\circ\text{C}/\text{min}$ , using a specially designed chamber to cool the air surrounding the film and frame at this controlled rate. We believe the wrinkling and

buckling that the free-standing films on the rigid frames experience lead to random stresses in the film that vary significantly from sample to sample, and is likely responsible for the wide range of aging rates observed. The next chapter will focus on investigating the physical aging of glassy polymer films formed under different controlled stress conditions.

### **3.5 Summary and Conclusions**

We have performed a systematic assessment of factors affecting the physical aging rate of micron thick polymer films and demonstrate that physical aging is dictated by conditions during the formation of the glassy state. Using ellipsometry to characterize the time-dependent decrease in film thickness that results from the increase in average film density during aging, we determined the physical aging rate of polymer films thermally quenched under different conditions. Although all films are subsequently aged in a supported state, we observed significant differences between films quenched in a free-standing compared to supported state. Films quenched in a free-standing state exhibit a strong thickness dependence to their physical aging rate at micron length scales, an order of magnitude or two larger than thicknesses where nano-confinement effects of the glass transition and modulus are typically observed. In contrast, supported films do not display any film thickness dependence to their aging rate at this large length scale. This phenomenon is not affected by differences in molecular structure, annealing temperature and time above  $T_g$ , or quench depth below  $T_g$ . Instead, we argue that different sample geometries inadvertently impose small differences in stress during vitrification that can trap the glassy films into different states (potential energy minima), strongly affecting the subsequent physical aging rate of the films.

# Chapter 4

## Formation of Polymer Glasses under Stress: Effect on Physical Aging

A version of this chapter was published as Laura A. G. Gray, Connie B. Roth *Soft Matter*, 10, 1572 – 1578, 2014.

“Copyright 2014 by the Royal Society of Chemistry”

### 4.1 Synopsis

In this chapter I will discuss our efforts to directly apply stress to a polymer above the glass transition temperature and during the vitrification process. These experiments allowed us to test our hypothesis that stress imparted to polymers during cooling is an important factor determining the subsequent physical aging of the glass. Broadly speaking, how stress or strain imparts mobility to glassy or jammed systems is of interest across colloids, granular materials, polymers, and molecular glasses. Here, we probe for the first time how deformation imparted to a glass while it is forming affects the subsequent glassy state, even after the stress has been removed. Conveniently, entangled polymers provide an ideal system for applying stress above the glass transition as the entanglements allow the polymer film to maintain mechanical integrity for some time above  $T_g$ . As stress applied during the quench is increased, the physical aging rate remains constant until quickly transitioning to a much higher aging rate above a minimum threshold in stress. We propose to explain this unique dependence of physical aging rate on stress using ideas previously suggested that stress or strain can deform the potential energy landscape (PEL) of a glass.

## 4.2 Introduction

Glasses are a non-equilibrium state of matter formed when packing frustration leaves the system trapped in a configuration that does not correspond to the global energy minimum of the equilibrium glass or crystal. Trapped in this higher energy state with excess free volume, glasses evolve in time leading to densification of the material and a host of other property changes, a process termed physical aging. A scientific description of these dynamics is extremely challenging because of the many-body interactions involved and our lack of a statistical mechanics description of non-equilibrium phenomena. In recent years, numerous studies have observed anomalous glassy physical aging dynamics as the sample size is reduced,<sup>106</sup> some occurring at length scales much larger than where boundary effects are known to alter the glass transition.<sup>66,102</sup> It has been suggested that unintended stresses imparted to the material during glass formation might be the underlying cause of the observed faster physical aging.<sup>55,61</sup> Here we directly test this assertion and demonstrate that stress present during the thermal quench is an important parameter affecting the subsequent physical aging.

Glassy behavior is common to a variety of different systems that all exhibit frustration upon cooling or densification, leading to the kinetic arrest of the system. Molecular glass formers, as common as silica (window glass) and amorphous polymers (transparent plastics), form a glass upon cooling when the available thermal energy is no longer able to equilibrate molecular configurations at the glass transition temperature ( $T_g$ ). Colloidal systems (milk) and granular materials (sand) become jammed into a glassy state at high volume fractions, while spin glasses occur when the magnetization becomes frustrated. The glass transition defies theoretical description because of its

pseudo nature, depending on the rate at which the glassy state is formed and there being little structural difference between the liquid and glassy state. Significant progress has been made in our understanding of the glass transition by comparing similarities across different systems. One such unifying concept is the jamming phase diagram,<sup>6,13</sup> which proposes a possible equivalence between temperature, density, and stress as different control parameters for the onset of rigidity associated with glass formation (Figure 4.1). Although the specific shape of the jamming diagram and the extent to which jamming (a zero-temperature phenomenon) and the glass transition can be related are under debate,<sup>6,20,24,25</sup> for the present discussion we are intrigued simply by the possible interplay between temperature and stress as we investigate glass formation by temperature quench at non-zero stress. A related issue of current debate is the extent to which mechanical deformation (stress) can be used to increase mobility and possibly “rejuvenate” a glass, equivalent to re-equilibrating the glass above its  $T_g$ .<sup>28,47,105</sup>

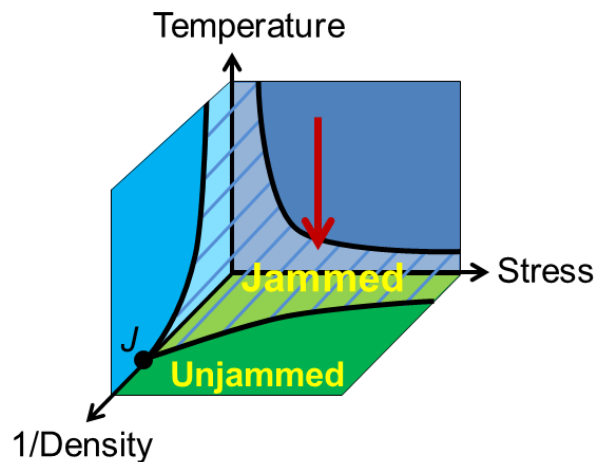


Figure 4.1: Jamming phase diagram,<sup>14</sup> originally proposed by Liu and Nagel,<sup>6,13</sup> illustrating the proposed control parameters which define whether a system is jammed or unjammed. Decreasing temperature, stress, or increasing density can move the system from a liquid-like to a jammed or glassy solid-like state. The red arrow indicates that the following experiments will access the glassy state by cooling at a non-zero stress.

Recent studies have shown that molecular mobility of glasses does not correlate with free volume,<sup>30,48</sup> but instead depends on the material's position within a potential energy landscape.<sup>43,49</sup> The potential energy landscape (PEL) picture is an important conceptual framework for understanding the glass transition and dynamics in frustrated systems, providing a topographical view of the energy states of the system that depend on the configurational coordinates of the structural units.<sup>2,3</sup> The rugged multidimensional landscape describing amorphous materials has many local energy minima within which the system can become easily trapped, preventing it from finding the more energetically favorable global minimum. The various energy minima are arranged into "metabasins" within which local  $\beta$ -relaxations associated with physical aging drive the system towards a common local minimum or "basin of attraction".<sup>27</sup> At higher temperatures above  $T_g$ , the system is free to transition between metabasins via  $\alpha$ -relaxations. The classic cooling rate dependence of glass formation where faster cooling rates lead to less stable glasses with faster physical aging rates is understood as the system being trapped in shallower, higher energy metabasins.<sup>3,26</sup> In contrast, a slower cooling rate allows the system more time to explore the rugged PEL enabling it to reach a deeper, lower energy metabasin with a correspondingly slower physical aging rate.

Within the PEL framework, stress induced molecular mobility has been centered around the idea originally put forward by Eyring<sup>44</sup> of a stress activated barrier hopping or landscape tilting mechanism.<sup>35-41,43,45</sup> A stress or strain imparted to the glass acts to deform or tilt the PEL, such that sufficiently large values can drive the system up the PEL<sup>40</sup> appearing to effectively reverse physical aging or "rejuvenate" the glass.<sup>28,47</sup> However, mechanical deformation can also transform the glass to a different energy

state.<sup>40,43,47</sup> Studies of how mechanical deformation imparts mobility that alters glassy dynamics have almost exclusively been conducted on systems where the glass was formed stress free.<sup>28–34,48–50</sup> Here, we investigate how stress applied during vitrification of the glass can increase its physical aging rate appearing to leave the system trapped in a less stable, higher energy state.

### 4.3 Experimental Methods

Molecular mobility of glassy polymer films can be characterized by measuring the physical aging rate. The speed at which the glassy material undergoes densification on a logarithmic timescale, often termed structural relaxation, depends on the nature of the local energy states within which the system is trapped providing a measure of the local slope of the metabasin.<sup>3,27</sup> As discussed previously in Chapter 3.3, we measure physical aging by measuring the logarithmic decrease in film thickness of polymer films pinned to silicon substrates using ellipsometry. The physical aging rate is defined as  $\beta = -\partial(h/h_0)/\partial(\log t)$ .<sup>55,61,66,72</sup> where  $h_0$  is the absolute film thickness at an aging time of 10 minutes. For this particular study, we have used polystyrene (PS) of three different molecular weights ( $M_w = 1440$  kg/mol,  $M_w/M_n = 1.04$ ;  $M_w = 650$  kg/mol,  $M_w/M_n = 1.06$ ;  $M_w = 289$  kg/mol,  $M_w/M_n = 2.19$ ). Films from 150 to 1700 nm in thickness were formed by spin-coating PS from toluene onto freshly cleaved mica, and subsequently annealing under vacuum for at least 12 h at 120 °C ( $T_g + 20$  °C) to remove residual solvent and relax chain conformations. Films were then floated off mica onto the surface of deionized water. The films were then captured on a rigid aluminum frame such that only two sides were held. The films were allowed to dry for at least 30 minutes before use. The initial length of the film was 9.15 mm and the width was 13 mm.

In order to apply a stress to the free-standing films, the aluminum frame was placed in a specially designed jig such that the film was oriented vertically. The aluminum frame was surrounded on three sides by heaters and further enclosed on all sides. The top support of the frame was attached to a cantilever arm and was free to slide up and down on two steel rods. Both the top support of the frame and the cantilever arm could be pinned in place, allowing us to control when and for how long a stress was applied to the film. A variable counterweight on the opposite end of the cantilever arm exerted a constant tension on the film (see Figure 4.2). Varying the counterweight and film thickness allowed us to vary the amount of stress applied to the film. Stress,  $\sigma$ , was calculated by dividing the tension by the cross-sectional area, which is the width multiplied by the film thickness as measured by ellipsometry before the aging measurement and after the stress was removed. The sides of the films did not noticeably bow inwards under the stresses applied, so we can approximate the film width as constant throughout the experiment.

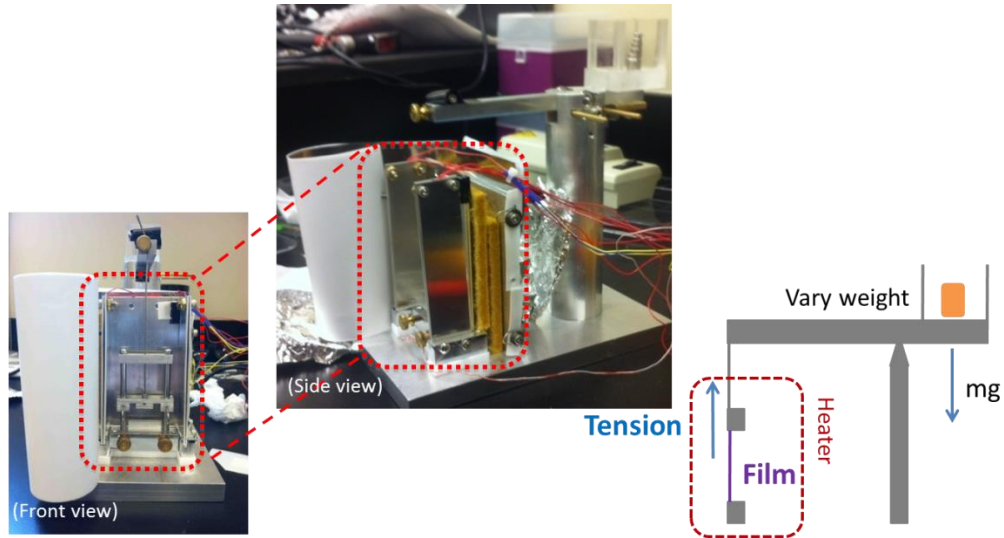


Figure 4.2: Pictures and a schematic of the jig used to apply a constant stress to a polymer film above  $T_g$  and during the quench. The film was held in a special holder and surrounded on three sides by heaters and further enclosed by a stainless steel and Teflon flap. Pins on either side of the fulcrum of the cantilever arm allowed us to control when stress was applied to the film.

Films were annealed in the jig with the frame held fixed for 30 minutes such that they were at  $T_g + 20\text{ }^\circ\text{C}$  ( $\pm 2\text{ }^\circ\text{C}$ ). A constant stress between 1.0 MPa and 15.0 MPa was then applied to the film for two minutes at  $T_g + 20\text{ }^\circ\text{C}$  by releasing the pins holding the cantilever arm in place. The enclosure was then opened and the heaters were turned off in order to allow the film to quickly quench through  $T_g$  while under stress. The films were allowed to cool for two minutes, however based on our previous work, the film cools rapidly through  $T_g$  at a rate greater than 7000 K/min.<sup>61</sup> The stress was then removed, and the top bar of the aluminum frame was lowered to its original position and pinned in place. Films were then gently transferred onto silicon wafers for the aging measurements.

## 4.4 Results and Discussion

Figure 4.3 plots the decrease in normalized film thickness  $h/h_0$  as a function of aging time that results from densification of the films during structural relaxation. Data

shown are for 1440 kg/mol  $M_w$  PS films of thicknesses between 150–700 nm with different amounts of tension applied shortly before and during the thermal quench. The applied stress  $\sigma$  during glass formation was found to strongly affect the resulting physical aging rate of the films. Figure 4.3 demonstrates this by comparing aging curves for films of equivalent thickness and different applied tensions with films of different thickness and the same tension. To within experimental error, the measured physical aging rates were found to fall into two groups with an average aging value of  $(3.52 \pm 0.98) \times 10^{-4}$  at low stress values,  $\sigma \lesssim 8$  MPa, and  $(8.03 \pm 0.21) \times 10^{-4}$  at high stress values,  $\sigma \gtrsim 9.5$  MPa.

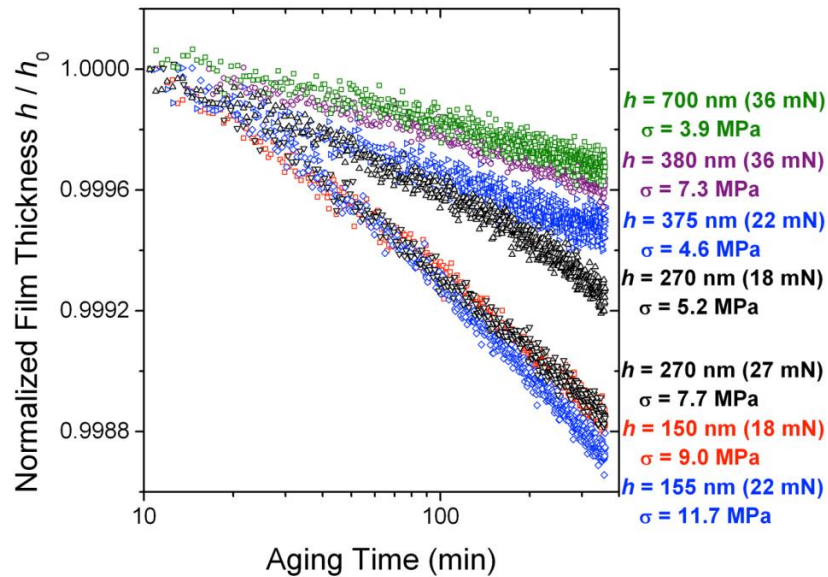


Figure 4.3: Normalized film thickness  $h/h_0$  vs logarithm of aging time for  $M_w = 1440$  kg/mol PS films quenched under stress. The legend notes the film thickness, tension, and resulting stress applied to each film.

Figure 4.4 graphs the measured physical aging rate  $\beta$  as a function of applied stress  $\sigma$  for the 1440 kg/mol  $M_w$  PS films. The data appear to transition from a low aging rate plateau at small stress values to a higher aging rate plateau at larger stress, with the transition occurring over a relatively small range of stress values between 7.6 and 9.0

MPa. The higher aging rates at larger stress values indicate that the resulting polymer glass is less stable. Data for a second high molecular weight and monodisperse PS, 650 kg/mol  $M_w$ , are also included in Figure 4.4 and fall within the range of data for the 1440 kg/mol  $M_w$  PS films. The physical aging at non-zero stress is consistent with expectations for a non-equilibrium glass formed by a standard temperature quench. The plateau in aging rate at small stress values is consistent with recent work by Lee and Ediger<sup>33</sup> that found no change in aging rate for polymer glasses (formed stress free) subjected to small deformations. It is also perhaps intuitive that the aging rate should increase with applied stress. However, we find the qualitative behavior of the data most surprising, as it transitions quite sharply from a low stress aging response to higher aging rates at larger stress and appears to plateau. Whether this plateau would continue for even larger stress values is not clear because further measurements at larger stress are prevented by film failure. The variability in the data is slightly larger at the lower aging rates because the overall decrease in thickness with aging time is smaller. For an aging rate of  $4 \times 10^{-4}$ , the total decrease in film thickness during the 6 h of aging is only 0.04%, which for a 400 nm thick film corresponds to a decrease of 0.16 nm in thickness. Even though this decrease is very small, we have previously demonstrated<sup>61,66,72</sup> that it is within the sensitivity of our ellipsometer, and that this method of determining the physical aging rate from the decrease in film thickness is consistent with other methods using the increase in index of refraction, as well as other experimental techniques such as dilatometry.<sup>72</sup>

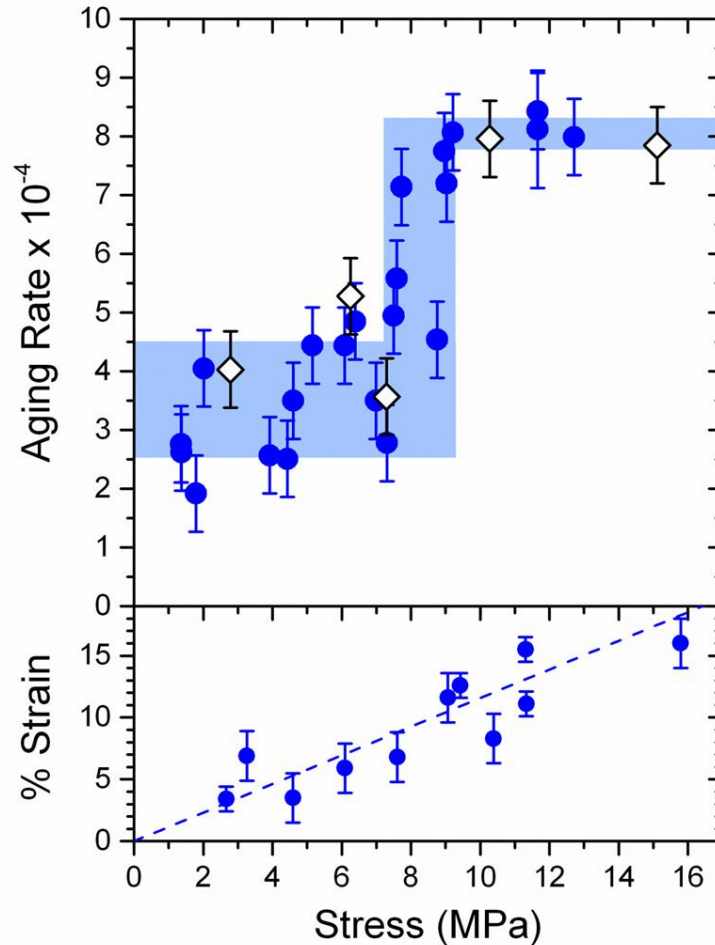


Figure 4.4: (top) Physical aging rate vs. applied stress during the quench for PS films of  $M_w = 1440$  kg/mol (blue circles) and 650 kg/mol (black diamonds). The thickness of the shaded blue bars represent the standard deviation of the physical aging rates below and above the transition stress. (bottom) Total strain vs. stress for  $M_w = 1440$  kg/mol PS films, indicating the deformation is in the linear regime.

Figure 4.4 also plots the measured strain achieved due to the applied stress on the polymer film in its rubbery state above  $T_g$ . The data show a linear trend over the range of applied stresses despite the sharp increase in aging rates observed indicating that the rubbery film behaves as expected for an elastic material, with no unusual change in deformation occurring at the stress where the increase in aging rate is observed. For an elastic rubber, the observed strains (all  $< 20\%$ ) are sufficiently small that no appreciable chain alignment would be anticipated, consistent with our observation that no evidence of

birefringence is measured (differences in index of refraction were  $< |0.003|$ ) even for the largest strains. When stress was applied, the films immediately stretched to their total elongation and did not visibly lengthen with time during the short two minutes stress was applied prior to thermally quenching the films. Such an observation is consistent with a tensile creep compliance deformation into the entanglement plateau region where strain does not depend on time for times less than the reptation time. At a temperature of  $T_g + 20$  °C, the reptation time is 24 min for 650 kg/mol  $M_w$  PS and 6 h for 1440 kg/mol  $M_w$  PS. Thus above  $T_g$ , our films are equivalent to a rubbery, physically cross-linked network. When samples are annealed for longer times comparable to the reptation time, flow occurs and the films lose mechanical integrity.

Interestingly, the effective compliance of the strain-stress data shown in Figure 4.4b,  $1.2 \times 10^{-8} \text{ Pa}^{-1}$ , is smaller by two orders of magnitude than the anticipated bulk plateau compliance of PS,  $4 \times 10^{-6} \text{ Pa}^{-1}$  as shown more fully in Figure 4.5 (bulk compliance estimated using a bulk uniaxial elongational compliance  $D$  from the plateau shear compliance<sup>131</sup> of  $\log J_e = -5.9$  via  $J = 3D$ , valid in the elastic regime). This indicates an increased stiffness of our films in the rubbery regime above  $T_g$ , which appears to be independent of film thickness over the range (150–700 nm) studied. Such stiffening has been previously observed in biaxial compliance measurements on ultrathin PS “nanobubble” films<sup>89–91,132</sup> and in nanoprobe contact measurements on a variety of polymers.<sup>92,96,133,134</sup> Despite considerable efforts, the underlying cause of this stiffening in thin films has yet to be identified, with suggestions that the effect is related to a stress-induced stiffening<sup>133,134</sup> or some change (trapping) of entanglements resulting from confinement of the polymer chains that may suppress some Rouse modes.<sup>99,135</sup> Clearly,

more work is needed to understand this effect.

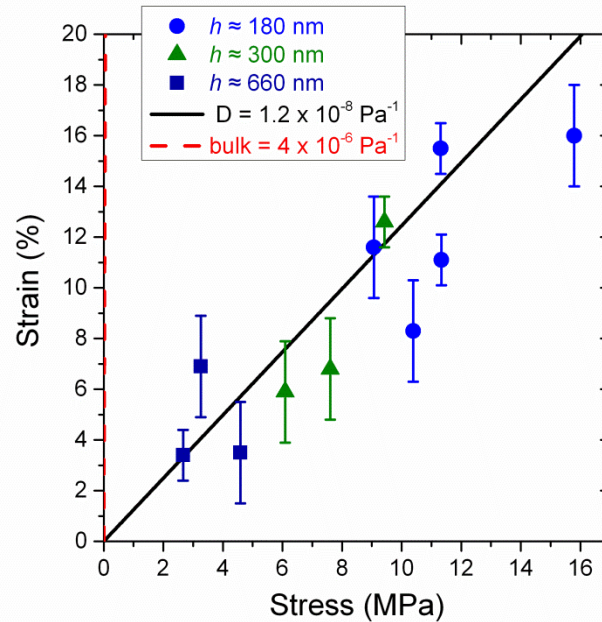


Figure 4.5: Strain response of films stressed above  $T_g$  at 120 °C in the rubbery regime (same data as shown in Figure 4.4). Black solid line is a fit to the data representing the rubbery creep compliance of our samples. Bulk rubbery creep compliance is depicted by the nearly vertical red dashed line.

In an effort to determine how universal this unusual aging behavior is, we collected similar data for a lower and more disperse molecular weight distribution PS, 289 kg/mol  $M_w$  with  $M_w/M_n = 2.19$ , which is more typical of commercial polymers. As shown in Figure 4.6, the observed behavior in physical aging rate as a function of applied stress during glass formation is qualitatively the same. The average aging rate for low stress values,  $(3.53 \pm 0.61) \times 10^{-4}$ , is the same as that for the higher molecular weight samples shown in Figure 4.4, with the data tending to the same aging rate in the limit of zero stress. This is consistent with physical aging measurements of polymer glasses formed at nominally zero stress that do not show a molecular weight dependence as structural relaxation involves motion on a local segmental scale. The aging rate at zero stress is also in good agreement with recent work in our group on PS films subjected to

biaxial stress on cooling imparted by thermal expansion mismatch between the film and supporting frame giving a limiting zero stress aging rate of  $\sim 4 \times 10^{-4}$ .<sup>55</sup>

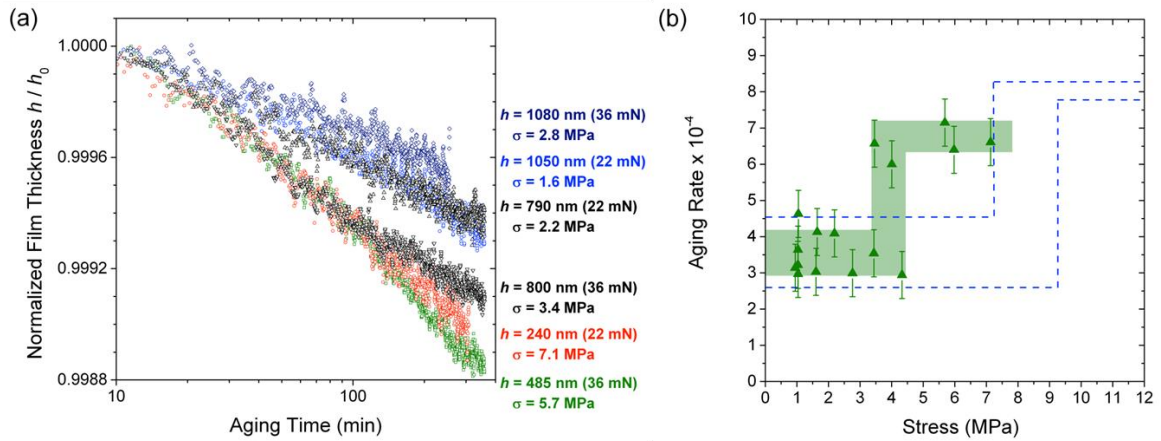


Figure 4.6: a) Normalized film thickness  $h/h_0$  vs logarithm of aging time for  $M_w = 289$  kg/mol PS films quenched under stress. The legend notes the film thickness, tension, and resulting stress applied to each film. b) Physical aging rate vs. applied stress during the quench for PS films of  $M_w = 289$  (green triangles). The thickness of the shaded green bars represent the standard deviation of the physical aging rates below and above the transition stress. The dashed blue lines represent the physical aging behavior of the  $M_w = 1400$  kg/mol and  $650$  kg/mol PS shown in Figure 4.4.

Despite the qualitative similarities between the data in Figures 4.6b and 4.4, there are some important differences. The transition from a low to high aging rate plateau with increasing stress appears sharper and more distinct. In addition, the resulting higher aging rate plateau is slightly reduced with an average aging rate of  $(6.72 \pm 0.39) \times 10^{-4}$ . (Stresses above 7.2 MPa could not be applied to this polymer as mechanical failure of the samples occurred.) Most significantly, the minimum stress needed before an increase in aging rate is observed is noticeably lower at  $\sigma \approx 3$  MPa. These differences may be due to either the reduced molecular weight or the increased dispersity of the 289 kg/mol  $M_w$  PS. The reptation time for this polymer is only 90 s at the temperature ( $T_g + 20$  °C) at which the two minutes of stress is applied; thus, partial relaxation of the material could occur for these samples. To test this assertion, several attempts were made to study a low

molecular weight monodisperse PS ( $M_w = 400$  kg/mol,  $M_w/M_n = 1.06$ ), which were annealed and stressed for times (2-5 min) approaching and comparable to the reptation time (4.6 min). In all instances, these samples lost mechanical integrity during the stressing above  $T_g$ , which is consistent with our assertion and would be expected for polymer melts under stress in the flow regime. Thus, it is likely that the broad dispersity of the low molecular weight 289 kg/mol  $M_w$  PS samples, whose distribution contains some high molecular weight chains, allows for the samples to maintain mechanical integrity for the two minutes stress is applied above  $T_g$ . A significant presence of lower molecular-weight component within this distribution may then limit local stretching for a fraction of the chains. A full study of how the minimum stress and high aging rate plateau vary with molecular weight, dispersity, and annealing time is beyond the scope of the present work. Future studies could test these different factors by using various bimodal distributions of two monodisperse polymers to control the contributions of low and high molecular weight chains. These issues highlight the challenges of such measurements where stress is applied in the liquid state prior to vitrification. Such considerations would also make these types of studies difficult on other (unentangled) glassy systems, although one could imagine designing some experimental setup to apply compressive stresses that would presumably avoid this issue.

We now consider possible reasons for the surprising qualitative shape of the aging rate  $\beta$  versus applied stress  $\sigma$  data presented in Figures 4.4 and 4.6b. As the applied stress increases, the physical aging rate remains unchanged at low stresses, then above some minimum stress value, the aging rate transitions quickly over a small range of stresses to a higher aging rate before appearing to reach some new plateau. Although

much work has investigated how the presence of stress can lead to enhanced mobility in glasses, the vast majority of the available literature on this pertains to glassy systems that were first formed stress free. Here, our experiments investigate for the first time the subsequent stability of glasses which have been formed by a temperature quench at non-zero stress values, as illustrated by the red arrow in Figure 4.1.

Our observation that the aging rate increases with applied stress demonstrates that the resulting glassy state is less stable. Consider a glass formed by cooling quickly, which exhibits a faster aging rate, indicative that it fell out of equilibrium at a higher temperature and formed a less stable glass. Within the PEL framework, the faster aging rates of quickly cooled glasses are seen to represent the more shallow energy basins higher in the PEL,<sup>3,26</sup> while glasses cooled more slowly are able to reach deeper energy metabasins lower in the PEL (Figure 4.7). Thus, from the faster aging rates observed at higher stress values, we can infer that the glassy state formed under large applied stress resides in a higher, less stable part of the PEL. The current theoretical understanding of how stress alters the mobility of glasses is also based on the glass' position within the PEL,<sup>41,49</sup> and not, as one might intuitively guess, on the available free volume because even glasses under compressive deformation show enhanced mobility.<sup>30,48</sup>

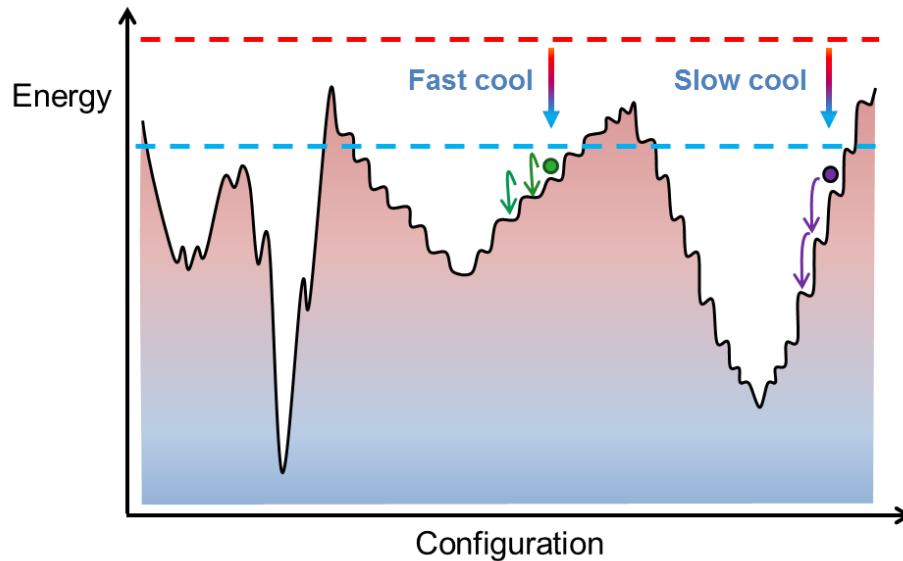


Figure 4.7: Schematic potential energy landscape of a typical glass former. As temperature is lowered, the system is trapped in a local “metabasin” whose energy depends on cooling rate. Faster cooling rates trap the system into shallower, higher energy metabasins with correspondingly faster physical aging rates.

To understand how stress might affect glass formation during a temperature quench, we propose an interpretation of our results based on the available literature investigating the deformation of glasses that have been formed stress free. We suggest that stress imparted to the material during glass formation acts to distort the PEL such that for high enough stress values above some minimum threshold value, the system preferentially cools into a different metabasin upon vitrification. After the stress is removed, the system is left trapped in this different, higher energy metabasin with a correspondingly faster physical aging rate (Figure 4.8). This interpretation is supported by observations that mobility of glasses depends on its position within the PEL,<sup>41,49</sup> and that stress or strain imparted to glasses and jammed systems lead to increased mobility.<sup>28–34,37–43,47–50,105</sup> These observations have been interpreted as a tilting of the PEL<sup>32,33,35–43</sup> acting to drive the system up the landscape,<sup>40</sup> which for sufficient magnitude can leave the system trapped in a higher energy state.<sup>40,41</sup> For example, in the work by Lee and

Ediger,<sup>33</sup> small deformations of polymer glasses leave the physical aging rate unchanged indicating that the glass remains trapped within the same metabasin, while larger postyield deformations that can induce transitions to higher metabasins did appear to “rejuvenate” the glass as if it was thermally reset. This distinction between small and large deformations leading to qualitatively different aging behavior has been made by Lacks and Osborne<sup>40</sup> in their molecular dynamics simulations of sheared glasses where they find the system either “overaging” or “rejuvenating” depending on the size of the imposed strain. Within the PEL framework, small strains are seen as “overaging” the system, driving it towards the same, thermally defined energy minimum, whereas larger strains appear to “rejuvenate” the system by transitioning it to a shallower, strain-dependent energy minimum. The imposed deformation is treated as decreasing energy barriers between metabasins, which, if large enough, can facilitate the transition to a higher energy metabasin.<sup>33,40,41</sup>

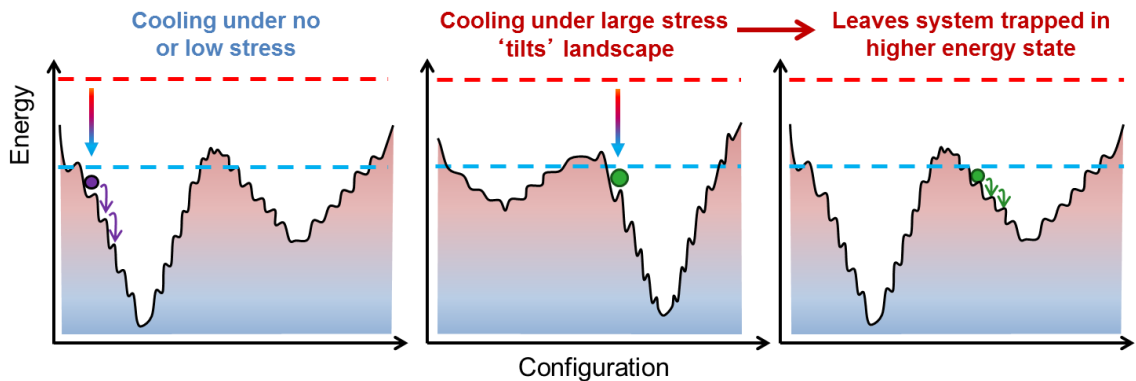


Figure 4.8: Proposed effect of stress during glass formation on local PEL. For large enough stress values, the PEL is sufficiently “tilted” that on cooling the system ends up trapped in a different, higher energy metabasin, exhibiting a correspondingly faster physical aging rate even after the stress is removed.

In recent molecular dynamics simulations on a coarse-grained model of glassy PS, Chung and Lacks mapped the inherent structures of the system within the PEL for a PS glass subjected to shear strains.<sup>43</sup> For small strains, deformation was found to slowly

drive the system up the landscape but remain within the same metabasin, while for larger strains, transitions to different, higher energy metabasins were observed. Similar results are found when stresses are applied.<sup>45</sup> Such simulations are consistent with our interpretation of the experimental results presented here. Our samples subjected to small deformations where the system quenches into the same metabasin would exhibit the same aging rate, while samples subjected to sufficiently large deformations that are enough to force the system to quench into a different, higher energy metabasin would lead to a higher aging rate. Although our data appear to show only a single transition to a higher energy metabasin, this does not preclude further transitions at higher stress, which could not be reached in the present study because of film failure during stretching. Thus, in analogy to these works and other studies that treat mechanical deformation as facilitating energy barrier hopping by effectively ‘tilting’ the PEL,<sup>32,33,35–41,43,45</sup> we view the addition of stress during vitrification as altering the PEL landscape such that for sufficiently large stress the system can be left trapped in a different metabasin with a higher aging rate. This conceptual interpretation leaves many questions unanswered; however, we believe it provides a useful starting point for further investigations. Existing theories on glass deformation<sup>36,37,40,41,43</sup> and simulations that map the inherent structure of the PEL<sup>41,49</sup> could be adapted to verify this interpretation.

## 4.5 Summary and Conclusions

Our results demonstrate that the formation of a glass by a temperature quench under applied stress can lead to less stable glasses with faster physical aging rates above a minimum threshold stress. We interpret these results within the PEL framework as the applied stress acting to distort or tilt the landscape, which for sufficiently large values can

leave the system trapped in a shallower, higher energy metabasin resulting in a less stable glassy state with faster structural relaxation. Vitrifying glasses under stress provides a means of accessing different parts of the PEL not necessarily accessible during thermal quenching, a process which could be used to manipulate the PEL and create glasses with different properties. Similarly, recent studies have found that manipulating the parameters of glass formation using controlled deposition conditions can produce glasses with unique material properties.<sup>136-138</sup> Understanding issues of how stress during glass formation alters the material's stability are particularly important for industrial applications involving polymers where various processing methods impart unintended stresses to the material, for example through thermal expansion mismatch between the polymer and mold.

## Chapter 5

# Mechanical Tensile Testing Apparatus for Controlled Deformation of Polymer Films during Vitrification

### 5.1 Synopsis

In order to further explore the dependence of physical aging rate on applied deformation during the thermal quench, we built a new experimental setup to measure and apply both stress and strain to thin polymer films in a temperature-controlled environment. Before deformation during cooling experiments can be conducted, the new apparatus needs to be extensively tested. In this chapter I will outline the design, construction, calibration, and testing of the apparatus. To further understand the importance of the values of stress applied above the glass transition in the study presented in Chapter 4, we need to understand the mechanical properties of PS above  $T_g$  and the onset of glassy properties as  $T_g$  is approached. I will present measurements of the mechanical properties of PS thin films under uniaxial deformation above and near  $T_g$ . These include the stress response to constant strain rate deformation, stress relaxation, and creep above  $T_g$ .

### 5.2 Introduction

The experiments presented in Chapter 4, detailing the effects of stress during vitrification on the physical aging rate of the subsequent glass, left us with many open

questions.<sup>52</sup> As stress applied during the quench increased, the physical aging rate quickly doubled in magnitude for stresses above  $\sim 8$  MPa for the two highest molecular weight polystyrenes studied (see Figure 4.4). In the potential energy landscape tilting interpretation proposed in Chapter 4, the applied stress needs to be large enough to give the system enough energy to overcome a potential energy barrier to transition to another metabasin. What is significant about the value of this transition stress of  $\sim 8$  MPa?

In order to answer this question, we built a new experimental apparatus. The apparatus used in Chapter 4 could only apply a constant force and no information about instantaneous strain or strain rate could be collected. While the temperature of the device could be controlled, the cooling rate could not be precisely controlled. The new mechanical tensile testing apparatus can apply stress and record strain, or apply a constant strain rate and record stress under controlled temperature and much more precise cooling conditions. The response of bulk PS films (tens of microns thick) to constant strain rate and constant strain deformation above  $T_g$  will be analyzed. These tests will assess the capabilities of the new experimental apparatus.

Before proceeding, I will highlight the known mechanical properties of PS. PS is a widely used material both commercially and academically to study polymer behavior. Far below  $T_g$  PS is a brittle glass. Under deformation, PS behaves elastically, for example stress increases linearly with strain when the strain rate is constant. Brittle, glassy PS yields and breaks at low strains  $< 2\%$  at a stress of 42 MPa.<sup>54</sup> Above the glass transition temperature, PS becomes ductile and eventually flows at very high temperatures. The mechanical response of PS also depends on the time scale over which the deformation is applied. A good illustration of this time-dependence is silly putty. A

quick impact results in silly putty behaving as an elastic solid (for example, bouncing a ball of silly putty on the floor). However, over long times, the silly putty will flow (leave a ball on a desk overnight and the next day it will be a puddle). Qualitatively, at short times and low temperatures, PS behaves as a solid, exhibiting a high modulus on the order of GPa ( $10^9$  Pa). As temperature or time is increased, PS softens. A small molecule would then flow, but due to entanglements in PS of sufficiently high molecular weight, PS then behaves as a rubbery band with a modulus on the order of MPa ( $10^6$  Pa). At times longer than the reptation time (the time for entanglements to relax) PS will flow. A schematic of this behavior is shown in Figure 5.1

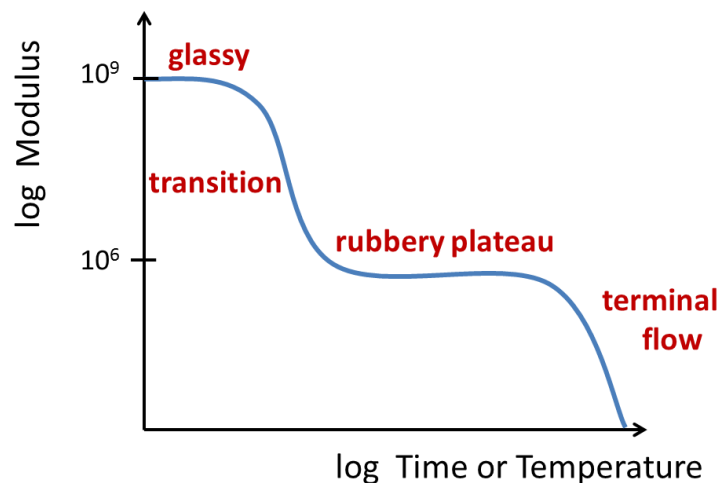


Figure 5.1 Schematic of logarithm of modulus vs. logarithm of time or temperature for entangled PS. At short times or low temperatures, polymers behave as hard, glassy materials. At longer times and higher temperatures, the polymer goes through a transition region from glassy to rubbery behavior if it is entangled. For times less than the reptation time, the polymer has mechanical integrity. At high temperatures and long times, chains reptate out of entanglements and flow occurs.

The mechanical properties of bulk polystyrene samples have been measured in a variety of conditions. Simon and coworkers measured the bulk and shear creep compliance of polycarbonate and PS as a function of time.<sup>139,140</sup> Inoue, Okamoto, and Osaki used elongational dynamic mechanical analysis to measure the stress relaxation

Young's modulus of PS from 90 – 115 °C.<sup>141</sup> They did not observe time-temperature superposition (where shifting  $E(t)$  curves in time based on the experimental temperature causes the curves to superimpose). They described the response of the PS as a combination of glassy and rubbery components that could then be superposed.<sup>141</sup> Fujita and Ninomia measured the stress relaxation Young's modulus and also had trouble with time-temperature superposition in the transition region.<sup>142</sup>

As discussed briefly in Section 4.4, Plazek<sup>131,143,144</sup> carried out studies of the temperature-dependent creep compliance of bulk PS under shear. In a specially designed cell, torsional stress was applied to bulk PS samples and the subsequent creep was recorded as a function of time at various temperatures. The time axis can be greatly extended by shifting creep compliance vs time data at different temperatures in time, a common process utilizing time-temperature superposition of polymers. Time-temperature superposition relies on the assumption that all relaxation times have the same temperature dependence and therefore a long-time response at low temperatures is similar to a short-time response at a higher temperature. This technique allowed Plazek to measure the plateau shear creep compliance of PS to be  $J = 1.2 \times 10^{-5} \text{ Pa}^{-1}$ .<sup>131</sup> If we assume that PS is a linear solid, the plateau elongation compliance,  $D$ , can be given by  $J = 3D$  giving  $D = 4 \times 10^{-6} \text{ Pa}^{-1}$ .<sup>145</sup> The Young's modulus,  $E$ , is  $1/D$  and is then  $E = 2.5 \times 10^5 \text{ Pa}$  (0.25 MPa).<sup>145</sup>

As discussed in Section 2.6.3, the creep compliance of thin polymer films under biaxial tension and confinement has been measured. Using nanobubble inflation, McKenna's group measured the creep compliance under biaxial stress (applied by exerting air pressure on the underside of circular and rectangular free-standing films).<sup>89-91</sup>

McKenna observed stiffening, a lowering in the creep compliance, by up to two orders of magnitude as film thickness decreased.<sup>89-91</sup> Due to the limitations of the nanobubble inflation technique, bulk creep compliance was not recovered but was projected to be recovered at film thicknesses of  $\sim 300$  nm.<sup>90</sup>

The above experiments were done in different geometries or under different conditions than our experimental setup. In both Chapter 4 and the current chapter, uniaxial deformation will be applied to PS films above  $T_g$ . In Chapter 4, a constant load was applied to the polymer film, the corresponding mechanical measurement would be creep compliance. However, creep compliance measurements in the literature were done under biaxial stress,<sup>89-91</sup> shear,<sup>146</sup> or pressure.<sup>146</sup> If PS is in the linear regime, conversions between mechanical properties measured for different geometries are simple. However, the mechanical properties, such as modulus or compliance, of non-linear materials do not simply depend on time but may also depend on the magnitude of strain rate, strain, or stress. When this occurs, conversion between different mechanical properties and different geometries is no longer simple or even possible without extensive knowledge of the material's response to multiple types of deformation.<sup>145</sup> As will be discussed below, PS does not always behave as an ideal linear viscoelastic material. Section 5.3 will detail the design, setup and calibration of the mechanical tensile testing apparatus. Section 5.4 will discuss mechanical measurements of stress and strain for PS under constant strain rate, stress relaxation, and creep for applications of uniaxial deformation.

## 5.3 Experimental Techniques

### 5.3.1 Mechanical Tensile Testing Apparatus: Components and Calibration

In order to explore the mechanical properties of thin polymer films and apply mechanical deformation during the cooling process, we designed and constructed a unique mechanical tensile testing apparatus. First, we will give an overview of the experimental setup before going into detail about each component. The free-standing polymer film is held by a stainless steel sample holder which consists of two components: one of the stainless steel supports is bolted to the hot stage while the other support is attached to a load cell and linear actuator in series as shown in the schematic in Figure 5.2. The temperature of the film is controlled by a hot stage and heated cover (Instec HCS 402) above and below the film and its supports. The micro tensile testing apparatus consists of three components which control motion and monitor position and force: a linear position actuator (Zaber NEMA Size 08), a linear voltage transducer or LVDT (Omega High Accuracy LD620-15), and a load cell (Interface Ultra Low Capacity). This specific actuator and LVDT were chosen as both have high accuracy over a relatively large travel distance of 30 mm. The load cell was chosen as it was one of the only load cells that could measure forces of  $< 0.5$  N with the accuracy it has (see below) and perform in both extension and compression. All three instruments are bolted down to a flat aluminum plate. The load cell is supported on a low-friction translation stage that has a range of 25 mm and is in series with the linear actuator. In parallel, the LVDT is attached to the translation stage the load cell is on.

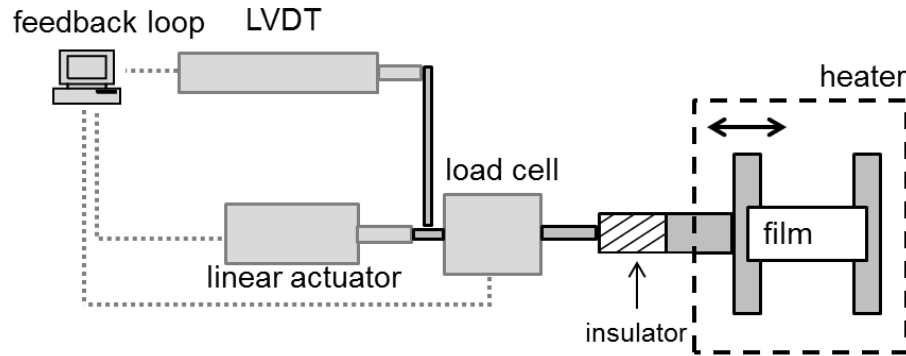


Figure 5.2: Schematic of mechanical tensile testing apparatus. On the right is the sample holder, whose right side is bolted to the hot stage below the film, while the left side floats and is free to move with the motion of the linear actuator. The film is heated from above and below by the Instec heater. The load cell is thermally insulated from the heated frame by an insulating ceramic spacer. The LVDT is in parallel with the load cell and actuator in order to ensure greater accuracy in position measurements in case the actuator skips steps. The actuator motion is controlled by a program in MATLAB.

The stainless steel sample holder which supports the free-standing film consists of two parts. The right half is bolted to the hot stage to provide a firm anchor for one end of the film. The left half of the stainless steel frame is attached, via an insulating piece of ceramic, to the load cell. The bottom surface of the left side of the frame hovers above the hot stage with an approximately 1/8 inch air gap, as shown in Figure 5.3. The level of the left side relative to the right side is checked before each new film is placed on the stainless steel support by placing a small bubble level across the tops of the frame, which should line up in order for the film to be flat. Additionally, there is an M shaped piece, as shown in Figure 5.3b, which can be placed over the left and right halves to join them together into a rigid piece. Two pins can then be inserted into the edges as shown to join the left and right halves together with a spacing of 10 mm across the gap where the film is suspended. This defines the initial length of the film. By joining the two halves of the sample holder into a single rigid piece, this allows us to transfer thin spin-cast films via

the floating method by dipping the connected sample holder into water to pick up the floated film.

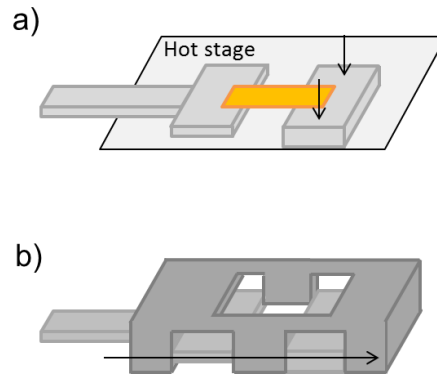


Figure 5.3. Schematic of stainless steel stretching frame. a) Schematic of sample holder with film. Light gray box indicates level of the hot stage: left half of sample holder is 1/8 in above the hot stage while the right half is screwed into the stage, as indicated by the black arrows. b) Sample holder with M-shaped bracket attached to keep the two halves of the sample holder together, two screws (following the black arrow, one in the back not shown) hold sample holder halves and bracket together. Film is floated onto sample holder through the hole in the M-shaped bracket.

The Zaber linear position actuator is used to apply deformation to the polymer film. The linear actuator is a rotary stepper motor with a minimum speed of 0.00045 mm/s and a maximum speed of 14 mm/s. The smallest step size is 0.047625  $\mu\text{m}$  (which is 1/64<sup>th</sup> of a rotation of the internal stepper motor) and a reported accuracy of 25  $\mu\text{m}$ . The main source of the inaccuracy in the linear actuator is from backlash when changing direction, which does not occur in most of the experiments described below. Regardless, the LVDT provides an accurate measure of the strain on the sample. The linear actuator is controlled in MATLAB with commands provided by the manufacturer.

The load cell and the LVDT output voltages between  $\pm 5$  V depending on the load and extension, respectively. A National Instruments data acquisition card (USB-6009) is used to convert the analog output to a digital signal with a maximum sampling rate of 48,000 samples per second. Generally, the voltage of the LVDT and load cell are read 10

times per second and stored in a matrix using MATLAB. After data collection, 10 data points were averaged to give a reading once per second. As will be discussed below, for strain rates of  $0.001 \text{ s}^{-1}$ , this gives us a reading every 0.001 in strain. Data was collected as fast as 100 times per second for faster strain rate experiments.

Attached in series to the linear actuator is the Interface load cell. The load cell operates in both tension and compression and can measure loads up to 0.5 N. The load cell internally deflects under a load, resulting in a change in resistance that is measured by a Wheatstone bridge. The reported nonlinearity of the load cell is  $\pm 0.05\%$  full load or  $\pm 0.00125 \text{ N}$ . The reported creep over twenty minutes is  $\pm 0.1\%$  full load or  $\pm 0.0025 \text{ N}$ . Upon receiving the load cell, we carried out our own calibration tests to obtain the accuracy in force that we can measure. A precision weight set purchased from McMaster-Carr was used to calibrate the load cell by placing the weight on the load cell and taking the average of two voltage readings, as shown in Figure 5.4a. We determined that 1 V output from the load cell corresponds to a 0.1022 N load with an average error of 0.0004 N as shown in Figure 5.4b. While the error in the fit does depend on the magnitude of the load, we will see below that there are other, larger, sources of error.

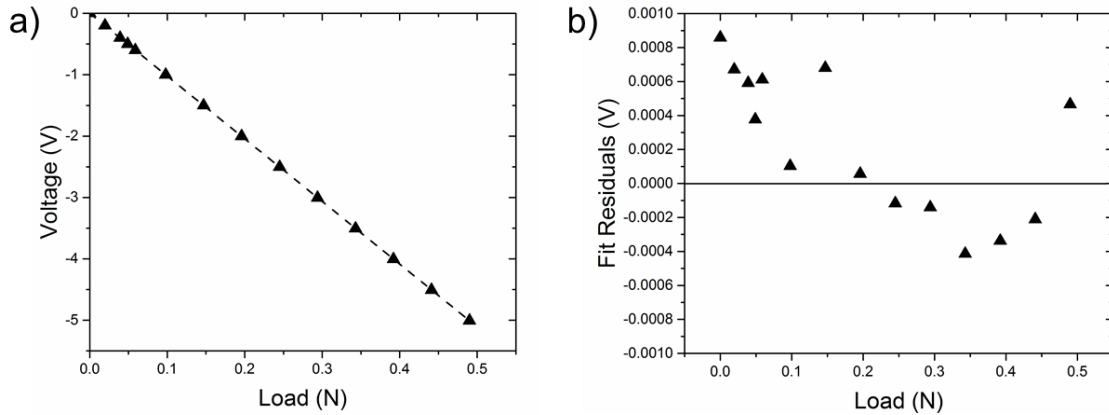


Figure 5.4: a) Load cell calibration curve and linear fit (dashed line) with a slope of 10.22 V/N. The reported slope does not depend on whether or not the fitted line is forced through the origin. b) Residuals from the difference between the measured voltage and the fit vs. load.

In actual test conditions, the load on the load cell is not stationary. There is vibrational noise from both the motor of the linear actuator and the free end of the stainless steel sample holder that vibrates due to the fact that much of its length remains unsupported. The original design had the left half of the sample holder supported on rolling ball bearings. However stick-slip friction overwhelmed the load cell signal despite efforts to try different ball bearing materials and smooth the tracks. We also tried having the left half of the sample holder slide on polished stainless steel rods or rods coated in Teflon. Friction dominated the load cell signal entirely until the left half of the sample was left suspended. There is also torque on the load cell from the weight of the stainless steel sample holder that results in an offset in the voltage the load cell reads when no other load is applied. The load cell has an internal signal conditioner that can add an offset voltage to compensate for the torque applied. The voltage offset is coarse grained so the average zero load voltage with just the frame attached (and no film) is  $\sim -0.22\text{V}$ . This added torque may change the linearity of the load cell. To check all these factors, we measured the voltage as a function of time when there was no film attached to

the load cell while the linear actuator was in motion. Figure 5.5 shows an example of the voltage resulting from the load cell when it is under operational conditions. The voltage is centered around zero as the average voltage ( $-0.4618\text{ V}$ ) over the whole time window is subtracted off. The actuator was only operating from  $t = 5$  to 55 seconds. The standard deviation of the voltage is  $\pm 0.016\text{ V}$  which corresponds to  $\pm 0.0016\text{ N}$ , an order of magnitude higher than the nonlinearity in the load cell with a stationary load applied. I will take this to be the accuracy of the load cell for the following studies.

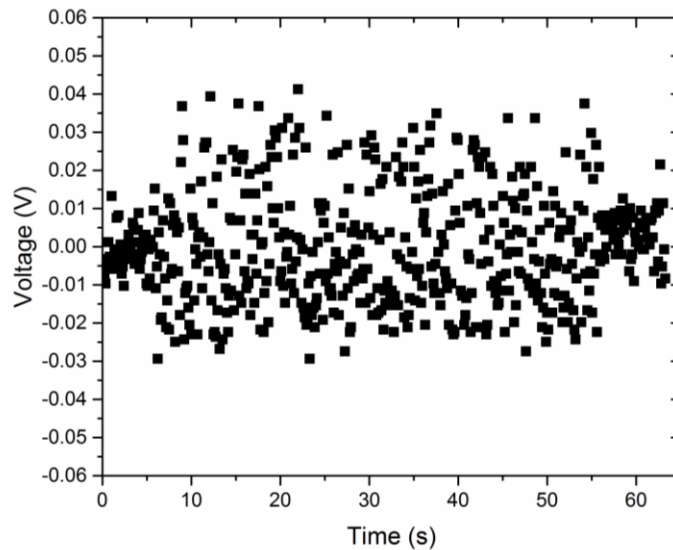


Figure 5.5: Example noise recorded for the load cell when the linear actuator is moving at  $0.01\text{ mm/s}$  (from  $t \sim 5 - 55$  seconds) and the left half of the stainless steel sample holder is attached.

The last component of the mechanical tensile testing apparatus to characterize is the linear voltage displacement transducer (LVDT) that is in parallel with the linear actuator to account for any slipping or speed discrepancies in the actuator (although none are listed by the manufacturer). As the LVDT is extended, a rod moves through a set of three solenoids changing the voltage induced in the outer solenoids by the inner solenoid. The LVDT was mounted on a translation stage that was positioned with a micrometer to a resolution of  $2\text{ }\mu\text{m}$ . Only the first 27 mm of the 30 mm long LVDT could be calibrated

due to the limited travel of the calibration micrometer. (The translation stage the load cell is mounted on is already limited to 25 mm of travel.) Similar to the calibration of the load cell, the LVDT was positioned with a known displacement and the voltage was recorded twice. The output voltage was measured both as the LVDT was extended and as it was pushed back in case hysteresis was an issue. The LVDT was extended and retracted three times and an average voltage calculated for each position as plotted in Figure 5.6. The average voltage was plotted vs. position and fit with a linear curve that resulted in a conversion factor of 2.966 mm per change in 1 V. The average residuals resulted in an error of  $\pm 12$  microns in position.

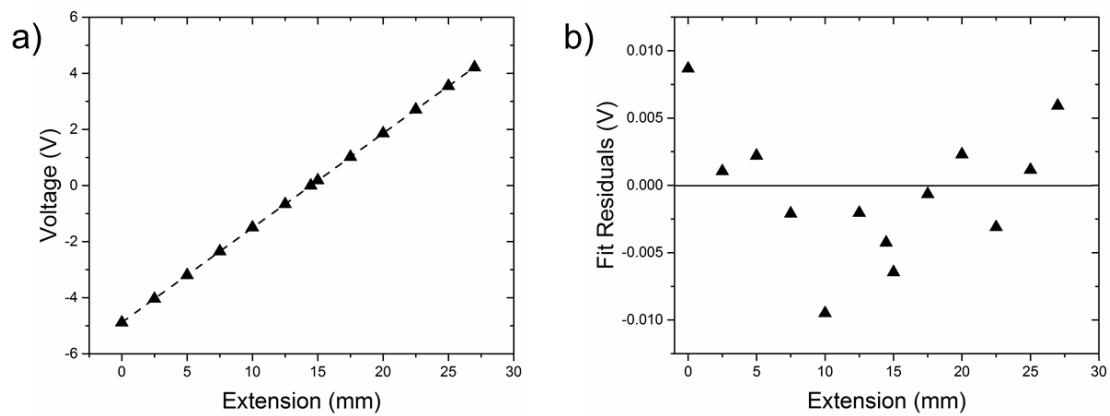


Figure 5.6: a) LVDT calibration curve of average voltage vs. extension for three trials. Linear fit  $V = 0.3371x - 4.8783$  that results in a conversion of 2.966 mm per change in 1 V. b) Difference between the measured voltage and the fit vs. extension.

Once all these components were individually calibrated and characterized, the ability of the apparatus to apply strain and measure force was tested with a simple spring. A compression spring was glued to the stainless steel supports using Krazy glue. The glue was allowed to dry for 10 minutes at room temperature before the supports and the spring were placed in an oven at 120 °C for 20 minutes to further cure the Krazy glue. The stainless steel support cooled to room temperature was then attached to the load cell,

as shown in Figure 5.2, for mechanical testing. For the first 5.6 seconds, the actuator did not move in order to get a baseline reading of the starting position at zero applied load and zero deformation. The average load cell and LVDT reading for the first 5.6 seconds was subtracted off from the load cell and LVDT readings to define 0 load and 0 extension. At 5.6 seconds, the actuator was told to extend the spring at a constant rate of 0.01 mm/s. The LVDT and load cell recorded data every 0.1 seconds. After the test, every 10 data points were averaged together to yield one measurement per second.

A few questions about the tensile testing apparatus can be answered with these spring tests. First, does the actuator accurately capture the initial motion of the actuator, *i.e.* is there a delay between the actuator's motion and the LVDT's motion? We can calculate the extension of the spring in two ways: (1) from assuming the actuator pulls at a constant rate of 0.01 mm/s, or (2) from the signal of the LVDT as discussed above. Figure 5.7 plots the force on the spring vs. extension of the spring from these two methods. The slopes of the two curves are nearly identical, the spring constant measured from assuming a constant strain rate is (1) 0.346 N/mm while the spring constant from the LVDT is (2) 0.331 N/mm (a percent difference of 4.43%). The LVDT signal also began to increase at the same time as the assumed motion of the actuator, indicating that there is no measurable lag between the LVDT's motion and the actuator's motion.

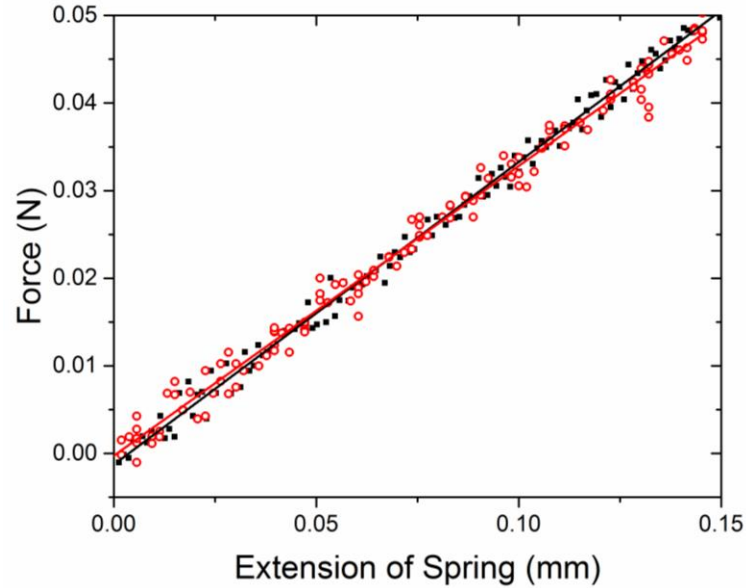


Figure 5.7: Force (N) vs. extension of the spring (mm) calculated by multiplying the time by the strain rate (black squares) or from the LVDT signal (red open circles).

We can also test the reproducibility of the tensile testing apparatus by measuring the spring constant of the spring for multiple extensions and compressions. The actuator was commanded to extend the spring from neutral to an extension of 1.2 mm then compress the spring 2.3 mm, through neutral to a compression of 1.1 mm, and repeat another full extension and retraction. The spring constant on each extension and compression was measured, as shown in Figure 5.8. The average spring constant is 0.32920 N/mm with a standard deviation of 0.0000251. This shows that the measurement of force vs. position of a spring is very repeatable.

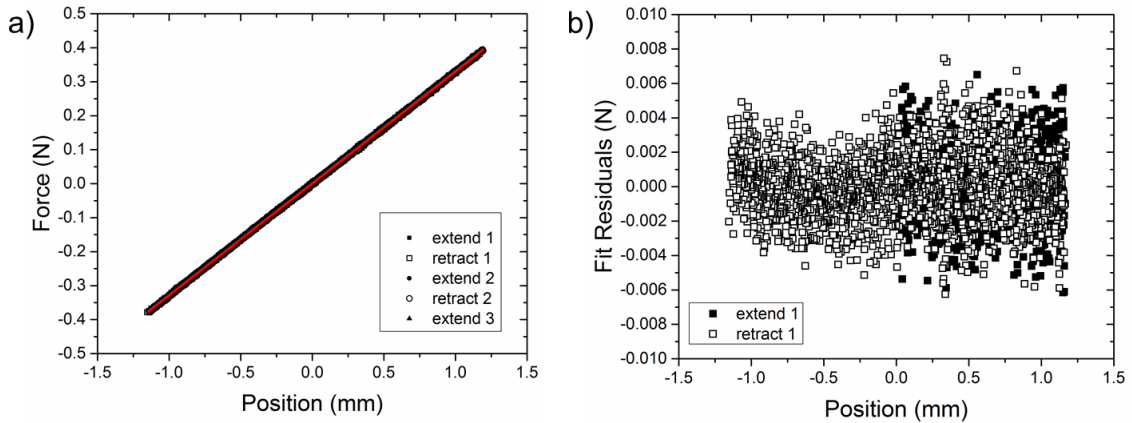


Figure 5.8: a) Force (N) vs. extension or compression (mm) of the spring. The average spring constant was 0.329 N/mm. b) Residuals from the first two force (N) vs. position curve in a).

Another check that there is no lag between the LVDT's motion and that of the linear actuator is to look at the LVDT reading vs. time for cycling a spring through extension and compression as described above. Does the LVDT signal change direction at the same time as the actuator was told to change direction? Figure 5.9 plots the signal from the LVDT vs. time. Vertical lines indicate the times when the actuator was told to change direction. Figure 5.9b and 5.9c show the first two direction changes, clearly indicating that the LVDT reflects the change in direction of the actuator (the other changes in direction look similar). The slope of the lines immediately following the change in direction (first 5 seconds afterwards) are 0.010 mm/s, indicating that both the actuator and the LVDT can accurately change direction and speed.

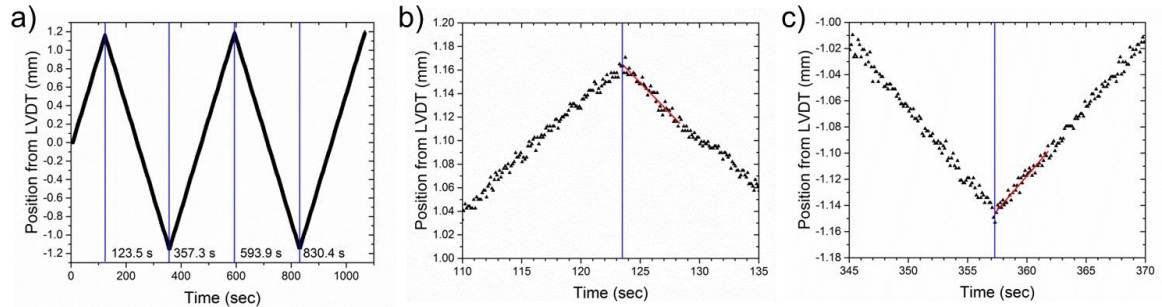


Figure 5.9: Position (mm) as measured by the LVDT vs. time for repeated extensions and compressions of the spring shown in Figure 5.8. a) Vertical blue lines indicate the times at which the actuator is told to change direction. b) Zoomed in view of the first and c) second direction change, indicating that the LVDT promptly responds to change in direction.

One of the goals of this tensile testing apparatus is to apply a constant stress to a polymer film. Can we accurately measure a constant stress? An extended or compressed spring should not relax if the deformation is held constant. Are there any relaxations in the tensile testing apparatus that would complicate measuring and applying a constant force to a polymer film? Figure 5.10 shows an example curve of force (N) vs. time for a spring held at a constant extension. The force was constant to within  $1.8 \times 10^{-4}$  % of its initial value. Two other trials, one in compression to a force of -0.319 N and one under a small extension to a force of 0.0045 N, measured no change in force to within  $2.6 \times 10^{-4}$  % and  $1.2 \times 10^{-2}$  % of the initial force, respectively. (Note: the second percentage is higher as the value of force applied to the spring was much smaller than the other tests, all three tests had slopes of magnitude  $10^{-7}$  N/s.)

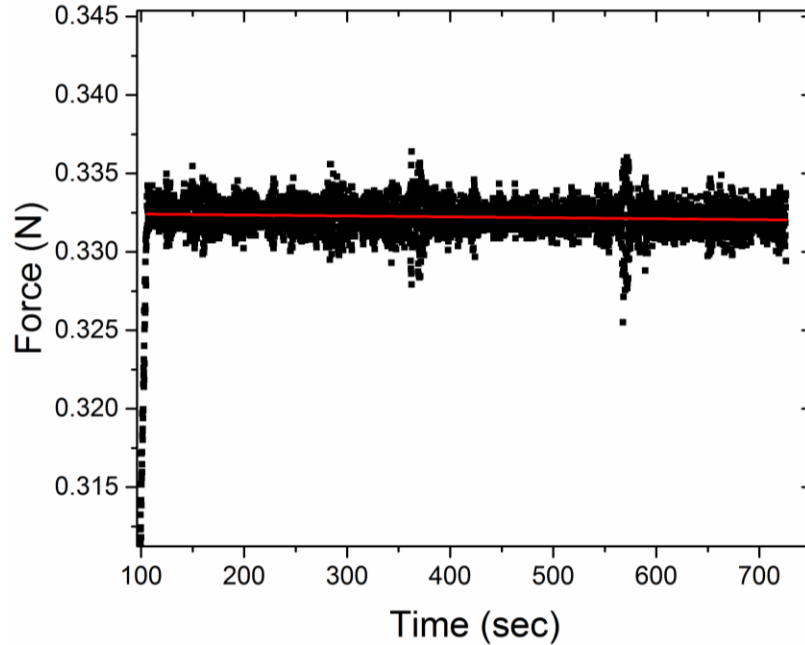


Figure 5.10: Force (N) for a spring extended to a given length and held there after  $t = 106$  s. The slope of the data after 106 seconds is  $-6.0 \times 10^{-7}$  N/s.

In summary, Table 5.1 gives the specifications and calculated errors in each device comprising the mechanical tensile testing apparatus. The quantities for the actuator are as reported by the manufacturer while the minima and resolutions of the LVDT and load cell are determined as discussed above.

	<b>Maximum</b>	<b>Minimum</b>	<b>Resolution</b>
<b>Load Cell</b>	0.5 N	$4 \times 10^{-4}$ N	0.0016 N
<b>LVDT</b>	30 mm	12 $\mu$ m	12 $\mu$ m
<b>Actuator</b>	30 mm	0.047625 $\mu$ m	25 $\mu$ m
<b>Actuator Speed</b>	1.4 mm/s	0.00045 mm/s	

Table 5.1: Technical specifications of the load cell, linear voltage displacement transducer, and linear actuator used in the construction of the mechanical tensile testing apparatus. The resolution of the actuator is large due to the potential for backlash and slipping.

Table 5.2 translates the above specifications of the mechanical tensile testing apparatus into anticipated resolutions in stress and strain for two example thin polymer films undergoing mechanical deformation. The films are assumed to be 2.5 mm wide by

10 mm long in these calculations. As the stress depends inversely on the film thickness, the stress for thicker films will be easier to measure accurately.

	Thin Film (1 $\mu\text{m}$ )	Thick Film (20 $\mu\text{m}$ )
<b>Stress</b>	0.64 MPa	0.032 MPa
<b>Strain</b>	0.0012	0.0012

Table 5.2: Estimated error in measurements of stress and strain for two example film thicknesses, 1  $\mu\text{m}$  and 20  $\mu\text{m}$ . Calculations done for films 1 cm long x 0.25 cm wide.

### 5.3.2 Sample Preparation

For the following studies, polystyrene films of molecular weight  $M_w = 1921$  kg/mol ( $M_w/M_n = 1.26$  from Pressure Chemical) were either spin cast onto mica or solution cast onto clean glass slides from a toluene solution. All films were annealed for at least 12 hours at  $T_g + 20$  °C in a vacuum oven following casting to remove residual solvent. Films were then cut to the desired dimensions, generally  $\sim 2.5$  mm wide such that the initial film length of  $\sim 10$  mm was four times that of the width. Spin cast films were floated onto water and caught on the stainless steel sample holder, whose two halves can be pinned together for the floating procedure. Floated films were allowed to dry on the frame for 30 minutes before use. Solution cast films were cut to the desired dimensions and the thickness was measured with a micrometer to  $\pm 1$  microns. Films were carefully transferred to the sample holder with tweezers then glued down with commercially available Krazy glue (also used by Shi-Qing Wang's group to secure films<sup>147</sup>) that was allowed to dry for 10 minutes before annealing. To obtain a more accurate measurement of film width and length, a picture was taken of each film prior to annealing, and the width and length were measured to within  $\pm 0.05$  mm. Films were then annealed for 15 – 20 minutes at the testing temperature above  $T_g$  to erase thermal history.<sup>61,72</sup>

## 5.4 Results and Discussion

### 5.4.1 Mechanical Behavior of Polystyrene Above $T_g$ Under Constant Strain Rate Deformation

Figure 5.11 plots force vs. time for five separate PS films (23 – 33 microns thick, ~2.5 mm wide, ~10 mm in length free to strain) pulled at a constant speed of 0.01 mm/s (or a strain rate of  $0.001 \text{ s}^{-1}$ ) at  $T = 140 \text{ }^\circ\text{C}$  to strains of either ~0.5 or ~1. Data were collected 10 times per second and averaged to give a force and position reading once per second. The force was calculated from the voltage output of the load cell as  $F = (V - \langle V_0 \rangle) / 10.22 \frac{\text{V}}{\text{N}}$  where  $V$  is the voltage and  $\langle V_0 \rangle$  is the voltage averaged over ~ 5 seconds prior to deformation.

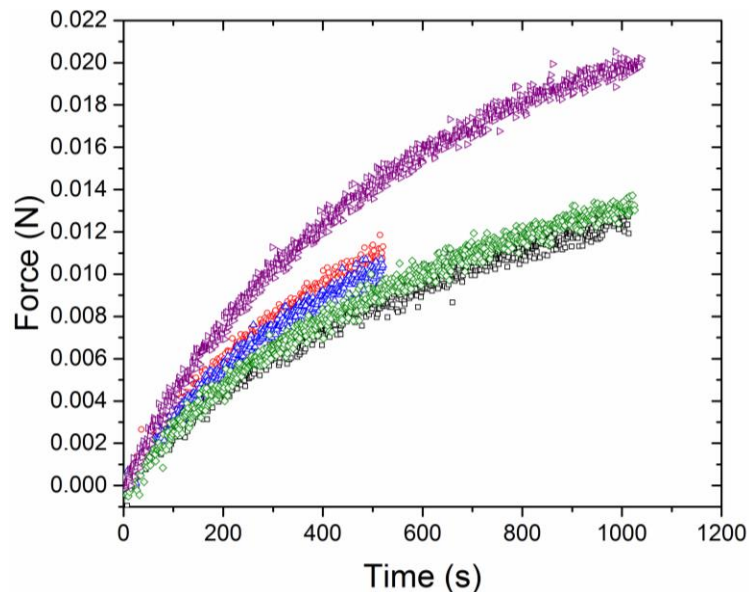


Figure 5.11: Force (N) vs. time (s) for five different PS films under constant uniaxial strain rate of  $0.001 \text{ s}^{-1}$ . The variation in force from film to film is likely due to variations in cross-sectional area (from  $5.38 \times 10^{-8}$  to  $9.50 \times 10^{-8} \text{ m}^2$ ). Blue and green data have the most similar cross-sectional area ( $6.24 \times 10^{-8}$  and  $6.53 \times 10^{-8} \text{ m}^2$  of all the data sets shown above).

Plotted in Figure 5.12 is the calculated stress vs. strain for the same films shown in Figure 5.11. The strain,  $\epsilon$ , was calculated by  $\epsilon = (V - \langle V_0 \rangle) \frac{2.966 \text{ mm/V}}{L_0}$ , where  $V$  is the

LVDT voltage,  $\langle V_0 \rangle$  is the LVDT voltage averaged over  $\sim 5$  seconds prior to deformation, and  $L_0$  is the initial film length. The stress,  $\sigma$ , was calculated by  $\sigma = F/(h_0 w_0)$ , where  $h_0$  is the initial film thickness and  $w_0$  is the initial film width measured prior to deformation. The largest source of error in our measurements are the measurements of film thickness ( $\pm 1 \mu\text{m}$ ) and width ( $\pm 0.05 \text{ mm}$ ). This stress, and all other stresses reported in this chapter, is the engineering stress on the film, as it does not account for the change in cross-sectional area during deformation.

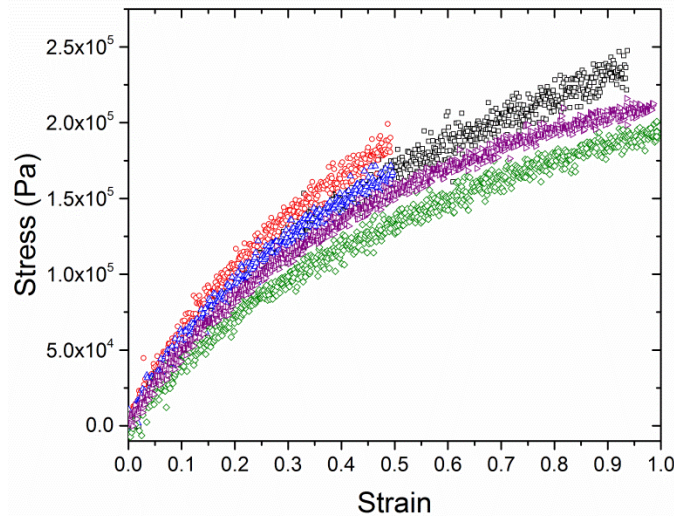


Figure 5.12: Stress (Pa) vs. strain for PS films deformed at  $140 \text{ }^\circ\text{C}$  under constant strain rate of  $0.001 \text{ s}^{-1}$  for the five data sets shown in Figure 5.11.

In Figure 5.12, as strain increases, the stress on the polymer film increases following an exponential decay. Above a strain of  $\sim 50 - 60 \%$  the stress appears to grow linearly with strain. In order to assess how well the apparatus captures the behavior of PS under deformation, we need to review the basic physics behind viscoelastic solids.

Above the glass transition temperature, we expect PS to behave as a viscoelastic material. There are two types of ideal mechanical materials: a linear elastic solid and a linear viscous fluid (also called a Newtonian fluid). A linear material is one whose overall mechanical response is a function of time only and does not depend on the strain

rate or other factors such as magnitude of applied stress or strain. For a viscous liquid, the tensile stress during a constant strain rate experiment would be constant and given by  $\sigma = \eta_e \dot{\epsilon}$ , where  $\eta_e$  is elongational viscosity, and  $\dot{\epsilon}$  is strain rate. At low temperatures and short times PS may behave as an elastic solid where the tensile stress during a constant strain rate experiment,  $\epsilon = \dot{\epsilon}_0 t$ , would be  $\sigma = E\epsilon$ , where  $E$  is the tensile modulus. Most materials are neither simply elastic nor simply viscous but are instead viscoelastic. As can be observed from Figure 5.12, the stress vs. strain behavior is neither constant (as in the viscous case) or linearly increasing (as in the elastic case). The behavior of PS is somewhere between these two extreme cases. Above  $T_g$  PS is a viscoelastic solid for times shorter than the reptation time at that temperature. The elastic response of PS comes from chains adopting non-equilibrium conformations under deformation.<sup>148</sup> If the deformation is removed, the chains will return to more favorable conformations in a manner reminiscent of a spring, thereby storing energy. Energy is dissipated by friction between chain segments leading to a viscous response in the polymer.<sup>148</sup> Recalling Figure 5.1, at long enough times or high enough temperatures, PS will flow.

Linear viscoelastic materials can be modeled in several ways using combinations of springs and dashpots to represent the elastic and viscous behavior of the material. A linear spring is used to represent the elastic contribution while a dashpot (a kind of piston filled with a Newtonian fluid) is used to represent the viscous contribution. The standard linear solid has been shown to successfully predict polymer behavior in the glassy and rubbery regime.<sup>145,149</sup> The range of viscoelastic behavior predicted by the standard linear solid excludes flow, therefore it is only valid for deformations at time scales shorter than the time scale required to observe flow at a given temperature.<sup>145</sup> For this model, the

material is modeled as a spring and dashpot in series, together in parallel with another spring, as shown in Figure 5.13. As will be shown in detail below, this model predicts an increase in stress for small deformations following an exponential decay while the long time behavior of the system is dominated by  $E_R$  resulting in linear growth in stress.

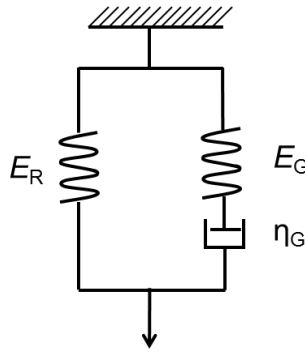


Figure 5.13: Schematic of the standard linear solid spring and dashpot model.

The standard linear solid has been applied in the literature to describe the viscoelastic behavior of amorphous polymers.<sup>150–153</sup> Focusing on PS near and above  $T_g$ , the regime of interest for this chapter, the standard linear solid has been used to model the behavior in the transition regime encompassing both glassy and rubbery behavior.<sup>150,151</sup> Gilbert, Ashby, and Beaumont critiqued the standard linear solid for predicting a sharper transition from the glassy to rubbery state as a function of time or temperature than experimentally observed under dynamic mechanical analysis under shear.<sup>150</sup> Shih-Jung Liu<sup>151</sup> used the standard linear solid to model the mechanical response of PS to compressive stresses applied during injection molding for temperatures up to 150 °C using finite element analysis. Liu reported a sharp drop in relaxation times as the polymer was heated above  $T_g$ , finding relaxation times on the order of  $10^{-2}$  seconds for PS above 120 °C.<sup>151</sup> Modifications of the standard linear solid have also been used to describe the behavior of semi-crystalline polymers.<sup>154</sup> None of these experiments and

models consider uniaxial deformation to PS, nor is there much discussion on comparison of relaxation times to reptation times (time above which flow occurs).

The right hand side of the standard linear solid, the spring and dashpot in series, is called a Maxwell element.<sup>149</sup> The stress in a material represented by a Maxwell element will be shared between the spring and dashpot such that  $\sigma_G = \sigma_{spring,G} = \sigma_{dashpot,G}$ . The deformation will result in strain in the spring and dashpot such that the total strain in the Maxwell element is  $\varepsilon_G = \varepsilon_{spring,G} + \varepsilon_{dashpot,G}$ . The strain rate is then  $\dot{\varepsilon}_G = \dot{\varepsilon}_{spring,G} + \dot{\varepsilon}_{dashpot,G}$ . As stated previously, we know how stress and strain are related for a spring and dashpot, so we can rewrite the strain rate equation as  $\dot{\varepsilon}_G = \dot{\sigma}_G/E_G + \sigma_G/\eta_G$  where the total stress,  $\sigma_G$ , across the Maxwell element can be used as the stress in the spring and dashpot are equal. This equation is a first order linear differential equation and can be solved for stress as a function of time yielding  $\sigma_G(t) = C \exp\left(-\frac{E_G}{\eta_G} t\right) + \eta_G \dot{\varepsilon}$ , where  $C$  is a constant. For the case of a constant strain rate deformation, as shown above in Figure 5.11, the stress at  $t = 0$  is zero and  $C = -\eta_G \dot{\varepsilon}$ . Defining,  $\tau = \eta_G/E_G$  gives  $\sigma_G(t) = \eta_G \dot{\varepsilon} [1 - \exp(-t/\tau)]$ . After the cessation of deformation, stress would relax with a characteristic time constant,  $\tau$ , for the Maxwell element.

Returning to the standard linear solid, the strain in the single spring will be equal to the strain across the Maxwell element  $\varepsilon = \varepsilon_G = \varepsilon_R$  while the stress in the material is equal to the sum of the stresses across the individual spring and Maxwell element:  $\sigma = \sigma_G + \sigma_R$ . In the previous paragraph, we found an expression for  $\sigma_G$  and we know that the stress response of the single spring definition is  $\sigma_R = E_R \varepsilon = E_R \dot{\varepsilon}_0 t$  for constant strain rate deformation where  $\varepsilon = \dot{\varepsilon}_0 t$ . Putting these together and defining  $\tau = \eta_G/E_G$ ,

we find that the predicted stress response for a standard linear solid under constant strain rate deformation is

$$\frac{\sigma(t)}{\dot{\epsilon}_0} = E_R t + E_G \tau \left(1 - \exp(-t/\tau)\right) \quad \text{Eq. 5.1}$$

$E_R$  describes the long time response of PS. Returning to Figure 5.1, this should represent a rubber-like modulus for PS. As discussed in the Section 5.2, the rubbery plateau modulus of PS is 0.25 MPa, assuming PS is a linear solid and converting bulk plateau shear compliance to Young's modulus.<sup>131,145</sup>  $E_G$  is then the short-time response of the material. We can use Eq. 5.1 with  $E_R$ ,  $E_G$ , and  $\tau$  as fitting parameters to model the response of PS above  $T_g$  to constant strain rate deformation. Figure 5.14 shows stress/strain rate vs. time for the data from Figure 5.12 (PS at 140 °C deformed at  $\dot{\epsilon}_0 = 0.001 \text{ s}^{-1}$ ). The solid lines are the fits to the standard linear solid.

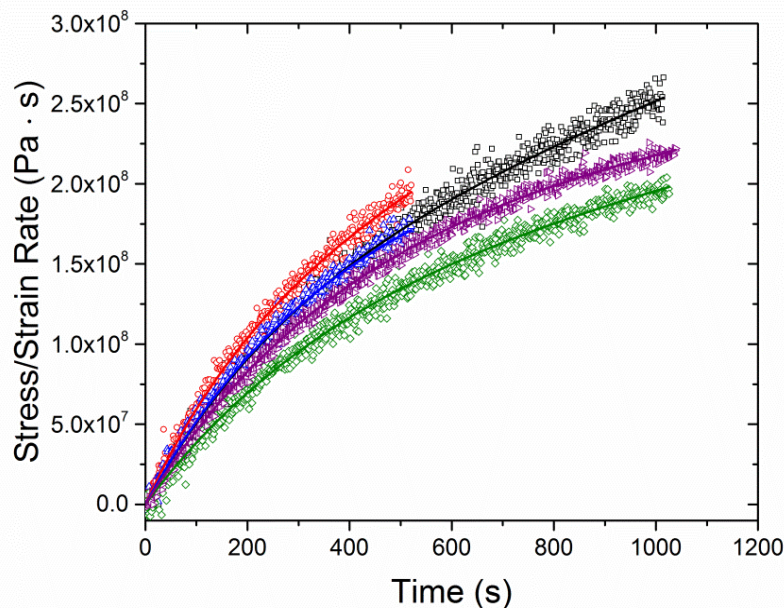


Figure 5.14: Stress/strain rate (Pa s) vs. time (s) for 23 – 33 micron thick PS films deformed at a constant strain rate of  $0.001 \text{ s}^{-1}$  at 140 °C. Solid lines are the fits from the standard linear solid prediction of Eq. 5.1.

The standard linear solid appears to capture the behavior of PS at 140 °C. We find that  $\tau = 340 \pm 70$  seconds,  $E_R = 8.4 \pm 5.0 \times 10^4$  Pa, and  $E_G = 4.7 \pm 0.8 \times 10^5$  Pa. The

parameter  $\tau$  represents the dominant relaxation time of PS at 140 °C. The parameter  $E_R$  captures the rate of increase of stress at long times that should be similar to the ideal elastic response of a rubber, for times less than the reptation time. If we exclude the data sets only taken up to strain of  $\sim 0.5$  (or times of  $\sim 500$  seconds), the average  $E_R$  is  $7.76 \pm 3.84 \times 10^4$  Pa. The larger variation in  $E_R$  and  $E_G$  could be in part from the  $\sim 5\%$  error in determining the cross-sectional area of the film. The better reproducibility of  $\tau$  from sample to sample is not affected by the uncertainty in cross-sectional area. The rubbery elastic component,  $E_R$ , is three times weaker than the rubbery plateau (0.25 MPa). The rubbery plateau modulus occurs over times shorter than the reptation time. Being off the rubbery plateau would explain the low modulus value but we should also see flow. The reptation time for 1921 kg/mol PS is approximately 1 second at 140 °C, so we should see flow after a few seconds, depending on the breadth of the transition region from rubbery plateau to flow. However flow, characterized by a constant stress with increasing strain or time at constant strain rate, is not observed even after hundreds of seconds. The sample has some polydispersity ( $M_w/M_n = 1.26$ ) and chains with twice the molecular weight have a reptation time of 12 s, but the continuation of mechanical integrity for such a long time compared to the reptation time is surprising. The lack of flow on these time scales may indicate a non-linear response to deformation. No flow on time scales greater than the reptation time has been observed in the literature. Zartman, *et al.*<sup>147</sup> exerted uniaxial tensile deformation on bulk PS films at various temperatures above  $T_g$  at a strain rate of  $0.2 \text{ s}^{-1}$ . Qualitatively we observe stress-strain curves of the same shape and similar temperature dependence to that of Zartman, *et al.* The PS they used had a molecular weight of  $M_w = 319 \text{ kg/mol}$ .<sup>147</sup> At 140 °C, this polymer has a reptation time of

approximately 0.002 s. They also do not observe flow at 140 °C on time scales up to 100x this reptation time.

Eq. 5.1 also suggests a scaling relation for the stress response to different constant strain rate deformations. The stress response for different strain rates vs. time should collapse onto one curve if stress is divided by strain rate. Figure 5.15 plots PS at 140 °C for four different strain rates. We see in Figure 5.15 that the curves separate by strain rate especially at long times, indicating that there is not a complete collapse of the data as Eq. 5.1 implies. At short times ( $t$  less than  $\sim 400$  s), it appears that all four strain rates follow a similar trend within the scatter. Separation of stress/strain rate vs. time curve by strain rate could indicate that at large deformations (the same as long times in Figure 5.15) and fast strain rates PS is no longer in the linear regime as Eq. 5.1 only holds in the linear regime. This may also explain the broader distribution of values for  $E_R$  that describes the long time stress response.

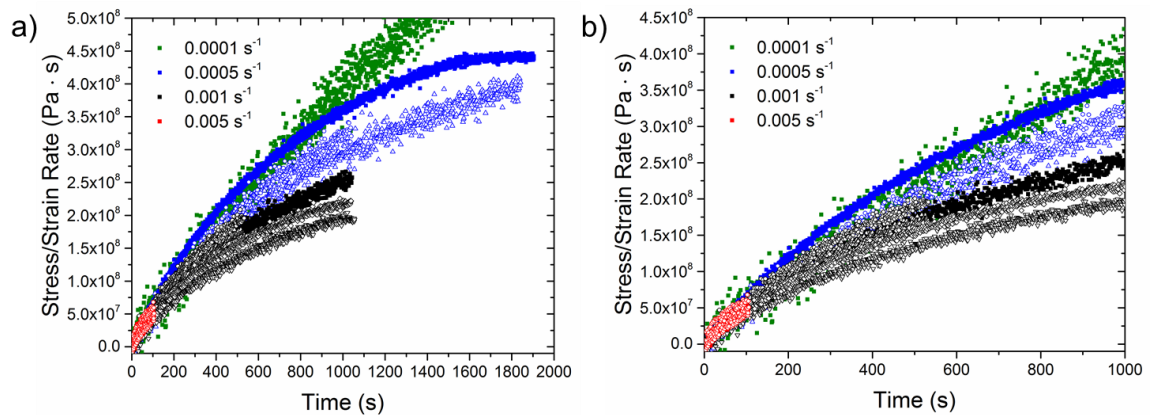


Figure 5.15: a) Stress divided by strain rate vs. time for PS films deformed at four different constant strain rates at 140 °C. b) Zoomed in version of a) to show separation of stress response by strain rate.

To show the strain-rate dependence of the stress response under constant strain rate deformation better, Figure 5.16 plots  $E_R$ ,  $E_G$ , and  $\tau$  vs. strain rate for PS deformed at 140 °C. At slow strain rates, there is less dependence on strain rate for  $E_R$  and  $E_G$  but  $\tau$

still strongly depends on strain rate. Only one PS film was measured at the slowest strain rate discussed above,  $1 \times 10^{-4} \text{ s}^{-1}$  (green curve in Figure 5.15), which looks qualitatively similar to the curves at other strain rates. The fit values of  $E_R$ ,  $E_G$ , and  $\tau$  are much larger than would be expected based on the other three strain rates ( $E_R = -1.4 \times 10^8 \text{ Pa}$ ,  $E_G = 4.7 \times 10^9 \text{ Pa}$  and  $\tau = 3300 \text{ s}$ ). The negative value for  $E_R$  may be due to deformation only out to 50% strain, where  $E_R$  is hard to fit as linear stress vs. time behavior begins for strains above  $\sim 50 - 60\%$ . At low strain rates,  $E_R$  and  $E_G$  do not vary much with strain rate.  $E_R$  appears to increase for the fastest strain rate while  $E_G$  remains constant, however  $E_G$  at the fastest strain rate has large variability from sample to sample. The logarithm of the characteristic relaxation time,  $\log \tau$  decreases approximately linearly with increasing logarithm of strain rate, indicating that relaxation time is inversely proportional to strain rate. Conceptually, at larger strain rates, less time is expected for rearrangements to occur as the rate of deformation introduces displacement over a shorter time period than slower strain rates. We do not observe any region in the strain rates tested that indicates a collapse of the stress vs. time response with strain rate.

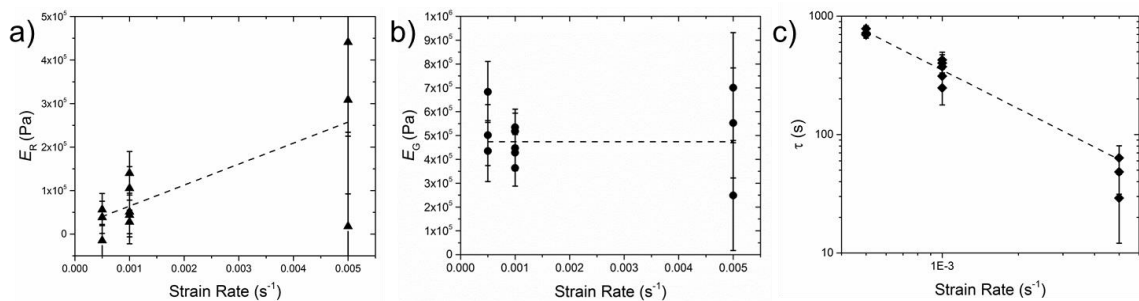


Figure 5.16: Standard linear solid fit parameters for PS deformed at constant strain rate at 140 C. a)  $E_R$  vs. strain rate, b)  $E_G$  vs. strain rate, c) logarithm of  $\tau$  vs. logarithm of strain rate.

We can also examine the behavior of PS films at different temperatures above  $T_g$ .

Figure 5.17 shows the stress vs. time response for representative PS films between  $T =$

110 – 140 °C deformed under a constant strain rate of  $0.001 \text{ s}^{-1}$ . PS films deformed at 120 °C and 130 °C show the same functional form as films deformed at 140 °C and can be adequately described by the standard linear solid. The reptation times of 1921 kg/mol PS are 16 hours and 250 seconds at 120 and 130 °C, therefore rubbery behavior up to 1000 seconds is reasonable for these slightly polydisperse samples. However, very different behavior is exhibited by the film deformed at 110 °C. This behavior is more reminiscent of glassy behavior, where after a short, elastic response, the film yields as seen in the sharp change in slope at small times. The PS then undergoes strain hardening before failing after  $\sim 500$  seconds. As  $T_g$  is approached, yielding at low strains is expected to occur.<sup>155–157</sup> Yielding will be discussed further in Chapter 6.

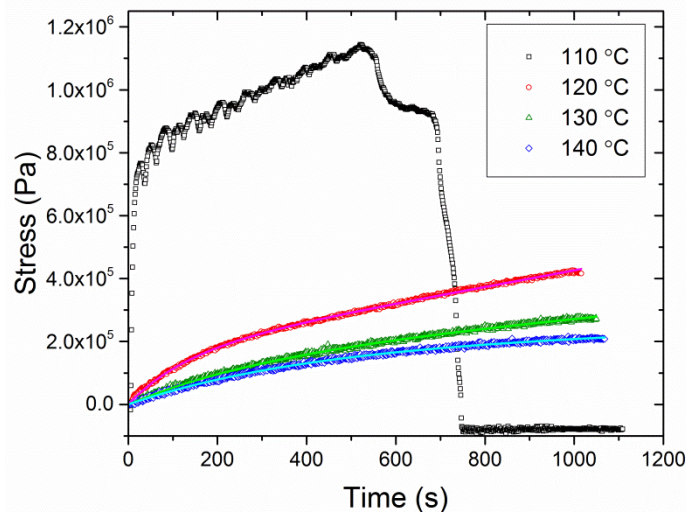


Figure 5.17: Stress vs. time for PS films under constant strain rate deformation of  $0.001 \text{ s}^{-1}$  at various temperatures above  $T_g = 100 \text{ °C}$ . Solid lines are fits to Eq. 5.1 for  $T = 120 - 140 \text{ °C}$ .

The values of  $E_R$  and  $E_G$ , increase with decreasing temperature towards  $T_g$ , as shown in Figure 5.18.  $E_R$  at 120 °C also agrees well with the bulk rubbery plateau modulus. Below  $T_g$ , PS is a glass with a much higher modulus than in the rubbery state above  $T_g$ , as PS approaches  $T_g$  we expect to measure a higher modulus.  $\tau$  decreases with

decreasing temperature contrary to the expectation that relaxation times grow when approaching  $T_g$ . However,  $\tau$  is defined as  $\eta_G/E_G$ . If  $E_G$  has a stronger temperature dependence than  $\eta_G$ ,  $\tau$  would decrease with temperature instead of increasing.

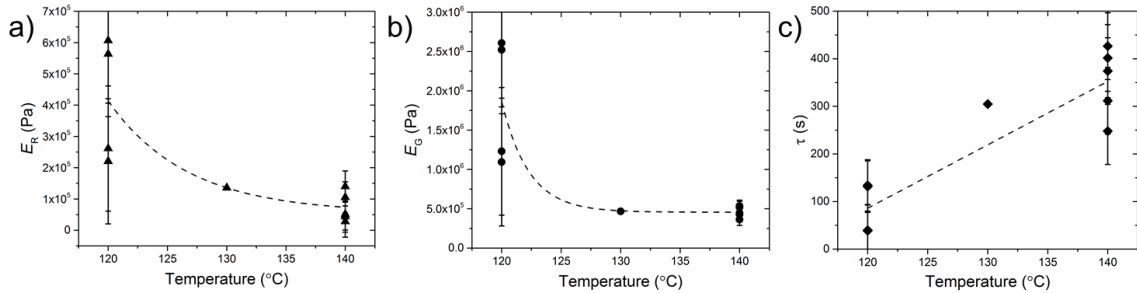


Figure 5.18: Standard linear solid fit parameters for PS deformed at a strain rate of  $1 \times 10^{-3} \text{ s}^{-1}$ . a)  $E_R$  vs. temperature, b)  $E_G$  vs. temperature, c)  $\tau$  vs. temperature. Error bars are the standard deviation of multiple samples at the same strain rate and temperature. Only one film was tested at  $130 \text{ }^\circ\text{C}$ .

The mechanical tensile testing apparatus can clearly assess the stress response to constant strain rate deformation of bulk PS films above  $T_g$ . PS deformed at temperatures above  $120 \text{ }^\circ\text{C}$  ( $T_g + 20 \text{ }^\circ\text{C}$ ) can be described by the standard linear solid, a common model used to predict the viscoelastic behavior of polymers.<sup>149</sup> Modeling PS as a standard linear solid yields an effective relaxation time,  $\tau$ , that depends on strain rate. For PS at  $140 \text{ }^\circ\text{C}$ , the average  $\tau$  at a strain rate of  $5 \times 10^{-4} \text{ s}^{-1}$  is  $707 \pm 65 \text{ s}$ ,  $347 \pm 71 \text{ s}$  for a strain rate of  $0.001 \text{ s}^{-1}$ , and  $45.4 \pm 14 \text{ s}$  at a strain rate of  $0.005 \text{ s}^{-1}$ . This relaxation time represents an effective stress relaxation time and should therefore predict the time-dependent stress behavior if stress is allowed to relax after deformation to a constant strain.

#### 5.4.2 Stress Relaxation of Polystyrene Above $T_g$

Stress relaxation following elongation is another mechanical test that can be performed by the mechanical tensile testing apparatus. After quickly pulling the film to a given strain (or length), the length is held constant and the stress is monitored with the

load cell as the polymer relaxes. The standard linear solid can again inform the behavior of PS under such a deformation. The Maxwell element of the standard linear solid obeys the following equation  $\dot{\varepsilon} = \dot{\sigma}_G/E_G + \sigma_G/\eta_G$  as described in Section 5.4.1. For stress relaxation to occur,  $\dot{\varepsilon}$  must be zero. Setting  $\dot{\varepsilon}$  to be zero and solving for the time-dependent stress results in  $\sigma_G(t) = C \exp(-E_G t/\eta_G)$  where the constant  $C$  is  $\sigma_{\max}$ , the stress immediately following the cessation of deformation at  $t = 0$ . The individual spring of the standard linear solid will contribute a constant to the overall stress equation as  $\sigma_R(t) = E_R \varepsilon$  where  $\varepsilon$  is the final strain and is held constant. Combining these contributions, the standard linear solid predicts the stress relaxation of PS at a constant strain or length as

$$\sigma(t) = E_R \varepsilon + \sigma_{\max} \exp(-t/\tau) \quad \text{Eq. 5.2}$$

where  $E_R$ , and  $\tau = \eta_G/E_G$  are fitting parameters. We will also fit  $\sigma_{\max}$  rather than forcing the fit through  $\sigma$  at  $t = 0$ . Forcing the fit through  $\sigma$  at  $t = 0$  leads to some negative values for  $E_R$  and poor fits overall.

Figure 5.19 shows the stress relaxation of PS at 120, 130, and 140 °C after deformation to a strain of 10%. At lower temperatures, higher stress is achieved for the same strain due to the higher modulus near  $T_g$ . As soon as deformation ceases, the stress begins to relax, at long times, the stress appears to reach a constant. The standard linear solid fits to Eq. 5.2 are shown as solid, colored lines in Figure 5.19a. For lower temperatures, 120 and 130 °C, the standard linear solid fit does not fit the data well, particularly at short times. However, the fit does appear to capture the behavior of the 140 °C data well. Figure 5.19b plots  $\ln(\sigma(t) - E_r \varepsilon)$  where  $E_r \varepsilon$  is found from the

average of the last 50 (or 20 points for 140 °C  $\dot{\epsilon} = 0.1 \text{ s}^{-1}$ ) data points. In Figure 5.19b, black lines are fits to a stretched exponential of the form

$$\ln(\sigma - E_r \epsilon) = \ln(\sigma_{max}) - (t/\tau)^\beta. \quad \text{Eq. 5.3}$$

Data at long times were excluded from the fits; as  $\sigma(t)$  approaches  $E_r \epsilon$ ,  $\ln(\sigma(t) - E_r \epsilon)$  fluctuates and becomes noisy leading to poor fits. Eq. 5.3 follows from rearranging Eq. 5.2, taking the natural logarithm of both sides, and assuming a *distribution* of stress relaxation times instead of one characteristic relaxation time as the standard linear solid presumes. A distribution of relaxation times is a characteristic of glass formers near and below the glass transition temperature and a signature of dynamic heterogeneity.<sup>17</sup>  $\beta$  values less than one indicate a more heterogeneous system.<sup>17</sup> We find that  $\beta$  is less than one and decreases with decreasing temperature, consistent with the idea of growing dynamic heterogeneity as  $T_g$  is approached.

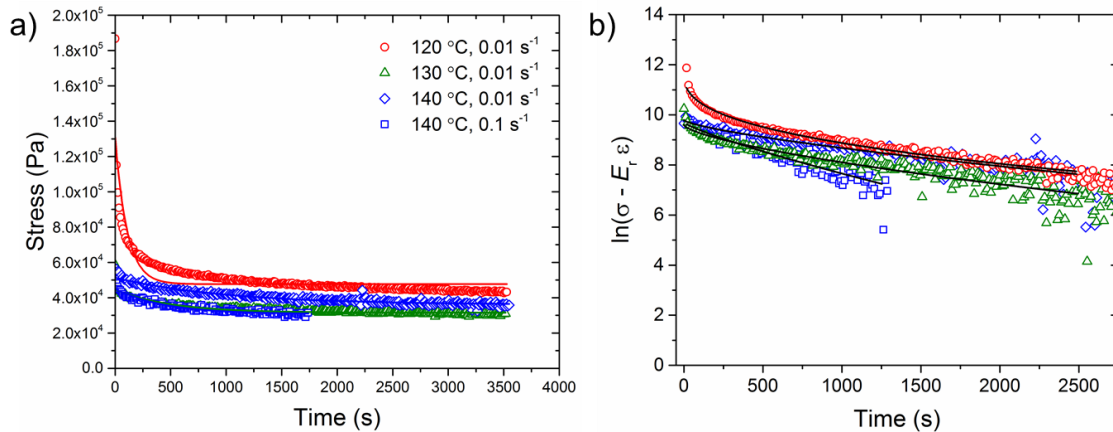


Figure 5.19: a) Stress vs. time for PS films from  $T = 120 - 140 \text{ }^\circ\text{C}$  quickly (see text for discussion) pulled to 10% strain than held at constant length. Solid colored lines are fits to Eq. 5.2. b) Same data as a) but logarithm of the stress minus the long term average stress is plotted vs. time. Solid black lines are fits to Eq. 5.3.

We can then compare the fit parameters from Eq. 5.3 under stress relaxation to those obtained from Eq. 5.1 for constant strain rate deformation measured in Section 5.4.1.  $E_R$  can be obtained from the data in Figure 5.19 by averaging over the last 50 (or

20 points for 140 °C  $\dot{\epsilon} = 0.1 \text{ s}^{-1}$ ) data points of stress and dividing by the strain of 0.1. Table 5.3 compares the fitting parameters from Eqs. 5.3 and 5.1 for stress relaxation and constant strain rate deformation. From Table 5.3, we can see that there is some agreement between  $E_R$  and  $\tau$  obtained from the standard linear solid fits to PS during stress relaxation and under very slow constant strain rate deformation from Section 5.4.1. The large variability in  $E_R$  from sample to sample does not provide a good test of whether the same parameters are valid under constant strain rate deformation or stress relaxation. However, there is reasonable agreement in the characteristic relaxation times for these two mechanical tests.

	120°C	130°C	140°C (0.01 s <sup>-1</sup> )	140°C (0.1 s <sup>-1</sup> )
<b>SR <math>\tau</math> (s)</b>	<b>110</b>	<b>500</b>	<b>1005</b>	<b>440</b>
<b>SR <math>E_R</math> (Pa)</b>	<b>4.4 x 10<sup>5</sup></b>	<b>3.1 x 10<sup>5</sup></b>	<b>3.6 x 10<sup>5</sup></b>	<b>3.0 x 10<sup>5</sup></b>
<b>SR <math>\beta</math></b>	<b>0.44</b>	<b>0.75</b>	<b>0.85</b>	<b>0.84</b>
<b>SLS <math>\tau</math> (s) (0.0005 s<sup>-1</sup>)</b>	<b>130 ± 60</b>	45	<b>735 ± 45</b>	<b>735 ± 45</b>
<b>SLS <math>E_R</math> (Pa) (0.0005 s<sup>-1</sup>)</b>	<b>4.5 ± 2.3 x 10<sup>5</sup></b>	<b>1.7 x 10<sup>5</sup></b>	<b>2.7 ± 3.7 x 10<sup>5</sup></b>	<b>2.7 ± 3.7 x 10<sup>5</sup></b>
<b>SLS <math>\tau</math> (s) (0.001 s<sup>-1</sup>)</b>	90 ± 55	<b>305</b>	290 ± 10	290 ± 10
<b>SLS <math>E_R</math> (Pa) (0.001 s<sup>-1</sup>)</b>	4.1 ± 2.0 x 10 <sup>5</sup>	1.4 x 10 <sup>5</sup>	2.0 ± 1.4 x 10 <sup>5</sup>	2.0 ± 1.4 x 10 <sup>5</sup>

Table 5.3: Characteristic relaxation times and  $\beta$  value fits from Eq. 5.3 for stress relaxation (SR  $\tau$ ) and long-time modulus (SR  $E_R$ ) and for fits from Eq. 5.1 constant strain rate deformations (SLS  $\tau$ ) for strain rates of  $1 \times 10^{-3}$  and  $5 \times 10^{-3} \text{ s}^{-1}$ . Error is from standard deviation of multiple films tested under the same conditions, when multiple films were tested.

### 5.4.3 Polystyrene Creep Above $T_g$

Creep experiments occur when a constant stress is applied and the strain is monitored. The physical aging data reported in Chapter 4 were a result of constant stress applied during the thermal quench. We would like to use the tensile testing apparatus to monitor the strain during this process. Therefore, an understanding of creep at a constant temperature is required before pursuing measurements of changes in strain during a temperature quench. Again, we will use the standard linear solid model. As described in Section 5.4.1., the stress across the standard linear solid is:  $\sigma = E_R \varepsilon + \sigma_G$  where  $\sigma_G$  is the stress across the Maxwell model. The spring and dashpot are in series in the Maxwell model, so the strain across the spring and dashpot sum to the strain across the Maxwell element. The strain rate is then  $\dot{\varepsilon}_G = \dot{\varepsilon}_{spring,G} + \dot{\varepsilon}_{dashpot,G}$ . We know how stress and strain are related for a spring and dashpot, so we can rewrite the strain rate equation as  $\dot{\varepsilon}_G = \dot{\sigma}_G/E_G + \sigma_G/\eta_G$ . For creep,  $\dot{\sigma}_G$  is equal to zero yielding  $\sigma_G = \dot{\varepsilon}_G \eta_G$ . Returning to the whole standard linear solid model, the strain (and strain rate) across the individual spring and the Maxwell element are equal ( $\varepsilon_R = \varepsilon_G$ ). Therefore, the stress across the standard linear solid is  $\sigma = E_R \varepsilon + \dot{\varepsilon}/\eta_G$ . Solving this differential equation yields  $\varepsilon(t) = \frac{\sigma}{E_R} - C \exp(-t/\tau_{eff})$  where  $\tau_{eff} = \eta_G/E_R$ . The constant  $C$  can be found by setting the strain at  $t = 0$  equal to 0. The standard linear solid then predicts that over time, the strain decays exponentially as:

$$\varepsilon(t) = \frac{\sigma}{E_R} [1 - \exp(-t/\tau_{eff})] \quad \text{Eq. 5.4}$$

Eq. 5.4 only holds when the change in stress is equal to zero.

Without knowing the change in cross-sectional area as a function of time, we cannot apply a constant true stress, instead, we apply a constant force or constant

engineering stress. Applying a constant force utilizes the computerized feedback loop of the tensile testing apparatus. The actuator is told to pull at a given speed depending on the force reading from the load cell. If the force is too high, the actuator is told to shorten the length of the film. If the force is too low, the film is lengthened. The force on the film is checked every 0.05 seconds and a command is given to the actuator. During this measurement, we record the force read by the load cell and the position of the film using the LVDT.

Figure 5.20a–b shows an example of a constant stress applied to a PS film at 130 °C. It takes ~75 seconds to reach the desired constant stress of 0.09 MPa. Therefore, we only fit Eq. 5.4 to the strain vs. time data after 75 seconds. Figure 5.20c–d shows an example of a constant stress applied to a PS film at 105 °C. The standard linear solid well describes the strain required to apply a constant stress to a PS film at 130 °C. Even at 105 °C, the standard linear solid describes all but the initial creep well even though features such as yield (not shown) are measurable at this low temperature near  $T_g$ .

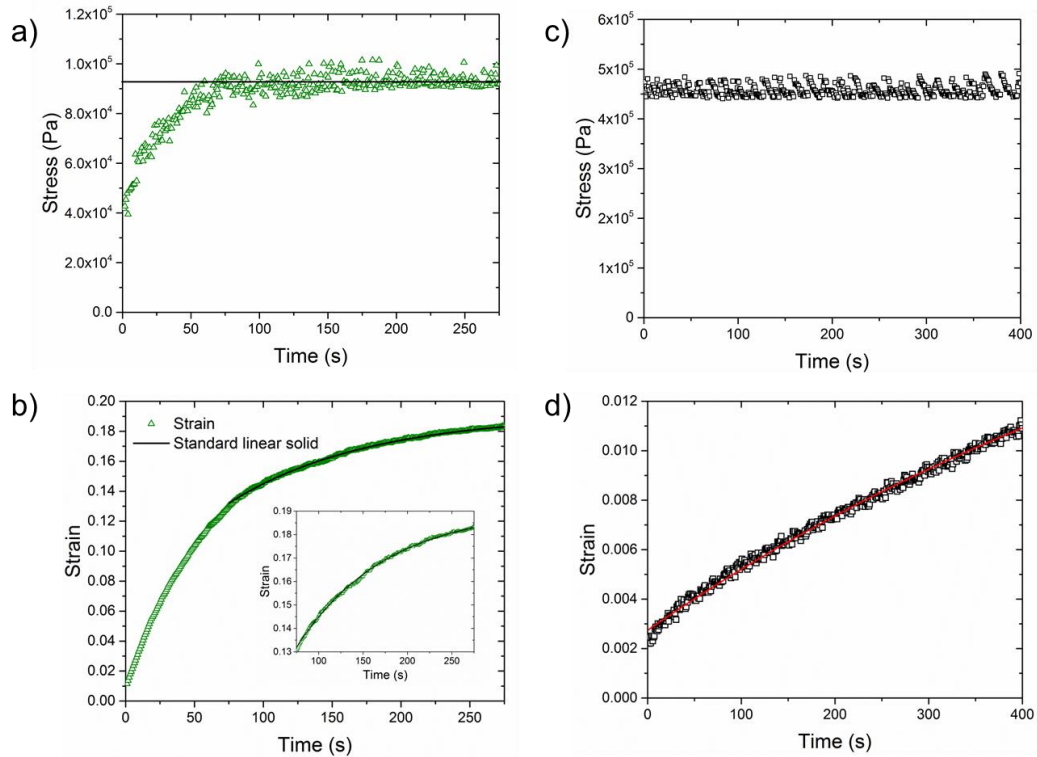


Figure 5.20: a) Stress vs. time for constant stress (0.09 MPa) applied to PS film at 130 °C. Black line corresponds to average stress value for  $t > 75$  s. b) Strain required to apply stress at 130 °C that is constant after  $t \sim 75$  s. Inset shows zoom in on strains for times where stress is constant. Black line is a fit to Equation 5.4 c) Stress vs. time for constant stress ( $\sim 0.45$  MPa) applied to PS film at 105 °C. d) Strain required to apply constant stress at 105 °C. Red line is a fit to Equation 5.4.

## 5.5 Summary and Conclusions

In this chapter I have described the design, construction, and calibration of a mechanical tensile testing apparatus suitable for measuring the mechanical behavior of thin polymer films down to 1  $\mu\text{m}$  thick. The viscoelastic behavior of PS above 120 °C ( $T_g + 20$  °C) was well characterized by the standard linear solid model of viscoelastic behavior. At temperatures below 120 °C, signatures of glassy behavior, such as yield at low strains, appeared. This temperature range will be the focus of the next chapter.

Unfortunately, the new mechanical tensile testing apparatus is not capable of measuring the mechanical properties of thin polymer films less than 1  $\mu\text{m}$  thick. Thinner

films require lower forces to apply the same stress (as stress is proportional to the inverse of film thickness). Therefore, as the film thickness decreases, the forces measured by the load cell also decrease. For films less than  $\sim 1 \mu\text{m}$ , the forces become comparable to the amount of noise in the load cell signal as described in Section 5.3. One of the experiments we would have liked to performed with this apparatus is the apparent stiffening we observed in Chapter 4 for films less than  $\sim 700 \text{ nm}$  thick. However, some modifications to the current setup could be made in order to increase the range of film thicknesses that can be measured. The design of the current heater prevents this, but if the load cell was placed on the other side of the film from the actuator and remained stationary, noise from the cantilevered arm as well as the linear actuator motor could be reduced, thereby allowing the detection of smaller forces.

We also hoped that we could use this apparatus to apply a constant stress on cooling (which we can do as shown in Section 5.4.3) while monitoring not only the strain but also the film thickness. From this we could repeat the aging experiments of Chapter 4 without having to transfer the film. We also hoped to measure temperature dependence of Poisson's ratio in thin films. The current setup has the film in position to be measured with ellipsometry. However, the design only has one side of the film attached to the orientable hot stage. The other side of the film attached to the mechanical tensile testing equipment cannot be tilted. Therefore, alignment of the ellipsometer beam reflected off the sample is difficult. Instead of using the reflected beam, the whole device could be effectively turned on its side with the design of a new heater and sample holder such that the ellipsometer beam passes through the film thickness on its way to the detector. The film would have be oriented at an angle of  $\sim 45^\circ$  to the beam for transmission

ellipsometry to be used. This could be accommodated with a new sample holder. These modifications would not be trivial and may not result in fully expanded capabilities, which is why we have not made them already.

# Chapter 6

## Stress Build Up and Yield in Polymer Films near the Glass Transition

### 6.1 Synopsis

In this chapter I will present experimental studies conducted on the mechanical tensile testing experimental apparatus described in Chapter 5. In Chapter 4, we observed an increase in physical aging rate when PS films were cooled under an applied stress greater than  $\sim 8$  MPa.<sup>52</sup> Here, we would like to investigate the origins of this minimum stress. Measurements of the stress build up on cooling for bulk PS films held at constant length resulting from thermal expansion coefficient mismatch between the film and the stainless steel sample holder are presented here. As the film is cooled, stress begins to build up at temperatures well above the glass transition temperature, up to  $T_g + 16$  °C. Above this temperature, the polymer film is in equilibrium. Below this temperature, the film begins to exhibit signatures of glassy behavior such as a yield stress. For temperatures between  $T_g$  and  $T_g + 15$  °C, we measure the yield stress as a function of temperature. We can compare the work done by the yield stress to the magnitude of the thermal activation energy for the  $\alpha$ -relaxation, a measure of the barrier heights between metabasins in the PEL. We find that the work done by stress becomes greater than the activation energy at  $T = 101$  °C. This indicates that stress enables barrier hopping for temperatures lower than 101 °C if the applied stress is greater than the yield stress at this temperature. The yield stress at 101 °C ( $7.5 \pm 1.2$  MPa) is comparable to the stress we

reported in Chapter 4 (7.6 – 9.0 MPa) above which physical aging rate changes due to stress applied during the thermal quench.<sup>52</sup>

## 6.2 Introduction

Glasses are non-equilibrium solids and are therefore unstable. Over time, glasses evolve leading to a small densification of the material, < 1% reduction in free volume, through a process called structural relaxation.<sup>7-9</sup> This small densification is accompanied by large changes in a host of other material properties such as an increase in modulus<sup>10</sup> and decrease in permeability,<sup>11,12</sup> generally referred to as physical aging.<sup>9</sup> Due to the non-equilibrium nature and many-body interactions of glasses, a comprehensive theoretical description does not exist. However, one useful framework to describe glass formers is the potential energy landscape (PEL).<sup>2,3,26,27</sup> The PEL is a  $3N$  dimensional phase space ( $N$  is the number of particles in the system) where each configuration of molecules in the glass former has a corresponding potential energy.<sup>27</sup> This landscape can be subdivided into energy metabasins consisting of multiple inherent states (individual minima within the PEL) grouped around a local minimum.<sup>27</sup> The PEL is a material property, how the glass former samples the landscape depends on temperature and cooling rate. At high temperatures, the material can sample all metabasins. As the material is cooled, the system is eventually trapped in one metabasin. The cooling rate determines when the system becomes trapped. Faster cooling rates allow for less time to explore the landscape, resulting in the system being trapped in a higher, shallower metabasin. Slower cooling allows the system to find a deeper, steeper metabasin of lower potential energy.<sup>3,26</sup> The glass transition temperature has been shown to depend on cooling rate,<sup>54</sup> as was depicted schematically in Figure 1.1. In Chapter 3, we

characterized how cooling rate affects physical aging rate.<sup>61</sup> Fast cooling leads to faster physical aging compared to the slower physical aging rate at slow cooling rates.<sup>3,8,9,47,61,158</sup> Therefore, we can correlate faster physical aging with higher, shallower metabasins and slower physical aging with deeper, steeper metabasins.

In Chapter 3, I detailed our previous study on the effect of sample holder geometry, quench depth below  $T_g$ , and quench rate on the physical aging rate of polymer glasses.<sup>61</sup> Here, I use the term physical aging rate to mean the logarithmic decrease in total polymer volume over time at temperatures below the glass transition. We observed an increased physical aging rate with decreasing film thickness for polymer films quenched in a free-standing state but not for films quenched in a supported state. We proposed that either the stress present in the films due to the different sample holders and/or the cooling rates between the two geometries could be the source of the thickness-dependent physical aging rate for free-standing films. We found that films quenched through  $T_g$  slower aged slower than films quenched faster, up to cooling rates of  $\sim 100$  °C/min above which the aging rate appeared to be constant with increased cooling rate. This aging rate dependence on quench rate did not explain the film thickness dependent aging rate for films quenched in a free-standing state as free-standing films that cool at thousands of degrees per minute aged slower than supported films cooled at 50 °C/min. Films quenched in a supported state were subjected to a biaxial tensile stress equal to  $\sigma = \frac{E(T)}{1-\nu(T)}(\alpha_{polymer} - \alpha_{substrate})\Delta T$  where  $E$  is the modulus,  $\nu$  is Poisson's ratio of the polymer,  $\alpha$  is the thermal expansion coefficient, and  $\Delta T$  is the change in temperature of interest.<sup>53</sup> This stress does not depend on film thickness. However, the free-standing wire frames exerted a film thickness-dependent stress to the film. The frames resisted the

films contraction with some force,  $F$ , similar to a spring force. The stress on the free-standing film was then  $F/hw$  where  $h$  is the film thickness and  $w$  is the film width; therefore thinner films built up higher applied stresses during cooling in the free-standing state. We proposed that stresses present during the glass formation process may account for these differences.<sup>61</sup>

Stress is often present during the glass formation process. Polymer glasses are created by a variety of techniques and most are processed or formed above  $T_g$  in the viscous liquid state then cooled. Throughout the cooling process, the polymer may be held by a solid support such as glass, silicon, or a metal. During the cooling process, stress can build up in the polymer due to differences in the thermal expansion coefficient of the polymer and the support. Polymers tend to have high thermal expansion coefficients up to two orders of magnitude higher than glass, silicon, and most common metals.<sup>54,55</sup> Zhao, *et al.*<sup>58</sup> directly observed the stress build up on cooling in polystyrene films spin cast on silicon substrates by measuring the bending of the substrate. Following annealing above  $T_g$ , the PS film was cooled to room temperature. Zhao, *et al.* observed no stress build up above  $T_g$ . The stress gradually built up below the glass transition temperature, reaching 15 MPa for bulk films.<sup>58</sup>

In Chapter 4, we directly probed the effect of applied stress during the quench on physical aging rate. We showed that the physical aging rate of polymer glasses is strongly affected by the stress applied during the thermal quench.<sup>52</sup> As stress was increased, the physical aging rate remained constant before quickly doubling over a short range of stress, then remained constant at this high aging rate for further increases in stress. For the two highest molecular weights tested (650 kg/mol and 1440 kg/mol PS),

we found that the stress over which the physical aging rate increased occurred over a range from 7.6 – 9.0 MPa, giving a minimum stress required to increase aging rate of 7.6 MPa. Even though the stress was only applied during the glass formation process and not during the aging measurement, the stability of the subsequent glass was altered.<sup>52</sup>

We proposed that stress can alter the potential energy landscape of the glass.<sup>52</sup> Eyring originally proposed in 1936 that stress could be used to overcome an energy barrier by a factor proportional to the applied stress.<sup>44</sup> Others have expanded upon Eyring's basic model<sup>35-42</sup> to describe observations of enhanced mobility of glasses under deformation.<sup>19,28-34,48-50</sup> As stress is applied, the energy barrier between adjacent minima approaches zero. Once enough stress (or strain) is applied, the glass can then transition from its energy minima into another as the barrier height is reduced toward the thermal energy of the glass.<sup>40</sup> Without the mechanical deformation, the glass would not have enough thermal energy to transition to another metabasin and would continue to age in its original state. Simulations have shown that the system moves up in the potential energy landscape as deformation beyond yield occurs.<sup>34,41,48-50</sup> Once the deformation is over, a reversal of the load does not reverse the change in position in the PEL; the glass remains trapped in a higher, shallower energy minima than prior to deformation.<sup>40</sup>

We proposed that large enough deformation *during the glass formation* process affects the metabasin the system is trapped in during cooling.<sup>52</sup> A glass formed under higher stress is in a higher, shallower potential energy minima with faster physical aging rate than a glass formed under no or low stress. In Chapter 4, we determined the range of stress during the quench over which the subsequent physical aging rate increased; this occurred above a minimum stress of 7.6 MPa. However, we did not determine why this

value of minimum stress was required. Here, we will investigate the stress build up on cooling for PS films above  $T_g$  to help us determine the temperature range over which yield can occur in PS. We then report the yield stress of PS above  $T_g$  and find that the yield stress between 100 – 115 °C is comparable to the stress applied in the experiments from Chapter 4. We will then compare the work done by the yield stress to the thermal activation energy at temperatures near and above  $T_g$ . We find that the work done by the yield stress becomes greater than the thermal activation energy at ~101 °C, indicating that the PEL of films quenched under a stress greater than the yield stress at 101 °C would be sufficient to transition the system to a different metabasin upon cooling.

### 6.3 Experimental Techniques

Polystyrene ( $M_w = 650$  kg/mol,  $M_w/M_n = 1.06$  or 1921 kg/mol,  $M_w/M_n = 1.26$ ) from Pressure Chemical was dissolved in toluene then solution cast onto clean glass slides. All films were annealed for at least 12 hours at  $T_g + 20$  °C (120 °C) under vacuum following casting. Films were then cut to the desired dimensions, ~2.5 mm wide and more than 10 mm long. The film thickness was measured with a micrometer to an accuracy of  $\pm 1$  microns; the films used in this study were between 10 – 30 microns thick. Films were transferred to the mechanical tensile testing apparatus' sample holder such that the initial film length free to strain/stress was ~ 10 mm long. Films were glued down with commercially available Krazy glue that was also used by Shi-Qing Wang's group to secure films<sup>147</sup>. A digital picture was taken of the film prior to annealing and deforming. The film width and length ( $\pm 0.05$  mm) were measured from the picture. The glue was allowed to dry at room temperature for 10 minutes before the film on the sample holder was annealed at the testing temperature above  $T_g$ , 102 – 120 °C, for 20 – 30 minutes.

The details of the mechanical tensile testing apparatus were presented in Chapter 5. In this chapter, we will utilize the apparatus' capability to apply a constant strain rate deformation while recording the change in length of and force applied to the film. While the actuator is moving, the resolution of the load cell was determined to be 0.0016 N. For a film 20 microns thick x 2.5 mm x 10 mm, this corresponds to a resolution in stress of  $3.2 \times 10^4$  Pa. However, when the actuator is stationary, as for the stress build up on cooling experiments in Section 6.4.1, the resolution in stress is higher as will be discussed.

## 6.4 Results and Discussion

### 6.4.1 Stress Build up on Cooling at Constant Length

Polymers, like most materials, contract on cooling or internal stress builds up within the material if not allowed to contract (as discussed in detail in Chapter 3 for the case of a film pinned to a substrate). In the following experiments, we observe stress build up on cooling for PS films held at a fixed length during the cooling process. The stress results from the mismatch in thermal expansion coefficients of the PS and the stainless steel sample holder. Here, the film is under uniaxial stress as it is held on two sides by the sample holder. The stress,  $\sigma$ , is equal to  $E\Delta\alpha\Delta T$  where  $E$  is Young's modulus of the polymer,  $\Delta\alpha$  is the difference in thermal expansion coefficients,  $\alpha_{\text{PS}} - \alpha_{\text{steel}}$ , and  $\Delta T$  is the change in temperature of interest. The thermal expansion coefficients are a function of temperature.<sup>55</sup> The Young's modulus is also a function of temperature, and may be a function of stress, strain rate, or other variables if PS is deformed into the non-linear regime.<sup>145</sup> Therefore, we will directly measure the stress build up on cooling with the mechanical tensile testing apparatus rather than calculating it.

650 kg/mol PS was solution cast onto glass slides yielding films 10 – 20 microns thick. Films were attached to the sample holder following the procedure described above and then annealed at  $T_g + 20$  °C (120 °C) for 20 minutes prior to cooling at the desired rate. Figure 6.1 shows the stress of a film cooling as a function of temperature and cooling rate for four different cooling rates: 0.1, 0.5, 1, and 10 °C/min. As films were cooled from the annealing temperature (120 °C), no stress builds up for temperatures between 120 and 116 °C. The standard deviation about 0 Pa for temperatures between 116 and 120 °C is  $\pm 2.7 \times 10^3$  Pa, providing us with a measure of the accuracy of the stationary load cell. The stationary load cell is  $\sim 10x$  more accurate than when it is in motion with the linear actuator moving (see Section 5.3.1 for a discussion of sources of noise). As the temperature is lowered, stress begins to increase as the film is cooled further. The temperature at which stress begins to build up,  $T_{onset}$ , depends on the cooling rate. Solid lines in Figure 6.1 are fits to a parabolic function truncated by a Heaviside function if  $T$  is greater than  $T_{onset}$  (*i.e.* the stress is set equal to zero):

$$\sigma = A(T_{onset} - T)^2 H(T_{onset} - T). \quad \text{Eq. 6.1}$$

PS films cooled at a faster rate build up stress on cooling at higher temperatures than films cooled more slowly, as seen from the inflection point of the fit lines in Figure 6.1. This trend is expected as PS films cooled faster have less time at a given temperature to equilibrate, therefore falling out of equilibrium at higher temperatures than films cooled more slowly.

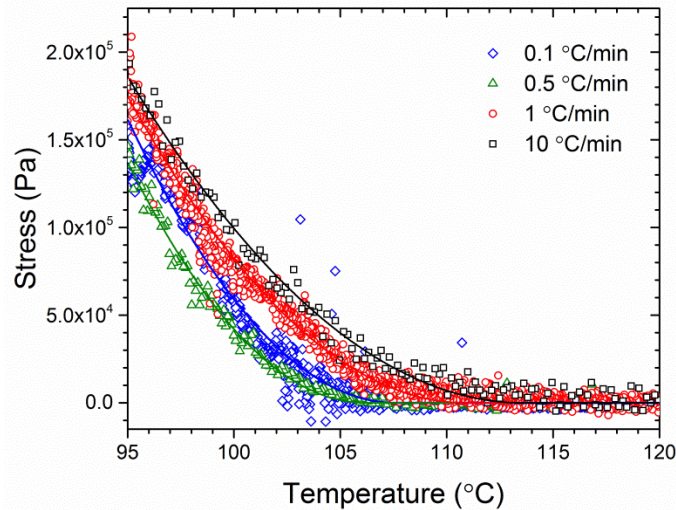


Figure 6.1: Example stress vs. temperature for films cooled from 120°C for four different cooling rates. Solid lines are fits to Eq. 6.1. As cooling rate is increased the temperature at which stress begins to build up increases.

Figure 6.2 shows the temperature at which stress begins to increase,  $T_{\text{onset}}$ , from the fits to Eq. 6.1 vs. cooling rate for cooling rates from 0.1 to 20 °C/min. Stress builds up initially at  $\sim T_g + 7$  °C for the slowest cooling rate of 0.1 °C/min. As the cooling rate is increased, the temperature at which stress builds up rises to  $116 \pm 1.2$  °C ( $T_g + 16$  °C). Above a cooling rate of  $\sim 5$  °C/min, the temperature at which stress begins to increase is independent of cooling rate.

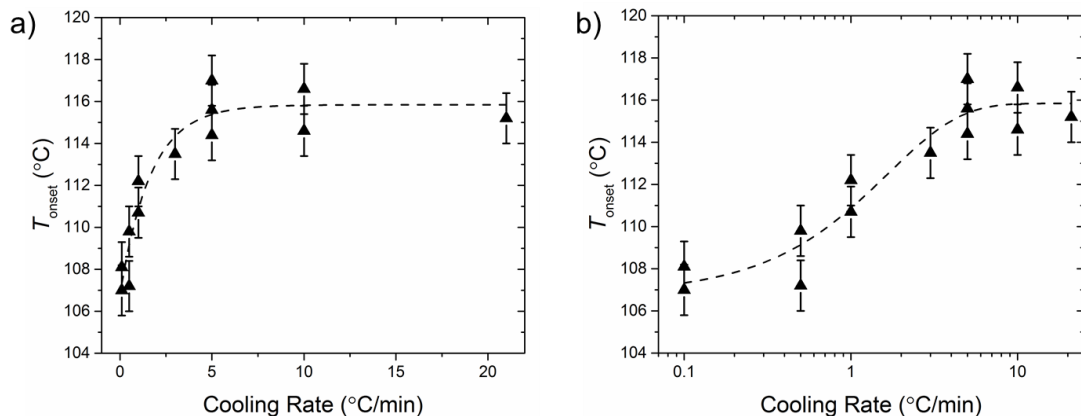


Figure 6.2: a) Temperature at which stress initially increases on cooling,  $T_{\text{onset}}$ , vs. cooling rate for PS films cooled at a fixed length. b) Same data, plotted vs. logarithm of cooling rate. Error bars correspond to the standard deviation in  $T_{\text{onset}}$  for all cooling rates greater than or equal to 5 °C/min. Dashed lines are a guide to the eye.

The high value of  $T_{\text{onset}}$  for modest cooling rates is a little surprising, but is consistent with the stress-strain behavior of PS seen in Chapter 5. In Section 5.4.1, we saw that PS films deformed above 120 °C behave as a standard linear solid, a viscoelastic material. However, at lower temperatures signatures of glassy behavior such as yield began to appear. The data in Figure 6.2 illustrate that this transition from viscoelastic liquid to glassy solid begins at  $116 \pm 1.2$  °C for even modest cooling rates of 5 °C/min. Above, 116 °C, PS is in equilibrium and can relax the stress applied by the thermal expansion coefficient mismatch between the PS and the stainless steel support (at least to within the  $2.7 \times 10^3$  Pa resolution of our apparatus). Glass-like behavior, that results in yield stress at low strains, only occurs for temperatures less than 116 °C. Therefore, in the next section, we will measure the yield stress of PS for temperatures between  $T_g$  and  $T_g + 115$  °C.

#### *6.4.2 Yield above the Glass Transition Temperature*

To measure the yield stress of PS, a constant strain rate deformation was applied to PS films 20 – 30  $\mu\text{m}$  thick on the mechanical tensile testing apparatus while the (engineering) stress of the film was recorded. The yield stress can be determined from the maximum in the stress vs. strain response.<sup>149</sup> Figure 6.3a shows an example stress-strain curve for PS deformed at 102 °C at a constant strain rate of  $0.001 \text{ s}^{-1}$ . For temperatures near  $T_g$ , this definition of yield stress is easily applied to the stress response at constant strain rate deformation. At higher temperatures, there is no clear maximum in stress, however there is a sharp change in curvature of stress vs. strain through yield. Figure 6.3b shows an example stress-strain curve for PS deformed at 110 °C, depicting a large change in slope but not a maximum in stress. The yield stress can then be

determined from the intersection of linear fits (red lines) to the stress vs. strain curve on either side of yield.<sup>149</sup>

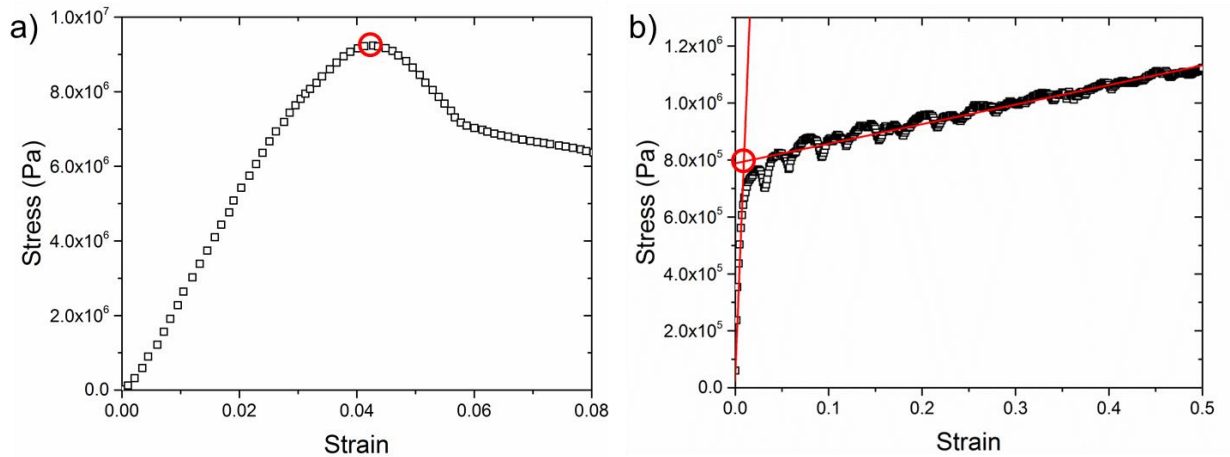


Figure 6.3: Stress (Pa) vs. strain for PS film under constant strain rate ( $0.001 \text{ s}^{-1}$ ) deformation at a)  $102 \text{ }^{\circ}\text{C}$  exhibiting yield as a maximum stress and b)  $110^{\circ}\text{C}$  exhibiting yield as a change in slope. Yield stress values are circled in red.

Plotted in Figure 6.4 is the yield stress of PS vs. temperature for temperatures above  $T_g$ . The yield stress increases as the temperature becomes close to  $T_g$ . There is a strain rate dependence to the yield stress, as shown by the different colored symbols in Figure 6.4. Higher yield stresses are measured for higher strain rates, black symbols correspond to a strain rate of  $0.001 \text{ s}^{-1}$ , compared to green symbols for a strain rate 10x slower of  $10^{-4} \text{ s}^{-1}$ . At  $102 \text{ }^{\circ}\text{C}$ , for example, the yield stress doubles when the strain rate increases by an order of magnitude. The yield stress at lower temperatures could not be measured by the mechanical tensile testing apparatus as the forces required to yield PS films  $20 - 30 \text{ }\mu\text{m}$  thick exceeded the maximum force the load cell can measure.

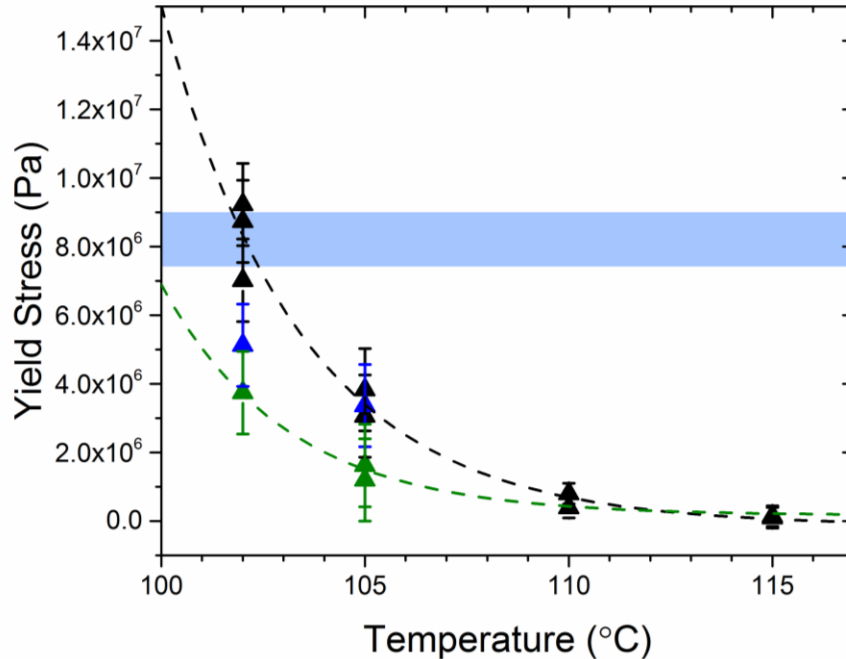


Figure 6.4: Yield stress (Pa) vs. temperature ( $^{\circ}\text{C}$ ) for  $M_w = 1921 \text{ kg/mol}$  PS. Black triangles correspond to data taken at a strain rate of  $0.001 \text{ s}^{-1}$ , blue  $5 \times 10^{-4} \text{ s}^{-1}$ , green  $1 \times 10^{-4} \text{ s}^{-1}$ . Error bars are given by the standard deviation of yield stress measured for different films at a single temperature and strain rate. The blue bar indicates the range of applied stress in Chapter 4 during the thermal quench over which the aging rate of high molecular weight PS films doubled.<sup>52</sup> Dashed lines are exponential fits to the data for strain rates of  $0.001 \text{ s}^{-1}$  (black) and  $10^{-4} \text{ s}^{-1}$  (green).

The blue bar in Figure 6.4 indicates the range of applied stress values over which the transition from low physical aging rate to a higher physical aging occurred in Chapter 4 when stress was applied on cooling. We find that this minimum transition stress is the same as the yield stress at  $102 \text{ }^{\circ}\text{C}$  for the fastest strain rate measured ( $0.001 \text{ s}^{-1}$ ) while being shifted to lower temperatures for lower strain rates. All the stresses applied during the quench in Chapter 4 correspond to yield stresses between  $T_g$  and  $115 \text{ }^{\circ}\text{C}$  for a strain rate of  $0.001 \text{ s}^{-1}$ . From Figure 6.4, we can conclude that the applied stress during the thermal quench previously discussed is of the same order of magnitude as the yield stress at and above the glass transition temperature.

Let's return to the potential energy landscape tilting mechanism introduced in Chapters 2 and 4. In Chapter 4, we proposed that the transition stress of ~8 MPa corresponds to the stress required to tilt the energy landscape sufficiently such that the glass cools into a different metabasin than it would under no or low stress. Eyring<sup>44</sup> originally proposed that stress acted to linearly decrease the barrier height resulting in an enhancement in the relaxation rate that can be written as:

$$\tau_{\alpha} = \tau_0 \exp[(E_A - \sigma V^*)/k_B T] \quad \text{Eq. 6.2}$$

where  $\sigma$  is the applied stress,  $V^*$  is an empirical, temperature-independent activation volume, and  $E_A$  is the thermal activation energy.<sup>37</sup> This is an oversimplification and the scaling relation has been shown to not accurately depict post-yield enhancement of mobility in deformed glasses.<sup>32</sup> However, the Eyring model does agree well with experimental data in the pre-yield regime and up until the point of yield.<sup>32</sup> This equation provides us with a quantitative way to compare the work done by stress on the PEL ( $\sigma V^*/k_B$ ) to the thermal activation energy ( $E_A/k_B$ ), a measure of existing barrier heights in the PEL, as a function of temperature.

We can compare the relative magnitudes of thermal energy and work done by the applied stress for transitioning from one metabasin to another at a given temperature. The activation energy,  $E_A(T)$ , which describes the thermal energy contribution, can be calculated from VFT fits to viscosity data from Plazek and O'Rourke.<sup>131</sup> The Vogel-Fulcher-Tammann (VFT) equation has long been used to fit the temperature dependence of the viscosity of polymers above  $T_g$ . Plazek and O'Rourke collected viscosity data of 600 kg/mol PS using a torsional creep apparatus for temperatures from 119.4 – 180 °C. They fit their temperature-dependent viscosity,  $\eta$ , data to the following equation:

$\eta = A \exp[C/(T - T_{inf})]$  where  $C = 936$  K,  $T_{inf} = 307$  K, and  $A$  is a constant.<sup>131</sup> The viscosity of small molecule fluids follows  $\eta = A \exp(E_A/k_B T)$  where  $k_B$  is Boltzmann's constant. For polymers,  $E_A$  varies with  $T$ . An apparent  $E_A(T)$  can be extracted from the slope of the logarithm of viscosity vs. temperature. To find  $E_A(T)$ , we can set the terms inside the exponentials of the two viscosity equations equal to each other. Therefore,  $E_A/k_B$  is equal to  $C T/(T - T_{inf})$ . We can use this  $E_A(T)$  from viscosity for  $E_A(T)$  in Eq. 6.2 if we assume that all relaxation times have the same temperature dependence.<sup>148</sup> This implies that other dynamic properties such as viscosity scale in the same way as the relaxation times. Here we will extrapolate  $E_A(T)$  from Plazek and O'Rourke's viscosity data down to  $100$  °C ( $T_g$ ). Experimental data of relaxation times below  $T_g$  deviates from VFT,<sup>159</sup> however we will only consider temperatures above  $T_g$ .  $E_A$  divided by  $k_B$  is plotted in Figure 6.5 in red.

For comparison, we can calculate the work done by the yield stress measured in Figure 6.4 as  $\sigma_y V^*/k_B$ , where  $V^*$  is  $9.6 \text{ nm}^3$ .<sup>149,160</sup>  $V^*$  represents the volume a chain segment has to move for a plastic deformation or flow to occur.  $V^*$  can be extracted from experimental data of viscosity vs. shear stress.<sup>160</sup> One criticism of this measure is that  $V^*$  values extracted from experiments and simulations varies from  $1 - 20 \text{ nm}^3$  with no clear correspondence to physical polymer properties.<sup>37</sup>  $\sigma_y V^*/k_B$  is plotted in black and green symbols for the different strain rates in Figure 6.5. The average work from stress (averaged over the two extreme strain rates measured) becomes comparable to the thermal activation energy at  $101.2 \pm 1.2$  °C, corresponding to a yield stress of  $7.5 \pm 1.2$  MPa. Due to the shallow slope of the thermal activation energy vs. temperature, there is

not a strong dependence on strain rate at the point of intersection between the work done by the yield stress and the thermal activation energy.

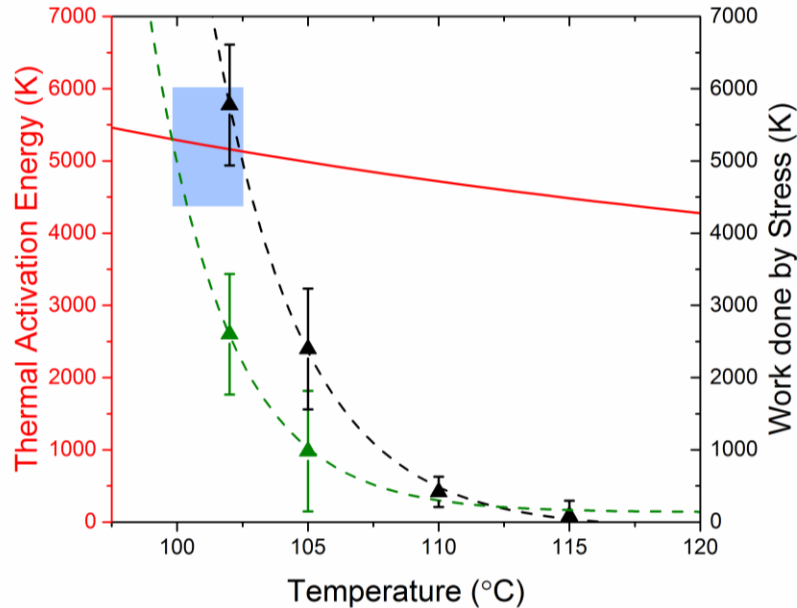


Figure 6.5: Comparison of thermal activation energy (red line) and work done by stress, black ( $0.001 \text{ s}^{-1}$ ) and green triangles ( $10^{-4} \text{ s}^{-1}$ ). Work done by stress becomes larger than thermal activation energy at  $T = 101.2 \pm 1.2 \text{ }^\circ\text{C}$  and corresponding  $\sigma = 7.5 \pm 1.2 \text{ MPa}$ .

By comparing the work done by the yield stress to the thermal activation energy as a function of temperature, we can better understand the minimum applied stress during the quench required to increase the physical aging rate in the measurements of Chapter 4. The transition stress was reported in Chapter 4 as  $7.6 - 9.0 \text{ MPa}$ . This value is within experimental error of the yield stress of  $7.5 \pm 1.2 \text{ MPa}$  at  $101.2 \pm 1.2 \text{ }^\circ\text{C}$ , the intersection where the work done by the stress becomes comparable to the thermal activation energy. Previously, observations of enhanced mobility in glasses under deformation<sup>19,28-33</sup> were described by stress-activated reductions of barrier heights,<sup>35-37,39-42</sup> leading to an increase in the potential energy of the glass during and after post-yield deformation.<sup>40</sup> Similarly, here we propose that stresses above  $7.5 \text{ MPa}$  applied at  $101 \text{ }^\circ\text{C}$  result in a reduction of barrier height of the PEL comparable to the height of the barrier, “tilting” the PEL, and

enabling a transition to a higher energy metabasin than would be possible by thermal energy alone. Our observation of faster physical aging after quenching under high stress is consistent with the system being in a higher, shallower potential energy metabasin.

## 6.5 Summary and Conclusions

In this Chapter, I have shown experimental results of stress build up on cooling of bulk PS films cooled at a fixed length and measurements of the yield stress of PS above  $T_g$ . As PS films held at fixed length are cooled, stress begins to build up at  $116 \pm 1.2$  °C ( $T_g + 16$ ) for cooling rates greater than 5 °C/min. Between  $T_g$  and 116 °C, PS exhibits signs of glass-like behavior such as stress build up from thermal expansion coefficient mismatch between the polymer and the support. In this temperature range, PS can support a yield stress. The yield stress of PS above  $T_g$  has a sharp temperature dependence and grows from ~1 MPa at 115 °C to ~10 MPa near  $T_g$ , depending on the strain rate, with faster strain rates leading to higher yield stresses. Glasses under stress have previously been described by attributing a reduction of barrier heights in the PEL to work done by the applied stress.<sup>35–37,39–42,44</sup> Glasses stressed beyond yield were shown to exhibit different aging trajectories than those stressed pre-yield.<sup>33</sup> Simulations indicated that post-yield deformation resulted in an increase in the glass's potential energy state into a different metabasin than the system was in prior to deformation.<sup>40</sup> For PS near  $T_g$  (101 °C), the work done by the measured yield stress becomes greater than the thermal activation energy of the  $\alpha$ -relaxation, indicating that quenching under a stress greater than this yield stress at 101 °C is sufficient to transition the system to a different metabasin.

# Chapter 7

## Summary

In this dissertation I presented experimental results on how conditions of the glass formation process can affect the physical aging of the subsequent glassy state. In this chapter, I will put my results in the context of the broader field of polymer physics and soft matter physics.

In Chapter 3, I showed that physical aging rate greatly depends on the conditions the glass former experiences during the thermal quench. PS films held in a free-standing state during the quench exhibited faster physical aging with decreasing film thickness whereas films held in a supported state had no film thickness dependence, even though all samples were aged under the same conditions. Free-standing films experienced faster cooling rates and different stress conditions than supported films. To determine the effect of cooling rate on physical aging rate, we controlled the cooling rate of supported PS films. We found that increased cooling rate increased the physical aging rate, though physical aging rate appeared to plateau above a cooling rate of  $\sim 100$  °C/min. Free-standing films were cooled at thousands of degrees per minute in our experiment (simply by opening the oven they were annealed in and exposing them to room temperature air). From our cooling rate experiments, we would expect free-standing films to exhibit no film thickness dependence. Thicker films cool faster but at such high cooling rates we would expect the physical aging rate to be constant. The free-standing films should also have a faster physical aging rate than the supported films that were cooled at 50 °C/min,

however free-standing films aged slower than supported films for all film thicknesses measured. We hypothesized that difference in stress between the two types of supports may account for the different physical aging behavior. Supported films of all thickness experienced a biaxial tensile stress due to the thermal expansion coefficient mismatch between film and support that did not depend on film thickness. Free-standing films experienced a uniaxial tension due to the spring-like wire frame resisting the thermal contraction of the film. The stress on the film was then equal to this force divided by the cross-sectional area of the film; *i.e.* the stress was inversely proportional to film thickness just as the aging rate increased with decreasing film thickness. This work had originally been motivated by observations of accelerated (faster) physical aging in gas separation membranes for film thicknesses below several microns.<sup>11,12,74–80</sup> We proposed that unintended stresses imposed on these films during the thermal quench from the wire frame support may be responsible for the accelerated physical aging. These results were published in *Macromolecules* in 2012.<sup>61</sup>

Since our results were published, Murphy, Freeman, and Paul have conducted gas permeation studies on PS.<sup>161</sup> PS films were spin cast onto glass and dried before a large layer of permeable polydimethylsiloxane (PDMS) was spin cast on top to prevent pinhole defects in the PS during the gas permeability measurements.<sup>161</sup> PS/PDMS films were placed on rectangular wire frames, annealed above the  $T_g$  of PS, then quenched free-standing into the glassy state and aged at 35 °C. Murphy, Freeman, and Paul observed that thinner PS films had a larger decrease in relative permeability over time than thicker films. The rate of permeability decrease and the film thickness dependence of this decrease for PS was less than for polysulfone or Matrimid, polymers commonly used for

gas permeation membranes. They then concluded that as PS has poor permeability and a low  $T_g$  compared to PSF and Matrimid, in addition to having a smaller film-thickness dependent free-standing aging response, PS is not a good model for the aging behavior of polymers used for gas permeation membranes.<sup>161</sup> Direct tests of how stress applied during the thermal quench affects the aging properties of high  $T_g$  polymers could be conducted to make our results in Chapter 4 more applicable to gas separation membranes.

In Chapter 4, we directly tested whether stress applied during the thermal quench to a polymer film could affect the physical aging rate of the subsequent polymer glass. We applied a known uniaxial tension to PS above its glass transition temperature before cooling quickly to room temperature. The PS films were aged in a supported state without the application of stress. At low applied stress, the physical aging rate remained constant. For high molecular weights, above a minimum threshold, the physical aging rate quickly doubled, then remained constant for further increases in stress. These results were published in *Soft Matter* in 2014.<sup>52</sup>

Motivated by our 2012 *Macromolecules* paper,<sup>61</sup> Justin Pye, in our lab, took a different approach to test whether stress affected the physical aging rate of PS. He annealed, quenched, and aged free-standing PS films on rigid frames with circular openings such that the PS films experienced a biaxial tensile stress independent of film thickness and dependent on the thermal expansion coefficient difference between the film and support.<sup>55</sup> To vary the thermal expansion coefficient and therefore the biaxial tensile stress on the polymer film, the frame material was varied. As the thermal expansion coefficient mismatch became larger, the stress on the film was increased and the physical aging rate increased.<sup>55</sup> Pye and Roth's physical aging rate in the limit of zero stress

agrees well with that found in Chapter 4. The details of the application of stress were different between the two experiments. In Pye and Roth, the stress built up as the temperature cooled (as opposed to being constant during cooling) and was also applied during the aging process.<sup>55</sup>

In Chapter 4 and the 2014 Soft Matter paper, we proposed that stress applied during the glass formation process deformed the potential energy landscape, causing the glass to become trapped in a higher potential energy metabasin with corresponding faster physical aging for stresses above a minimum threshold stress.<sup>52</sup> This description followed from previous work describing the “tilting” of the potential energy landscape of a glass when under deformation,<sup>35–42</sup> attempting to explain observations of enhanced molecular mobility.<sup>19,28–34,48–50</sup> In Chapter 6, we measured the yield stress of PS above and near  $T_g$ . We compared the work done by yield stress on the PEL that lowers barrier heights to the thermal activation energy, a measure of barrier height in the PEL, at temperatures above  $T_g$ . We found that the work done by the yield stress became comparable to the thermal activation energy at 101 °C. The minimum stress applied during the quench required to increase the physical aging rate (found in Chapter 4) was in good agreement with the yield stress at 101 °C, where the work done by stress on the PEL becomes comparable to the thermal activation energy.

The existing literature on deforming the potential energy landscape only considers deformation of the glass after it had already been formed. Our work suggests that how you form the glassy state is also very important and should be carefully controlled and monitored. Our results suggest that careful control of the preparation of the glass can enable the exploration of different types of potential energy metabasins within the PEL.

The hope is that a broader sampling of different glassy states and a more thorough understanding of the processes controlling vitrification will aid in the theoretical description of glassy dynamics and the glass transition. Within soft matter physics, there is a growing interest in controlling the glass formation process. For example, Mark Ediger has pioneered work on ultra-stable vapor deposited small molecule glasses.<sup>136,137</sup> By carefully controlling the glass formation process through slow vapor deposition at a controlled temperature, Ediger and coworkers have formed very stable, dense glasses in much deeper potential energy metabasins that were not otherwise experimentally accessible without aging on geological timescales.<sup>136,137</sup>

There are still many open questions concerning glass formation and the potential energy landscape. Future work could include monitoring the strain and strain rate on cooling under constant stress. Combined with the results from Chapter 6 on the yield stress of PS near  $T_g$ , the strain rate on cooling would help provide a real space description of glass formation under stress, to complement the information from the potential energy “tilting” theory. Aging polymer glasses formed under stress to equilibrium could provide more information about the potential energy state of the system. To occur on a reasonable timescale, aging to equilibrium has to be done near  $T_g$ . Aging to equilibrium could be done on films with ellipsometry (preliminary attempts to age bulk samples to equilibrium near  $T_g$  were inconclusive) or for larger, bulk samples with differential scanning calorimetry.

I began this dissertation with a discussion of the jamming phase diagram. Similar to prior results,<sup>28,33,40,47</sup> our work suggests that stress changes the underlying glassy state and does not simply “rejuvenate” the glass as an increase in temperature would.

Therefore, the path the system takes to the glassy state is different during a temperature quench at zero stress than at non-zero stress. Although recent work has cautioned against making direct comparison across diverse soft matter systems,<sup>21–25</sup> I believe broad concepts revealed by this dissertation could be relevant to systems such as granular materials, colloids, and foams. “Rejuvenation” of these materials by shear instead of diluting to lower densities may not be equivalent processes. Peng and McKenna<sup>162</sup> have conducted such experiments, comparing the aging behavior of colloidal glasses following concentration jumps or shear melting. They observed different aging trajectories for colloidal glasses following changes in concentration vs. shear suggesting that these processes do not equivalently alter the structure of the glass.<sup>162</sup>

Our results indicate that more stable glasses can be produced by exerting less stress during the glass formation process. Our experiments in Chapter 3 and 4 revealed that even moderate stresses just from thermal expansion mismatch can alter the physical aging of the glassy state. Understanding the effects of glass formation conditions on the stability of the subsequent glass can aid the industrial design of many polymer products as well as improve our understanding of the fundamental processes behind the glass transition.

# Bibliography

1. Thompson, R. C., Swan, S. H., Moore, C. J. & vom Saal, F. S. Our plastic age. *Philos. Trans. R. Soc. B* **364**, 1973–1976 (2009).
2. Stillinger, F. H. A Topographic View of Supercooled Liquids and Glass Formation. *Science* **267**, 1935–1939 (1995).
3. Debenedetti, P. G. & Stillinger, F. H. Supercooled liquids and the glass transition. *Nature* **410**, 259–267 (2001).
4. Dyre, J. C. Colloquium: The glass transition and elastic models of glass-forming liquids. *Rev. Mod. Phys.* **78**, 953–972 (2006).
5. Biroli, G. & Garrahan, J. P. Perspective: The glass transition. *J. Chem. Phys.* **138**, 12A301 (2013).
6. Liu, A. J. & Nagel, S. R. The Jamming Transition and the Marginally Jammed Solid. *Annu. Rev. Condens. Matter Phys.* **1**, 347–369 (2010).
7. Struik, L. C. E. *Physical Aging in Amorphous Polymers and Other Materials*. (Elsevier Scientific Publishing Co., 1978).
8. Greiner, R. & Schwarzl, F. R. Thermal contraction and volume relaxation of amorphous polymers. *Rheol. Acta* **23**, 378–395 (1984).
9. Hutchinson, J. M. Physical Aging of Polymers. *Prog. Polym. Sci.* **20**, 703–760 (1995).
10. Simon, S. L. in *Encyclopedia of Polymer Science and Technology* (ed. Kroschwitz, J.) 290–318 (Wiley, 2002).
11. Huang, Y. & Paul, D. R. Physical aging of thin glassy polymer films monitored by gas permeability. *Polymer* **45**, 8377–8393 (2004).
12. Huang, Y. & Paul, D. R. Effect of Film Thickness on the Gas-Permeation Characteristics of Glassy Polymer Membranes. *Ind. Eng. Chem. Res.* **46**, 2342–2347 (2007).
13. Liu, A. J. & Nagel, S. R. Jamming is not just cool any more. *Nature* **396**, 21–22 (1998).
14. O’Hern, C. S., Silbert, L. E., Liu, A. J. & Nagel, S. R. Jamming at zero temperature and zero applied stress: The epitome of disorder. *Phys. Rev. E* **68**, 011306 (2003).
15. Cates, M., Wittmer, J., Bouchaud, J.-P. & Claudin, P. Jamming, Force Chains, and Fragile Matter. *Phys. Rev. Lett.* **81**, 1841–1844 (1998).
16. O’Hern, C. S., Liu, A. J. & Nagel, S. R. Effective Temperatures in Driven Systems: Static Versus Time-Dependent Relations. *Phys. Rev. Lett.* **93**, 165702 (2004).

17. Ediger, M. D. Spatially Heterogeneous Dynamics in Supercooled Liquids. *Annu. Rev. Phys. Chem.* **51**, 99–128 (2000).
18. Langer, S. A. & Liu, A. J. Sheared foam as a supercooled liquid? *Europhys. Lett.* **49**, 68–74 (2000).
19. Corwin, E. I., Jaeger, H. M. & Nagel, S. R. Structural signature of jamming in granular media. *Nature* **435**, 1075–1078 (2005).
20. Ciamarra, M. P., Nicodemi, M. & Coniglio, A. Recent results on the jamming phase diagram. *Soft Matter* **6**, 2871–2874 (2010).
21. Parisi, G. & Zamponi, F. The ideal glass transition of hard spheres. *J. Chem. Phys.* **123**, (2005).
22. Mari, R., Krzakala, F. & Kurchan, J. Jamming versus glass transitions. *Phys. Rev. Lett.* **103**, 1–4 (2009).
23. Berthier, L. & Witten, T. A. Compressing nearly hard sphere fluids increases glass fragility. *Europhys. Lett.* **86**, 10001 (2008).
24. Ikeda, A., Berthier, L. & Sollich, P. Unified study of glass and jamming rheology in soft particle systems. *Phys. Rev. Lett.* **109**, 018301 (2012).
25. Ikeda, A., Berthier, L. & Sollich, P. Disentangling glass and jamming physics in the rheology of soft materials. *Soft Matter* **9**, 7669 – 7683 (2013).
26. Sastry, S., Debenedetti, P. G. & Stillinger, F. H. Signatures of distinct dynamical regimes in the energy landscape of a glass-forming liquid. *Nature* **393**, 554–557 (1998).
27. Heuer, A. Exploring the potential energy landscape of glass-forming systems: from inherent structures via metabasins to macroscopic transport. *J. Phys. Condens. Matter* **20**, 373101 (2008).
28. Viasnoff, V. & Lequeux, F. Rejuvenation and Overaging in a Colloidal Glass under Shear. *Phys. Rev. Lett.* **89**, 065701 (2002).
29. Loo, L. S., Cohen, R. E. & Gleason, K. K. Chain Mobility in the Amorphous Region of Nylon 6 Observed under Active Uniaxial Deformation. *Science* **288**, 116–119 (2000).
30. Colucci, D. M., O’Connell, P. A. & McKenna, G. B. Stress relaxation experiments in polycarbonate: A comparison of volume changes for two commercial grades. *Polym. Eng. Sci.* **37**, 1469–1474 (1997).
31. Lee, H.-N., Paeng, K., Swallen, S. F. & Ediger, M. D. Dye reorientation as a probe of stress-induced mobility in polymer glasses. *J. Chem. Phys.* **128**, 134902 (2008).
32. Lee, H.-N., Paeng, K., Swallen, S. F. & Ediger, M. D. Direct measurement of molecular mobility in actively deformed polymer glasses. *Science* **323**, 231–4 (2009).

33. Lee, H.-N. & Ediger, M. D. Mechanical Rejuvenation in Poly(methyl methacrylate) Glasses? Molecular Mobility after Deformation. *Macromolecules* **43**, 5863–5873 (2010).
34. Lee, H.-N., Riggleman, R. A., de Pablo, J. J. & Ediger, M. D. Deformation-Induced Mobility in Polymer Glasses during Multistep Creep Experiments and Simulations. *Macromolecules* **42**, 4328–4336 (2009).
35. Chen, K. & Schweizer, K. S. Theory of aging, rejuvenation, and the nonequilibrium steady state in deformed polymer glasses. *Phys. Rev. E* **82**, 041804 (2010).
36. Chen, K. & Schweizer, K. S. Theory of Yielding, Strain Softening, and Steady Plastic Flow in Polymer Glasses under Constant Strain Rate Deformation. *Macromolecules* **44**, 3988–4000 (2011).
37. Chen, K. & Schweizer, K. S. Stress-enhanced mobility and dynamic yielding in polymer glasses. *Europhys. Lett.* **79**, 26006 (2007).
38. Chen, K. & Schweizer, K. S. Microscopic Constitutive Equation Theory for the Nonlinear Mechanical Response of Polymer Glasses. *Macromolecules* **41**, 5908–5918 (2008).
39. Malandro, D. L. & Lacks, D. J. Molecular-Level Mechanical Instabilities and Enhanced Self-Diffusion in Flowing Liquids. *Phys. Rev. Lett.* **81**, 5576–5579 (1998).
40. Lacks, D. J. & Osborne, M. J. Energy Landscape Picture of Overaging and Rejuvenation in a Sheared Glass. *Phys. Rev. Lett.* **93**, 255501 (2004).
41. Chung, Y. G. & Lacks, D. J. How Deformation Enhances Mobility in a Polymer Glass. *Macromolecules* **45**, 4416–4421 (2012).
42. Chung, Y. G. & Lacks, D. J. Atomic mobility in strained glassy polymers: The role of fold catastrophes on the potential energy surface. *J. Polym. Sci. Part B Polym. Phys.* **50**, 1733–1739 (2012).
43. Chung, Y. G. & Lacks, D. J. Atomic mobility in a polymer glass after shear and thermal cycles. *J. Phys. Chem. B* **116**, 14201–14205 (2012).
44. Eyring, H. Viscosity, Plasticity, and Diffusion as Examples of Absolute Reaction Rates. *J. Chem. Phys.* **4**, 283–291 (1936).
45. Maloney, C. E. & Lacks, D. J. Energy barrier scalings in driven systems. *Phys. Rev. E* **73**, 061106 (2006).
46. Struik, L. C. E. On the rejuvenation of physically aged polymers by mechanical deformation. *Polymer* **38**, 4053–4057 (1997).
47. McKenna, G. B. Mechanical rejuvenation in polymer glasses: fact or fallacy? *J. Phys. Condens. Matter* **737**, S737 – S763 (2003).

48. Riggleman, R. A., Lee, H.-N., Ediger, M. D. & de Pablo, J. J. Free Volume and Finite-Size Effects in a Polymer Glass under Stress. *Phys. Rev. Lett.* **99**, 215501 (2007).
49. Riggleman, R. A., Schweizer, K. S. & de Pablo, J. J. Nonlinear Creep in a Polymer Glass. *Macromolecules* **41**, 4969–4977 (2008).
50. Riggleman, R. A., Lee, H.-N., Ediger, M. D. & de Pablo, J. J. Heterogeneous dynamics during deformation of a polymer glass. *Soft Matter* **6**, 287–291 (2010).
51. Riggleman, R. A., Toepferwein, G. N., Papakonstantopoulos, G. J. & de Pablo, J. J. Dynamics of a Glassy Polymer Nanocomposite during Active Deformation. *Macromolecules* **42**, 3632–3640 (2009).
52. Gray, L. A. G. & Roth, C. B. Stability of polymer glasses vitrified under stress. *Soft Matter* **10**, 1572 – 1578 (2014).
53. Benham, P. P., Crawford, R. J. & Armstrong, C. G. *Mechanics of Engineering Materials*. (Longman Addison Wesley, 1996).
54. Brandrup, J., Immergut, E. H. & Grulke, E. A. *Polymer Handbook*. (Wiley, 1999).
55. Pye, J. E. & Roth, C. B. Physical Aging of Polymer Films Quenched and Measured Free-Standing via Ellipsometry: Controlling Stress Imparted by Thermal Expansion Mismatch between Film and Support. *Macromolecules* **46**, 9455–9463 (2013).
56. Beaucage, G., Composto, R. J. & Stein, R. S. Ellipsometric study of the glass transition and thermal expansion coefficients of thin polymer films. *J. Polym. Sci. Part B Polym. Phys.* **31**, 319–326 (1993).
57. Rosen, S. L. *Fundamental Principles of Polymeric Materials*. (John Wiley & Sons, 1993).
58. Zhao, J.-H., Kiene, M., Hu, C. & Ho, P. S. Thermal stress and glass transition of ultrathin polystyrene films. *Appl. Phys. Lett.* **77**, 2843 (2000).
59. Chung, J. Y., Chastek, T. Q., Fasolka, M. J., Ro, H. W. & Stafford, C. M. Quantifying residual stress in nanoscale thin polymer films via surface wrinkling. *ACS Nano* **3**, 844–852 (2009).
60. Thomas, K. R. & Steiner, U. Direct stress measurements in thin polymer films. *Soft Matter* **15**, 7839–7842 (2011).
61. Gray, L. A. G., Yoon, S. W., Pahner, W. A., Davidheiser, J. E. & Roth, C. B. Importance of Quench Conditions on the Subsequent Physical Aging Rate of Glassy Polymer Films. *Macromolecules* **45**, 1701–1709 (2012).
62. Keddie, J. L., Jones, R. A. L. & Cory, R. A. Size-Dependent Depression of the Glass Transition Temperature in Polymer Films. *Europhys. Lett.* **27**, 59–64 (1994).

63. Ediger, M. D. & Forrest, J. A. Dynamics near free surfaces and the glass transition in thin polymer films: A view to the future. *Macromolecules* **47**, 471–478 (2014).
64. Dalnoki-Veress, K., Forrest, J. A., Murray, C., Gigault, C. & Dutcher, J. R. Molecular weight dependence of reductions in the glass transition temperature of thin, freely standing polymer films. *Phys. Rev. E* **63**, 031801 (2001).
65. Roth, C. B. & Torkelson, J. M. Selectively Probing the Glass Transition Temperature in Multilayer Polymer Films: Equivalence of Block Copolymers and Multilayer Films of Different Homopolymers. *Macromolecules* **40**, 3328–3336 (2007).
66. Pye, J. E., Rohald, K. A., Baker, E. A. & Roth, C. B. Physical Aging in Ultrathin Polystyrene Films: Evidence of a Gradient in Dynamics at the Free Surface and Its Connection to the Glass Transition Temperature Reductions. *Macromolecules* **43**, 8296–8303 (2010).
67. Kawana, S. & Jones, R. A. L. Effect of physical ageing in thin glassy polymer films. *Eur. Phys. Journal. E* **10**, 223–230 (2003).
68. Priestley, R. D., Broadbelt, L. J. & Torkelson, J. M. Physical Aging of Ultrathin Polymer Films above and below the Bulk Glass Transition Temperature: Effects of Attractive vs Neutral Polymer-Substrate Interactions Measured by Fluorescence. *Macromolecules* **38**, 654–657 (2005).
69. Priestley, R. D., Ellison, C. J., Broadbelt, L. J. & Torkelson, J. M. Structural relaxation of polymer glasses at surfaces, interfaces, and in between. *Science* **309**, 456–459 (2005).
70. Koh, Y. P. & Simon, S. L. Structural Relaxation of Stacked Ultrathin Polystyrene Films. *J. Polym. Sci. Part B* **46**, 2741–2753 (2008).
71. Rowe, B. W., Freeman, B. D. & Paul, D. R. Physical aging of ultrathin glassy polymer films tracked by gas permeability. *Polymer* **50**, 5565–5575 (2009).
72. Baker, E. A., Rittigstein, P., Torkelson, J. M. & Roth, C. B. Streamlined Ellipsometry Procedure for Characterizing Physical Aging Rates of Thin Polymer Films. *J. Polym. Sci. Part B Polym. Phys.* **47**, 2509–2519 (2009).
73. Rowe, B. W., Pas, S. J., Hill, A. J., Suzuki, R., Freeman, B. D. & Paul, D. R. A variable energy positron annihilation lifetime spectroscopy study of physical aging in thin glassy polymer films. *Polymer* **50**, 6149–6156 (2009).
74. Pfromm, P. H. & Koros, W. J. Accelerated physical ageing of thin glassy polymer films : evidence from gas transport measurements. *Polymer* **36**, 2379–2387 (1995).
75. Dorkenoo, K. D. & Pfromm, P. H. Experimental Evidence and Theoretical Analysis of Physical Aging in Thin and Thick Amorphous Glassy Polymer Films. *J. Polym. Sci. Part B Polym. Phys.* **37**, 2239–2251 (1999).

76. Dorkenoo, K. D. & Pfromm, P. H. Accelerated Physical Aging of Thin Poly [1-(trimethylsilyl)-1-propyne] Films. *Macromolecules* **33**, 3747–3751 (2000).
77. McCaig, M. S. & Paul, D. R. Effect of film thickness on the changes in gas permeability of a glassy polyarylate due to physical aging Part I. Experimental observations. *Polymer* **41**, 629–637 (2000).
78. Huang, Y. & Paul, D. R. Experimental methods for tracking physical aging of thin glassy polymer films by gas permeation. *J. Memb. Sci.* **244**, 167–178 (2004).
79. Huang, Y. & Paul, D. R. Effect of Temperature on Physical Aging of Thin Glassy Polymer Films. *Macromolecules* **38**, 10148–10154 (2005).
80. Huang, Y. & Paul, D. R. Physical Aging of Thin Glassy Polymer Films Monitored by Optical Properties. *Macromolecules* **39**, 1554–1559 (2006).
81. Huang, Y. & Paul, D. R. Effect of Molecular Weight and Temperature on Physical Aging of Thin Glassy Poly (2,6-dimethyl-1,4-phenylene oxide ) Films. *J. Polym. Sci. Part B Polym. Phys.* **45**, 1390–1398 (2007).
82. Struik, L. C. E. Physical Aging in Plastics and Other Glassy Materials. *Polym. Eng. Sci.* **17**, 165 – 173 (1977).
83. Curro, J. G., Lagasse, R. R. & Simha, R. Diffusion model for volume recovery in glasses. *Macromolecules* **15**, 1621–1626 (1982).
84. Huang, Y., Wang, X. & Paul, D. R. Physical aging of thin glassy polymer films: Free volume interpretation. *J. Memb. Sci.* **277**, 219–229 (2006).
85. McCaig, M. S., Paul, D. R. & Barlow, J. W. Effect of film thickness on the changes in gas permeability of a glassy polyarylate due to physical aging: Part II. Mathematical model. *Polymer* **41**, 639–648 (2000).
86. Alfrey, T., Goldfinger, G. & Mark, H. The apparent second-order transition point of polystyrene. *J. Appl. Phys.* **14**, 700–705 (1943).
87. De Gennes, P. G. Reptation of a Polymer Chain in the Presence of Fixed Obstacles. *J. Chem. Phys.* **55**, 572 (1971).
88. Doi, M. & Edwards, S. F. Dynamics of concentrated polymer systems. Part 1. - Brownian motion in the equilibrium state. *J. Chem. Soc. Faraday Trans. 2* **74**, 1789–1807 (1978).
89. O’Connell, P. A. & McKenna, G. B. Rheological measurements of the thermoviscoelastic response of ultrathin polymer films. *Science* **307**, 1760–1763 (2005).
90. O’Connell, P. A. & McKenna, G. B. Dramatic stiffening of ultrathin polymer films in the rubbery regime. *Eur. Phys. J. E* **20**, 143–150 (2006).

91. O'Connell, P. A., Wang, J., Ishola, T. A. & McKenna, G. B. Exceptional Property Changes in Ultrathin Films of Polycarbonate: Glass Temperature, Rubbery Stiffening, and Flow. *Macromolecules* **45**, 2453–2459 (2012).
92. Rowland, H. D., King, W. P., Pethica, J. B. & Cross, G. L. W. Molecular confinement accelerates deformation of entangled polymers during squeeze flow. *Science* **322**, 720–724 (2008).
93. Bodiguel, H. & Fretigny, C. Viscoelastic dewetting of a polymer film on a liquid substrate. *Eur. Phys. J. E* **19**, 185–193 (2006).
94. Bodiguel, H. & Fretigny, C. Viscoelastic Properties of Ultrathin Polystyrene Films. *Macromolecules* **40**, 7291–7298 (2007).
95. Wang, J. & McKenna, G. B. Viscoelastic and Glass Transition Properties of Ultrathin Polystyrene Films by Dewetting from Liquid Glycerol. *Macromolecules* **46**, 2485–2495 (2013).
96. Karim, T. B. & McKenna, G. B. Unusual Surface Mechanical Properties of Poly( $\alpha$ -methylstyrene): Surface Softening and Stiffening at Different Temperatures. *Macromolecules* **45**, 9697–9706 (2012).
97. Paeng, K. & Ediger, M. D. Molecular Motion in Free-Standing Thin Films of Poly(methyl methacrylate), Poly(4-tert-butylstyrene), Poly( $\alpha$ -methylstyrene), and Poly(2-vinylpyridine). *Macromolecules* **44**, 7034–7042 (2011).
98. Evans, C. M., Narayanan, S., Jiang, Z. & Torkelson, J. M. Modulus, Confinement, and Temperature Effects on Surface Capillary Wave Dynamics in Bilayer Polymer Films Near the Glass Transition. *Phys. Rev. Lett.* **109**, 038302 (2012).
99. Ngai, K. L., Prevosto, D. & Grassia, L. Viscoelasticity of nanobubble-inflated ultrathin polymer films: Justification by the coupling model. *J. Polym. Sci. Part B Polym. Phys.* **51**, 214–224 (2013).
100. Ellison, C. J., Mundra, M. K. & Torkelson, J. M. Impacts of Polystyrene Molecular Weight and Modification to the Repeat Unit Structure on the Glass Transition–Nanoconfinement Effect and the Cooperativity Length Scale. *Macromolecules* **38**, 1767–1778 (2005).
101. Wu, X., Liu, C., Zhu, Z., Ngai, K. L. & Wang, L.-M. Nature of the Sub-Rouse Modes in the Glass - Rubber Transition Zone of Amorphous Polymers. *Macromolecules* **44**, 3605–3610 (2011).
102. Pye, J. E. & Roth, C. B. Two Simultaneous Mechanisms Causing Glass Transition Temperature Reductions in High Molecular Weight Freestanding Polymer Films as Measured by Transmission Ellipsometry. *Phys. Rev. Lett.* **107**, 235701 (2011).

103. Pye, J. E. & Roth, C. B. Above, below, and in-between the two glass transitions of ultrathin free-standing polystyrene films: Thermal expansion coefficient and physical aging. *J. Polym. Sci. Part B Polym. Phys.* **53**, 64–75 (2015).
104. Prevosto, D., Capaccioli, S. & Ngai, K. L. Origins of the two simultaneous mechanisms causing glass transition temperature reductions in high molecular weight freestanding polymer films. *J. Chem. Phys.* **140**, 074903 (2014).
105. Roth, C. B. Mobility and stability of glasses. *J. Polym. Sci. Part B Polym. Phys.* **48**, 2558–2560 (2010).
106. Priestley, R. D. Physical aging of confined glasses. *Soft Matter* **5**, 919 (2009).
107. Roth, C. B. & Dutcher, J. R. Glass transition and chain mobility in thin polymer films. *J. Electroanal. Chem.* **584**, 13–22 (2005).
108. Koh, Y. P. & Simon, S. L. Enthalpy Recovery of Polystyrene: Does a Long-Term Aging Plateau Exist? *Macromolecules* **46**, 5815–5821 (2013).
109. Fukao, K. & Sakamoto, A. Aging phenomena in poly(methyl methacrylate) thin films: Memory and rejuvenation effects. *Phys. Rev. E* **71**, 041803 (2005).
110. Napolitano, S. & Wübbenhorst, M. Structural relaxation and dynamic fragility of freely standing polymer films. *Polymer* **51**, 5309–5312 (2010).
111. Tompkins, H. G. *A User's Guide to Ellipsometry*. (Dover Publications, Inc., 1993).
112. Ellison, C. J., Kim, S. D., Hall, D. B. & Torkelson, J. M. Confinement and processing effects on glass transition temperature and physical aging in ultrathin polymer films: novel fluorescence measurements. *Eur. Phys. J. E* **8**, 155–66 (2002).
113. Simon, S. L., Sobieski, J. W. & Plazek, D. J. Volume and enthalpy recovery of polystyrene. *Polymer* **42**, 2555–2567 (2001).
114. Richardson, H., Carelli, C., Keddie, J. L. & Sferrazza, M. Structural relaxation of spin-cast glassy polymer thin films as a possible factor in dewetting. *Eur. Phys. Journal. E* **12**, 437–441 (2003).
115. Richardson, H., López-García, Í., Sferrazza, M. & Keddie, J. L. Thickness dependence of structural relaxation in spin-cast, glassy polymer thin films. *Phys. Rev. E* **70**, 051805 (2004).
116. Reiter, G. & Napolitano, S. Possible origin of thickness-dependent deviations from bulk properties of thin polymer films. *J. Polym. Sci. Part B Polym. Phys.* **48**, 2544–2547 (2010).
117. Frank, C. W., Rao, V., Despotopoulou, M. M., Pease, R. F. W., Hinsberg, W. D., Miller, R. D. & Rabolt, J. F. Structure in Thin and Ultrathin Spin-Cast Polymer Films. *Science* **273**, 912–915 (1996).

118. Riggleman, R. A., Yoshimoto, K., Douglas, J. F. & de Pablo, J. J. Influence of Confinement on the Fragility of Antiplasticized and Pure Polymer Films. *Phys. Rev. Lett.* **97**, 045502 (2006).
119. Kim, S., Mundra, M. K., Roth, C. B. & Torkelson, J. M. Suppression of the T<sub>g</sub> - Nanoconfinement Effect in Thin Poly(vinyl acetate) Films by Sorbed Water. *Macromolecules* **43**, 5158–5161 (2010).
120. Ellison, C. J., Ruskowski, R., Fredin, N. & Torkelson, J. M. Dramatic Reduction of the Effect of Nanoconfinement on the Glass Transition of Polymer Films via Addition of Small-Molecule Diluent. *Phys. Rev. Lett.* **92**, 095702 (2004).
121. Kosbar, L. L., Kuan, S. W. J., Frank, C. W. & Pease, R. F. W. Photophysical Studies of Spin-Cast Polymer Films. *ACS Symp. Ser.* **381**, 95–111 (1989).
122. Mundra, M. K., Ellison, C. J., Behling, R. E. & Torkelson, J. M. Confinement, composition, and spin-coating effects on the glass transition and stress relaxation of thin films of polystyrene and styrene-containing random copolymers: Sensing by intrinsic fluorescence. *Polymer* **47**, 7747–7759 (2006).
123. Fakhraai, Z., Sharp, J. S. & Forrest, J. A. Effect of sample preparation on the glass-transition of thin polystyrene films. *J. Polym. Sci. Part B Polym. Phys.* **42**, 4503–4507 (2004).
124. Sharp, J. S. & Forrest, J. A. Free Surfaces Cause Reductions in the Glass Transition Temperature of Thin Polystyrene Films. *Phys. Rev. Lett.* **91**, 235701 (2003).
125. Prucker, O., Christian, S., Bock, H., Ruhe, J., Frank, C. W. & Knoll, W. On the glass transition in ultrathin polymer films of different molecular architecture. *Macromol. Chem. Phys.* **199**, 1435–1444 (1998).
126. Reiter, G., Hamieh, M., Damman, P., Sclavons, S., Gabriele, S., Vilmin, T. & Raphaël, E. Residual stresses in thin polymer films cause rupture and dominate early stages of dewetting. *Nat. Mater.* **4**, 754–758 (2005).
127. Raegen, A. N., Massa, M. V., Forrest, J. A. & Dalnoki-Veress, K. Effect of atmosphere on reductions in the glass transition of thin polystyrene films. *Eur. Phys. J. E* **27**, 375–377 (2008).
128. Incropera, F. P., Dewitt, D. P., Bergman, T. L. & Lavine, A. S. *Fundamentals of Heat and Mass Transfer*. (John Wiley & Sons, 2007).
129. Shelby, M. D. & Wilkes, G. L. The effect of molecular orientation on the physical ageing of amorphous polymers—dilatometric and mechanical creep behaviour. *Polymer* **39**, 6767–6779 (1998).
130. Shelby, M. D., Hill, A. J., Burgar, M. I. & Wilkes, G. L. The effects of molecular orientation on the physical aging and mobility of polycarbonate solid state NMR and dynamic mechanical analysis. *J. Polym. Sci. Part B Polym. Phys.* **39**, 32–46 (2000).

131. Plazek, D. J. & O'Rourke, V. M. Viscoelastic Behavior of Low Molecular Weight Polystyrene. *J. Polym. Sci. Part A-2* **9**, 209–243 (1971).
132. O'Connell, P. A. & McKenna, G. B. The Stiffening of Ultrathin Polymer Films in the Rubbery Regime: The Relative Contributions of Membrane Stress and Surface Tension. *J. Polym. Sci. Part B Polym. Phys.* **47**, 2441–2448 (2009).
133. Tweedie, C. A., Constantinides, G., Lehman, K. E., Brill, D. J., Blackman, G. S. & Van Vliet, K. J. Enhanced Stiffness of Amorphous Polymer Surfaces under Confinement of Localized Contact Loads. *Adv. Mater.* **19**, 2540–2546 (2007).
134. Xu, W., Chahine, N. & Sulchek, T. Extreme hardening of PDMS thin films due to high compressive strain and confined thickness. *Langmuir* **27**, 8470–8477 (2011).
135. O'Connell, P. A., Hutcheson, S. A. & McKenna, G. B. Creep Behavior of Ultra-Thin Polymer Films. *J. Polym. Sci. Part B Polym. Phys.* **46**, 1952–1965 (2008).
136. Swallen, S. F., Kearns, K. L., Mapes, M. K., Kim, Y. S., McMahon, R. J., Ediger, M. D., Wu, T., Yu, L. & Satija, S. Organic Glasses with Exceptional Thermodynamic and Kinetic Stability. *Science* **315**, 353–357 (2007).
137. Singh, S., Ediger, M. D. & de Pablo, J. J. Ultrastable glasses from in silico vapour deposition. *Nat. Mater.* **12**, 139–144 (2013).
138. Guo, Y., Morozov, A., Schneider, D., Chung, J. W., Zhang, C., Waldmann, M., Yao, N., Fytas, G., Arnold, C. B. & Priestley, R. D. Ultrastable nanostructured polymer glasses. *Nat. Mater.* **11**, 337–343 (2012).
139. Yan, M. & Simon, S. L. Pressure relaxation of polystyrene and its comparison to the shear response. *J. Polym. Sci. Part B Polym. Phys.* **45**, 3375–3385 (2007).
140. Grassia, L., D'Amore, A. & Simon, S. L. On the viscoelastic Poisson's ratio in amorphous polymers. *J. Rheol.* **54**, 1009–1022 (2010).
141. Inoue, T., Hayashihara, H., Okamoto, H. & Osaki, K. Birefringence of amorphous polymers. II. Dynamic measurement and relaxation measurement. *J. Polym. Sci. Part B Polym. Phys.* **30**, 409–414 (1992).
142. Fujita, H. & Ninomiya, K. Dependence of Mechanical Relaxation Spectra of Linear Amorphous Polymers on the Distribution of Molecular Weights. *J. Polym. Sci.* **24**, 233–260 (1957).
143. Plazek, D. J. Magnetic Bearing Torsional Creep Apparatus. *J. Polym. Sci. Part A-2* **6**, 621–638 (1968).
144. Plazek, D. J. Temperature Dependence of the Viscoelastic Behavior of Polystyrene. *J. Phys. Chem.* **69**, 3480–3487 (1965).

145. Tschoegl, N. W., Knauss, W. G. & Emri, I. Poisson's Ratio in Linear Viscoelasticity – A Critical Review. *Mech. Time-Dependent Mater.* **6**, 3–51 (2002).
146. Meng, Y. & Simon, S. L. Pressure Relaxation of Polystyrene and Its Comparison to the Shear Response. *J. Polym. Sci. Part B* **45**, 3375–3385 (2007).
147. Zartman, G. D., Cheng, S., Li, X., Lin, F., Becker, M. L. & Wang, S.-Q. How Melt-Stretching Affects Mechanical Behavior of Polymer Glasses. *Macromolecules* **45**, 6719–6732 (2012).
148. Hiemenz, P. C. & Lodge, T. P. *Polymer Chemistry*. (Taylor & Francis Group, LLC, 2007).
149. Ward, I. M. & Sweeney, J. *Mechanical Properties of Solid Polymers*. (John Wiley & Sons, 2013).
150. Gilbert, D. G., Ashby, M. F. & Beaumont, P. W. R. Modulus-maps for amorphous polymers. *J. Mater. Sci.* **21**, 3194–3210 (1986).
151. Liu, S.-J. Modeling and simulation of thermally induced stress and warpage in injection molded thermoplastics. *Polym. Eng. Sci.* **36**, 807–818 (1996).
152. Higazy, A. A., Afifi, H., Khafagy, A. H., El-Shahawy, M. A. & Mansour, A. M. Ultrasonic studies on polystyrene/styrene butadiene rubber polymer blends filled with glass fiber and talc. *Ultrasonics* **44**, e1439–e1445 (2006).
153. Plaseied, A. & Fatemi, A. Tensile Creep and Deformation Modeling of Vinyl Ester Polymer and Its Nanocomposite. *J. Reinf. Plast. Compos.* **28**, 1775–1788 (2009).
154. Lai, C., Ayer, R., Hiltner, A. & Baer, E. Effect of confinement on the relaxation behavior of poly(ethylene oxide). *Polymer* **51**, 1820–1829 (2010).
155. Bauwens-Crowet, C. The compression yield behaviour of polymethyl methacrylate over a wide range of temperatures and strain-rates. *J. Mater. Sci.* **8**, 968–979 (1973).
156. Nanzai, Y. Molecular kinetics of yield deformation and ductile fracture in polymer glasses. *Prog. Polym. Sci.* **18**, 437–479 (1993).
157. Lach, R., Grellmann, W., Schröter, K. & Donth, E. Temperature dependence of dynamic yield stress in amorphous polymers as indicator for the dynamic glass transition at negative pressure. *Polymer* **40**, 1481–1485 (1999).
158. Cangialosi, D., Wübbenhorst, M., Groenewold, J., Mendes, E., Schut, H., Van Veen, A. & Picken, S. J. Physical aging of polycarbonate far below the glass transition temperature: Evidence for the diffusion mechanism. *Phys. Rev. B* **70**, 224213 (2004).
159. Zhao, J., Simon, S. L. & McKenna, G. B. Using 20-million-year-old amber to test the super-Arrhenius behaviour of glass-forming systems. *Nat. Commun.* **4**, 1783 (2013).

160. Haward, R. N. & Thackray, G. The Use of a Mathematical Model to Describe Isothermal Stress-Strain Curves in Glassy Thermoplastics. *Proc. R. Soc. A* **302**, 453–472 (1968).
161. Murphy, T. M., Freeman, B. D. & Paul, D. R. Physical aging of polystyrene films tracked by gas permeability. *Polymer* **54**, 873–880 (2013).
162. Peng, X. & McKenna, G. B. Comparison of the physical aging behavior of a colloidal glass after shear melting and concentration jumps. *Phys. Rev. E* **90**, 050301 (2014).